Chemical and Physical Mechanisms of Calcite Dissolution in Seawater

Thesis by

John David Naviaux

In Partial Fulfillment of the Requirements for

the degree of

Doctor of Philosophy in Environmental

Science and Engineering

CALIFORNIA INSTITUTE OF TECHNOLOGY

Pasadena, California

2020

Defended October 10, 2019

John David Naviaux
ORCID: 0000-0002-0681-3163

ACKNOWLEDGEMENTS

Academia constantly drives home the power of "we." Every project is made possible by the love and support of friends and family, and improved by the hard work and feedback of peers. Although it feels cheesy to say, this thesis is no exception. First and foremost, I would like to thank Jess for his advice and mentorship over the years. When I first came to Caltech, I barely knew anything about isotopes, let alone the oceans. It a testament to Jess's infectious intellectual curiosity that, from these humble beginnings, I dedicated the next half-decade to the study of marine chemistry (using isotopes!). This project has been the most interesting and fun one of my life, and I could not have predicted that it would involve challenges ranging from unexpected biology in the lab, to water gun fights in the middle of the Pacific Ocean. I will be forever grateful for this opportunity.

Of course, with Jess came the amazing network of people with which he has surrounded himself. I was fortunate enough to overlap with Adam, whose work served as the foundation of this project. My back-and-forths with Adam were invaluable, and he was always as excited as I was when I came running to his office with each new datapoint. My frequent trips to USC to pray to the Picarro gods were made all the better by my interactions with Will, Nick, and Sijia. Their ability to make complex equipment from random lab scraps helped to push the bounds of what I thought possible. And to the rest of the Adkins group, there is no one else with whom I'd rather drink copious amounts of coffee with every Wednesday morning.

I am also lucky to have such an amazing group of friends that have served to both support and distract when the need arose. Weekendfests with Trevor helped to ground me, as did my time free associating with the GPS crew, Alistair, Dan, Kyle, and Austin. I always looked forward to talking with Hans and Leah (of Fulbright/Funbright fame) and know that, while we may be on opposite sides of the globe, we will continue to be friends forever.

My mom and dad have also been an unwavering source of love and support. They instilled an early love of science in me, and were with me as I bounced around from psychology, to

economics, to particle physics, to finally finding my home in the environmental sciences. I could not ask for more loving and caring parents.

Of course, nothing has brought as much joy to my life as the family I have gained along the way. This is the second thesis that Tima, the best pup better than the rest pup (everybody knows it, EASY), has personally overseen, and her constant demands for walks and bellyrubs were essential to its success. Lucky for me, one of the best parts about Tima is the person that lives with her, Lauren. Lauren, even though we are both strong, independent people that are totally not co-dependent, I could not imagine my life without you. You are, without a doubt, the most impressive person I have ever met, and I am so grateful that I get to spend my life with you. You are my daily inspiration and best friend, and I am so excited to continue our adventure together. I love you to the moon and back.

ABSTRACT

Calcium carbonates are among the most abundant and reactive minerals on Earth, and their dissolution/preservation in the ocean helps to regulate changes in atmospheric pCO_2. The chemistry of the oceans has varied significantly over the past several billion years, and it is changing at an unprecedented rate today in response to anthropogenic burning of fossil fuels. The excess CO_2 from human activities is acidifying the oceans and decreasing the saturation state ($\Omega = \frac{[Ca^{2+}][CO_3^{2-}]}{K'_{sp}}$) of marine carbonates, increasing their propensity to dissolve. Despite its importance, the rate of carbonate dissolution in seawater is still described by a purely empirical expression, and the physical and chemical mechanisms setting the overall kinetics remain unknown. This stands in contrast to calcite dissolution in freshwater, where fully coupled surface-solution models have been identified. The lack of mechanistic understanding in seawater limits our ability to predict how carbonate dissolution kinetics, and therefore the buffering capacity of the ocean, are affected by changes in chemistry. This thesis advances our knowledge of the physical and chemical mechanisms responsible for carbonate dissolution by making new measurements in seawater both in the lab and *in-situ*.

I first probe the activation energy of the reaction in seawater by dissolving ^{13}C-labeled $CaCO_3$ across the full range of Ω at 5, 12, 21, and 37°C. I find that a surface-based framework is required to explain the strong non-linearity of the data near equilibrium. In this framework, dissolution proceeds by the retreat of pre-existing steps for $0.9<\Omega<1$, defect-assisted etch pit formation for $0.75<\Omega<0.9$, and homogenous etch pit formation for $0<\Omega<0.75$. I provide the first seawater estimates of kinetic coefficients (β), nucleation site densities (n_s), and step edge free energies (α) for each mechanism, as well as the activation energy for detachment from steps (ϵ_{step}) and the kinetic energy barrier to etch pit initiation (ϵ_{init}).

Next, I use a custom designed *in-situ* reactor to measure calcite dissolution rates across a transect of the North Pacific. I find that the same surface mechanisms and "critical" Ωs identified in lab also govern the dissolution of calcite in the open ocean. *In-situ* dissolution rates are ~4x slower than in the lab, but I use a combination of chemical spike experiments and measurements in archived seawater to show that this discrepancy can be explained by

the presence of dissolved organic carbon *in-situ*. I propose an empirical rate equation that describes all previous *in-situ* measurements of inorganic calcite dissolution rates.

Changes in the relation between dissolution rate and Ω can be explained by the activation of different surface processes, but the surface theory cannot account for much of the near-equilibrium dissolution behavior and temperature dependence. I therefore continue on in this thesis to combine the latest speciation models with dissolution measurements in artificial seawater of varying sulfate concentrations. I find that low sulfate solutions suppress dissolution rates by two orders of magnitude near equilibrium, while dissolution rates in the same solutions are enhanced far-from-equilibrium. Using these results, I fit a mechanistic model of dissolution that couples surface and solution processes. The model satisfies the principle of microscopic reversibility, provides an excellent estimate of calcite solubility product in seawater, and explains near equilibrium ($\Omega > 0.75$) dissolution rates in 0, 14, and 28 mM [SO_4^{2-}] seawater at 21°C. The model cannot explain dissolution rates for $\Omega < 0.75$ when etch pits begin opening homogenously across the surface, so I suggest areas of improvement for future models.

Previous work has demonstrated that calcite dissolution rates are enhanced in the presence of the enzyme carbonic anhydrase (CA). In the final chapter of this thesis, I evaluate the mechanism of CA rate enhancement by comparing the catalytic effects of freely dissolved CA, CA immobilized within hydrogels, and CA chemically bound onto porous silica beads. At the same time, I design and test a fluidized bed reactor and demonstrate its efficacy as a carbon capture device by attaching it directly to the Caltech cogeneration power plant smokestack. I find that dissolution rates within the reactor are only enhanced when CA is freely dissolved, strongly suggesting that the catalytic mechanism is direct proton transfer from the enzyme to the calcite surface.

PUBLISHED CONTENT AND CONTRIBUTIONS

Dong, S., Adkins, J.F., Rollins, N.E., Subhas, A. V., Naviaux, J.D., Celestian, A., Liu, X., Kemnitz, N., Byrne, R.H., Berelson, W.M., 2019. Aragonite Dissolution Kinetics and Calcite/Aragonite Ratios in Sinking and Suspended Particles in the North Pacific. Earth Planet. Sci. Lett. https://doi.org/10.1016/j.epsl.2019.03.016

J.D.N. assisted with the design and testing of the equipment used to collect data. J.D.N. also organized, cleaned, and assisted with the analysis of the data.

Dong, S., Subhas, A. V., Rollins, N.E., Naviaux, J.D., Adkins, J.F., Berelson, W.M., 2018. A kinetic pressure effect on calcite dissolution in seawater. Geochim. Cosmochim. Acta 238, 411–423. https://doi.org/10.1016/j.gca.2018.07.015

J.D.N. helped to interpret the observed kinetic pressure effect by applying a model of surface energetics to the data.

Naviaux, J.D., Subhas, A. V., Dong, S., Rollins, N.E., Liu, X., Byrne, R.H., Berelson, W.M., Adkins, J.F., 2019a. Calcite dissolution rates in seawater: Lab vs. in-situ measurements and inhibition by organic matter. Mar. Chem. 215, 103684. https://doi.org/10.1016/j.marchem.2019.103684

J.D.N conducted the experiments, analyzed all of the data, and wrote the manuscript for this publication.

Naviaux, J.D., Subhas, A. V., Rollins, N.E., Dong, S., Berelson, W.M., Adkins, J.F., 2019b. Temperature Dependence of Calcite Dissolution Kinetics in Seawater. Geochim. Cosmochim. Acta 246, 363–384. https://doi.org/10.1016/J.GCA.2018.11.037

J.D.N conducted the experiments, analyzed all of the data, and wrote the manuscript for this publication.

Subhas, A. V, Adkins, J.F., Rollins, N.E., Naviaux, J., Erez, J., Berelson, W.M., 2017. Catalysis and chemical mechanisms of calcite dissolution in seawater. Proc. Natl. Acad. Sci. 114, 8175–8180. https://doi.org/10.1073/pnas.1703604114

J.D.N. assisted with the model code and helped to understand the experimental data within a surface energetic framework.

TABLE OF CONTENTS

LIST OF ILLUSTRATIONS

LIST OF TABLES

C h a p t e r 1

TEMPERATURE DEPENDENCE OF CALCITE DISSOLUTION KINETICS IN SEAWATER

1.1 Introduction

Carbonate dissolution has been extensively studied for decades, but the functional form of its kinetic rate law is still debated. The simplest formulation, and the one used most frequently in the oceanographic community, is based upon an assumption that calcite dissolves via attack of water at the surface:

$$\mathrm{CaCO_3 + H_2O \rightleftharpoons Ca^{2+} + CO_3^{2-} + H_2O} \tag{1.1}$$

In transition state theory, the overall dissolution rate (R_{diss}) is the sum of simultaneous forward (R_f) and back (R_b) reactions, each with their own rate constants (k_f, k_b) such that:

$$\mathrm{R_{diss}} = R_f - R_b = k_f - k_b[Ca^{2+}]^m[CO_3^{2-}]^m \tag{1.2a}$$

Here, m is a constant describing the stoichiometry of the dissolution reaction. The forward rate depends solely on k_f in this formulation, as the activity of the solid is assumed to be 1. Substituting in the definitions of $\frac{k_f}{k_b} = [Ca^{2+}]^m[CO_3^{2-}]^m = K_{sp}^m$ and $\Omega = \frac{[Ca^{2+}][CO_3^{2-}]}{K_{sp}}$ yields (Lasaga, 1998):

$$\mathrm{R_{diss}} = k_b K_{sp}^m - k_b[Ca^{2+}]^m[CO_3^{2-}]^m = k(1 - \Omega^m) \tag{1.2b}$$

Here, k is the net dissolution rate constant per unit area and $1\text{-}\Omega^m$ is a measure of the thermodynamic driving force of the solution. Absent of mechanistic understanding, the oceanographic community has historically fit dissolution rates using the empirical equation (Berner and Morse, 1974; Keir, 1980; Morse, 1978):

$$R_{diss} = k(1 - \Omega)^n \quad (1.2c)$$

Here, n is referred to as the reaction order.

There is an ongoing conversation in the oceanographic community about whether calcite dissolution in natural waters obeys linear kinetics (m=n=1), or if a higher order n is required. The answer has important mechanistic implications, as values of n other than 1 imply that reactions beyond Eq. (1.1) set the dissolution rate of calcite in the ocean. Linear kinetics may be a reasonable approximation for synthetic calcite in non-seawater solutions (Svensson and Dreybrodt, 1992) far from equilibrium (Ω<0.8, Cubillas et al., 2005) or with packed calcite beds (Boudreau, 2013; Sulpis et al., 2017), but results with suspended particles both in the laboratory (Gehlen et al., 2005; Keir, 1983, 1980; Morse and Berner, 1972; Subhas et al., 2015; Teng, 2004; Walter and Morse, 1985; Xu et al., 2012) and *in-situ* (Berelson et al., 2007, 1994; Fukuhara et al., 2008; Honjo and Erez, 1978; Peterson, 1966) have consistently reported non-linear relationships between dissolution rate and undersaturation. The discrepancy cannot be attributed solely to uncertainties in calcite's apparent solubility product (Hales and Emerson, 1997), as recent work using updated K_{sp} values has confirmed non-linear kinetics for synthetic (Dong et al., 2018; Subhas et al., 2015, 2017) and biogenic (Subhas et al., 2018) calcites at the near equilibrium undersaturations (0.7<Ω<1) most relevant to the modern ocean water column (Olsen et al., 2016).

The oceanographic community has focused on the $(1-\Omega)^n$ rate law, but alternative theories dating back to Burton and Cabrera (1949; Burton et al., 1951; Cabrera and Levine, 1956) argue that the solution driving-force is a necessary, yet ultimately insufficient predictor of reaction kinetics. Crystals are made up of heterogeneous distributions of steps, kinks, defects, and dislocations, and their differing reactivities constrain both the rates and mechanisms of growth/dissolution. For example, it has been shown, using atomic force microscopy (AFM), that calcite dissolution in dilute solutions is limited to pre-existing steps until critical Ω thresholds are surpassed, at which point the overall rate increases dramatically as edge and screw dislocations open to become etch pits (Teng, 2004 and references therein). Models based upon the observed spread of 2D etch pits (Dove et al., 2008, 2005) or pulsing

stepwaves (Fischer and Lüttge, 2018; Lasaga and Lüttge, 2001; Lüttge, 2006) allow for these mechanistic transitions and have been used to describe dissolution for a variety of minerals.

The temperature dependence of calcite dissolution kinetics has been extensively studied as a means to understand the mineral's dissolution mechanism, but no study has investigated this dependence in seawater. Knowledge of the elementary reactions and surface complexes responsible for dissolution (Arakaki and Mucci, 1995; Busenberg and Plummer, 1986; Chou et al., 1989; Plummer et al., 1978; Pokrovsky and Schott, 2002), and their respective activation energies (Plummer et al., 1978; Oleg S. Pokrovsky et al., 2009) is limited to simple non-seawater solutions far from equilibrium. It is generally agreed that the dissolution rate of calcite is linearly dependent on the concentration of H^+ for pH<4-5 (Plummer et al., 1978; Plummer et al., 1979; Busenberg and Plummer, 1986; Chou et al., 1989; Arakaki and Mucci, 1995; Alkattan et al., 1998), and that the activation energy for the reaction is on the order of 8-10.5 kJ/mol (Morse and Arvidson, 2002; Sjöberg and Rickard, 1984a). The dissolution mechanism becomes more complicated at higher pH values as the system enters a regime of mixed transport and surface reaction control (Rickard and Sjöberg, 1983; Sjöberg and Rickard, 1984a). Rate constants collected in the mixed control regime combine several processes, so bulk dissolution studies frequently report "apparent," rather than true activation energies. Apparent activation energies vary with solution composition and experimental design, but tend to range from 14-25 kJ/mol when measured under atmospheric pCO_2 levels (Finneran and Morse, 2009; Gledhill and Morse, 2006; Gutjahr et al., 1996; Sjöberg, 1978; Sjöberg and Rickard, 1984a). Apparent activation energies can reach as high as 60 kJ/mol at elevated pCO_2 (Oleg S. Pokrovsky et al., 2009). AFM studies can calculate activation energies for specific surface processes (Liang et al., 1996; Liang and Baer, 1997; MacInnis and Brantley, 1992; Xu et al., 2010), but dissolution rates derived from scaling up AFM measurements frequently disagree with those from bulk dissolution measurements (Arvidson et al., 2003; Morse et al., 2007)

The goal of our work is to provide the first measurements of the temperature dependence of calcite dissolution kinetics in seawater. Using the ^{13}C tracer method of Subhas et al. (2015), we dissolve labeled calcite powders in a closed system at 5, 12, 21, and 37°C across the full range of saturation states. Our experiments are conducted in filtered seawater, and the sensitivity of the ^{13}C tracer method allows us to resolve the near equilibrium Ωs most relevant to the ocean. We gain further insight by applying the surface nucleation model of Dove et al. (2005) to our data to identify changes in dissolution mechanism and to parse the near-equilibrium effects of temperature on the physical and energetic properties of calcite.

1.2 Methods

Following the methods of Subhas et al. (2015), ^{13}C labeled calcium carbonate powder was purchased from Sigma Aldrich (SKU 492027, >99 atom%) and wet sieved (solution information below) into 70-100 and 20-53 μm size fractions. The total specific surface areas for each fraction were determined by Kr gas BET to be 900±40 cm^2/g for the 70-100um fraction, and 1520±60 cm^2/g for the 20-53 μm fraction. Dissolution rates in the literature are frequently normalized by average geometric surface area (270 and 625 cm^2/g for our samples), but we use BET normalized rates as they produce a tighter agreement between our size fractions. The use of geometric surface area does not affect our results, and for comparison, both geometric surface area rates ($g/cm^2/day$) and mass normalized rates (g/g/day) are reported alongside our BET surface area rates in the Appendix (Table A1).

It has been shown that a mineral's reaction history can alter densities of steps, edges, and/or etch pits, thereby changing the dissolution rate that is eventually measured (Arvidson et al., 2003; Arvidson and Luttge, 2010; Fischer et al., 2014, 2012). To ensure that our dissolution rates were not an artifact of our choice of sieving liquid, we compared dissolution rates of powders sieved in: (1) pure 18.2MΩ cm^{-1} water, (2) 18.2MΩ cm^{-1} water adjusted to pH 8.5 with ammonium hydroxide, and (3) Dickson standard seawater (https://www.nodc.noaa.gov/ocads/oceans/Dickson_CRM/batches.html) adjusted to Ω≈1 via HCl addition. A subset of powder that had been sieved in pH 8.5 ammonium hydroxide was also baked at 80°C under vacuum for 7 days. No differences in subsequent dissolution

rates were observed (Figure **1.1**), so data are reported for powders sieved in 18.2MΩ cm^{-1} water unless otherwise noted.

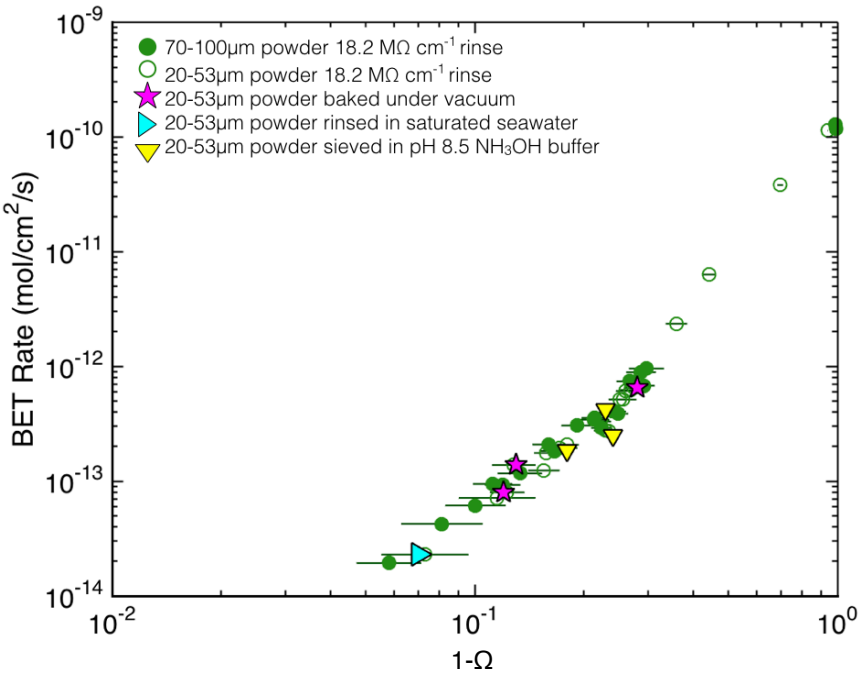

Figure 1.1: BET rates (mol/cm^2/s) versus 1-Ω at 21°C for 20-53µm (open circles) and 70-100µm (closed circles) size fractions, as well as 20-53µm grains with different treatments (see text for details). The majority of the data were collected using powders sieved in 18.2MΩ cm^{-1} water, but the different symbols show the consistency of our rates across a range of powder size fractions and rinse treatments.

Experimental bags were prepared by placing 1-5mg of $Ca^{13}CO_3$ powder inside a 1-L Supelco bag (part no. 30336-U) that had been modified (Subhas et al. 2015) to include an extra sampling port. The additional ports housed 0.2 µm filters to retain the carbonate powder during sampling. Bags were heat sealed and evacuated to remove all headspace. Experimental fill waters were made separately by first siphoning Dickson standard seawater (Batches 144-165) into another evacuated Supelco bag, and then titrating its total alkalinity (and therefore Ω) to the desired level via injection of 0.1M HCl. Silicate and phosphate differed between Dickson seawater batches, but only varied between 1-7 and 0.3-0.6

μmol/kg, respectively. Though phosphate adsorbs strongly to calcite surfaces (de Kanel and Morse, 1978; Millero et al., 2001) and is thought to be an inhibitor of dissolution (Berner and Morse, 1974; Sjöberg, 1978), variations in phosphate concentrations did not impact our results. The range of concentrations investigated in this study is much smaller than in studies that have documented significant inhibition (50 μmol/L, Walter and Burton, 1986), and preliminary experiments with seawater spiked to 20 μmol/L phosphate showed no inhibitory effect (not shown).

Each run began by siphoning 50g of fill water into the experimental bag to pre-rinse the calcite grains and remove any fine particles. The rinse water was subsequently taken out through the sampling port and discarded, after which the bags were filled with ~300g of seawater and placed in a recirculating water bath set to 5, 12, 21, or 37°C. The water bath maintained its temperature to ±0.1°C and was placed on a shaker table set to 85rpm. No change in dissolution rates were observed at higher shake speeds, but rates dropped significantly when stirring below 60rpm (Subhas et al., 2015). We used a rate of 85rpm to ensure that chemical transport was not limiting in our experiments. At no point was any headspace introduced into the system, so there was no change in the dissolved inorganic carbon (DIC) of the water due to exchange with the atmosphere. Fill water was always equilibrated to the desired temperature before being introduced into the experimental bags to ensure that initial measurements were not affected by a gradient in temperature between the bag and the water bath. Although not as important for experiments that ran for several days, this equilibration was crucial in achieving reproducible results in undersaturated waters below $\Omega<0.5$. Bags were sampled every 6-12 hours over the course of 2-5 days.

The samples were analyzed for DIC and ^{13}C using a Picarro cavity ringdown spectrometer. The $\delta^{13}C$ values were converted to moles dissolved per time, with typical traces shown in Figure **1**.**2**. The data become linear after an initial equilibration time <24 hours (Subhas et al., 2017), and points between 24 and 72 hours were fit with a linear regression using Microsoft Excel's Linest function, with the resulting slope taken as the dissolution rate. The relative error on the slope was used as the rate error and typically ranged from 1-5%. Total

alkalinity was measured by open-system Gran titration and compared against the alkalinity expected from dissolution, as derived from the ^{13}C mass balance. The agreement between these alkalinities was always within 1-4 µmol/kg. The final saturation state was calculated by CO2SYS using measured DIC, total alkalinity, and temperature. Standard errors in DIC (±2-4 µmol/kg) and alkalinity (±1-3 µmol/kg) were propagated using a Monte Carlo approach, giving a final error on Ω of 0.01 to 0.04 units. We used the carbonate system dissociation constants from the Dickson and Millero (1987) refit to Mehrbach et al.'s (1973) data, sulfate dissociation constants from Dickson et al. (1990), and a borate to salinity ratio from Uppström (1974).

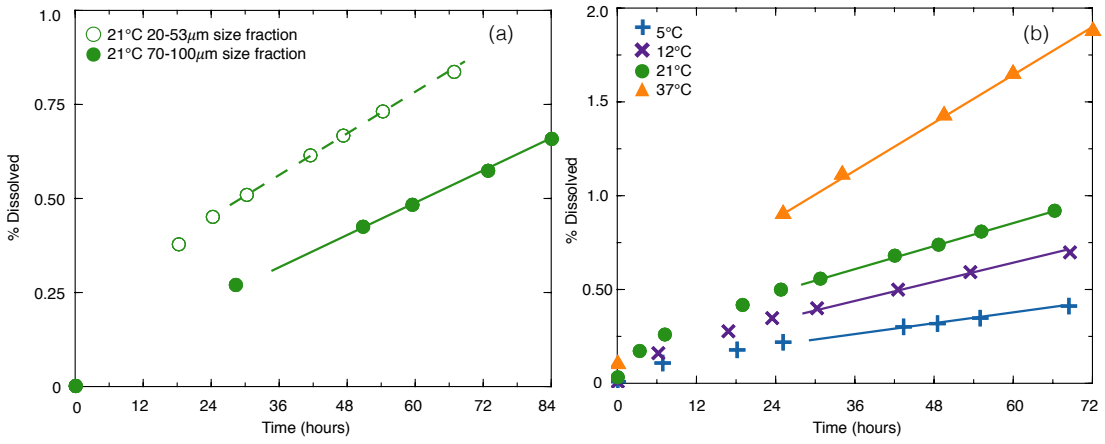

Figure 1.2: (a) Raw dissolution vs. time of two different size fractions of 13C-labeled calcite at 1-Ω = 0.83, normalized by the total fraction of powder dissolved. Curves become linear after 24 hours and the slope of the subsequent data points is taken as the rate (dashed/solid lines in the figure). The 20-53µm size fraction dissolves more quickly than the 70-100µm size fraction ($2.3 \cdot 10^{-3}$ vs. $1.4 \cdot 10^{-3}$ g/g/day), but both yield the same rate when corrected for BET surface area ($1.8 \cdot 10^{-13}$ mol/cm^2/s). (b) Raw dissolution vs. time at constant 1-Ω = 0.80. Increasing the temperature increases dissolution rate non-linearly.

Our dissolution rates were not affected by isotopic exchange. Experiments in supersaturated conditions (Ω=1.3) using the same methods saw no enrichment over the course of nine days beyond an initial increase in $\delta^{13}C$ of 1-3‰ (Subhas et al., 2015). Rate calculations rely on

the rate of change of the $\delta^{13}C$ signal versus time, so the time independent exchange signal we observed does not alter our measurements of the net dissolution rate.

1.3 Results

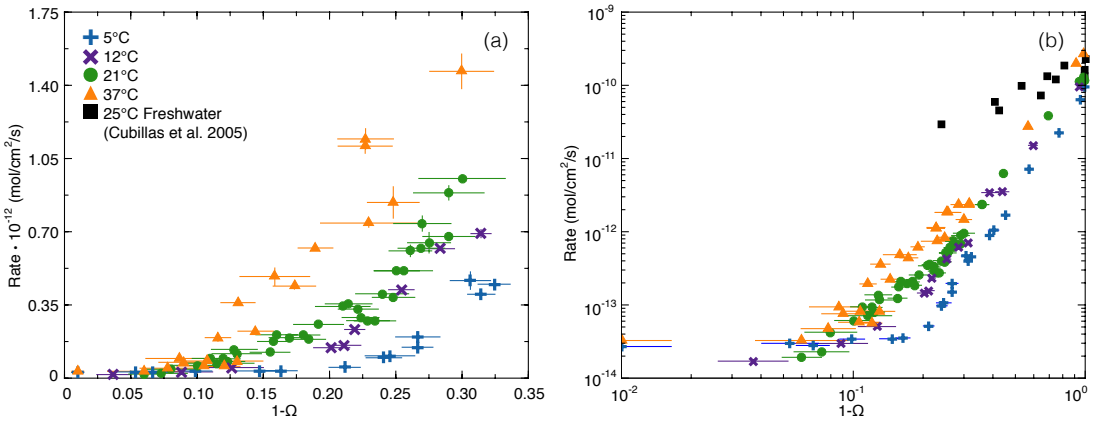

Figure 1.3: Comparison of calcite dissolution rates (mol/cm^2/s) plotted vs. 1-Ω (a) near equilibrium, and (b) in Log-Log 1-Ω space from 1>Ω>0. Dissolution in seawater behaves differently than in freshwater (black squares in b). The y-error bars reflect the error on the linear fit to the dissolution vs. time data from 24 to 72 hours and do not include the uncertainty in surface area.

Figure **1.3** shows our experimental results in the 1-Ω framework. Data in this plot cover a range of DIC and alkalinity of 1740-2050 and 807-2045 µmol/kg, respectively, corresponding with a calculated pH range of 5.7-7.65 on the total proton scale (Figure **1.4**). Our methodology allowed for rate data from each individual experiment to be collected under conditions of constant solution saturation and unchanging mineral surface area. Typical $\delta^{13}C$ dissolution signals were on the order of 5-40‰, where a 20‰ increase corresponds to a decrease in surface height of ~7-8 nm, an addition of just 1 µmol/kg of alkalinity, and the release of 10^{-7} mole of calcium (Subhas et al., 2015). This is the first work to measure the near-equilibrium temperature dependence of calcite dissolution with this level of sensitivity, and our analytical constraints mean that the observed rate changes may be more directly attributed to temperature dependent effects on the dissolution mechanism.

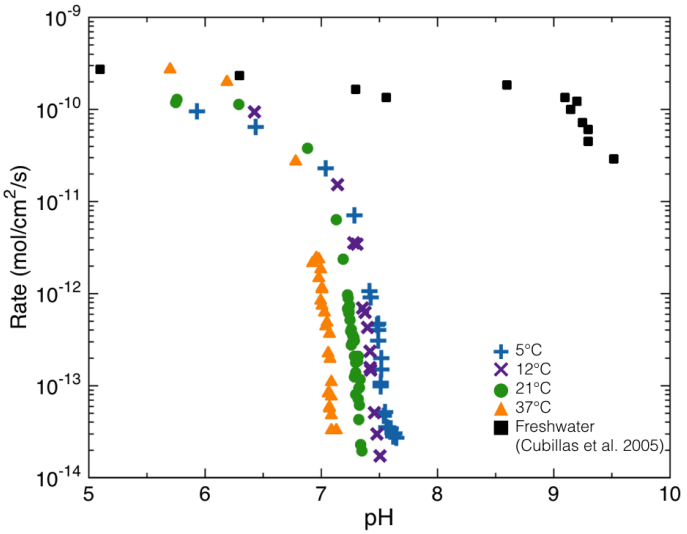

Figure 1.4: Calcite dissolution rates (mol/cm^2/s) versus in-situ pH_{total} calculated from CO2Sys using measured alkalinity and DIC pairs. Note that the dissolution rate at each temperature changes by nearly three orders of magnitude over 0.3 pH units. Seawater dissolution rates decrease sharply at a lower pH than in freshwater.

We can see from Figure **1.3**b that, although calcite dissolves at a similar rate in freshwater (Cubillas et al., 2005) and seawater at $\Omega \approx 0$, the mineral responds fundamentally differently in each media to changes in saturation state. The dissolution rate in freshwater increases almost linearly as Ω drops (left to right on the plot), but seawater dissolution is highly non-linear at all temperatures and consists of multiple different slopes in log-log space. Our data show that calcite dissolution rates increase by four orders of magnitude as Ω decreases from 1 to 0.

Calcite dissolution kinetics in seawater respond to temperature in a complex manner. Dissolution rates appear least sensitive to temperature for $\Omega>0.9$, but they transition to a regime where the temperature sensitivity increases greatly from $0.9>\Omega>0.75$. This strong dependence weakens after $\Omega \approx 0.75$, and the rate offsets between each temperature remain nearly constant as the solution approaches $\Omega = 0$.

1.4 Discussion

1.1.1 Analysis within the 1-Ω framework

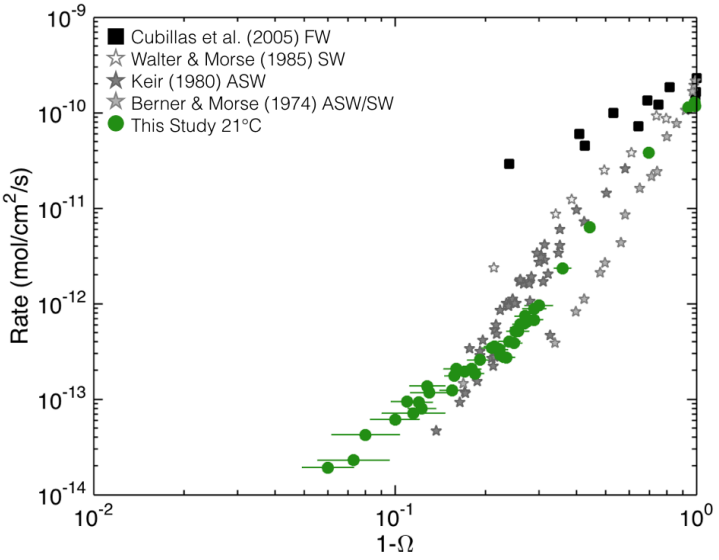

Figure 1.5: Comparison of calcite dissolution rates (mol/cm^2/s) in this study at 21°C versus previously published rates in freshwater (FW), seawater (SW), and artificial seawater (ASW) at 25°C. All data were taken directly from the published papers and were not adjusted to account for updated carbonate system equilibrium constants. Each study is normalized by BET surface area except for Cubillas et al. (2005), which is normalized by geometric surface area. The points from Berner & Morse (1974) combine the data for SW with 1.6 µmol/L phosphate and ASW with 0.5 µmol/L phosphate in Appendix Tables B and C, respectively. Data from Walter & Morse (1985) are for synthetic calcite and were taken from Fig. 1 of their paper and normalized using BET surface area from Table 3.

Previous work in freshwater has successfully fit calcite dissolution kinetics with near-linear rate laws (Cubillas et al., 2005; Svensson and Dreybrodt, 1992), but it is clear that this approach cannot describe our seawater data. Our results are highly non-linear against 1-Ω and exhibit a similar trend far from equilibrium as observed in previous bulk dissolution experiments in seawater (Figure **1.5**). Consistent with reports of a near equilibrium Ω_{crit} value in seawater (Dong et al., 2018; Subhas et al., 2015, 2017), we observe an abrupt change in the dissolution rate response to saturation at every temperature at $\Omega \approx 0.75$. Due to this change, no single rate law of the traditional $k(1-\Omega)^n$ form can describe the dissolution rate of calcite across the full range of saturation states. York regression fits to the reaction orders (n)

and net dissolution rate constants (*k*) are therefore calculated for data Ω<0.75 and Ω>0.75, with the results plotted in Figure **1.6** and listed in Table 1.1.

Table 1.1: York Fits to Log(R) = Log(k) + nLog(1-Ω)

T (°C)	Ω > 0.75		Ω < 0.75	
	$Log_{10}k$ ($mol/cm^2/s$)	n	$Log_{10}k$ ($mol/cm^2/s$)	n
5	-13.07 ± 0.18	0.34 ± 0.09	-10.01 ± 0.10	4.81 ± 0.07
12	-11.51 ± 0.15	1.92 ± 0.07	-9.95 ± 0.27	4.09 ± 0.15
21	-11.06 ± 0.10	2.15 ± 0.05	-9.83 ± 0.12	4.18 ± 0.07
37	-10.50 ± 0.13	2.47 ± 0.05	-9.56 ± 0.35	4.58 ± 0.22

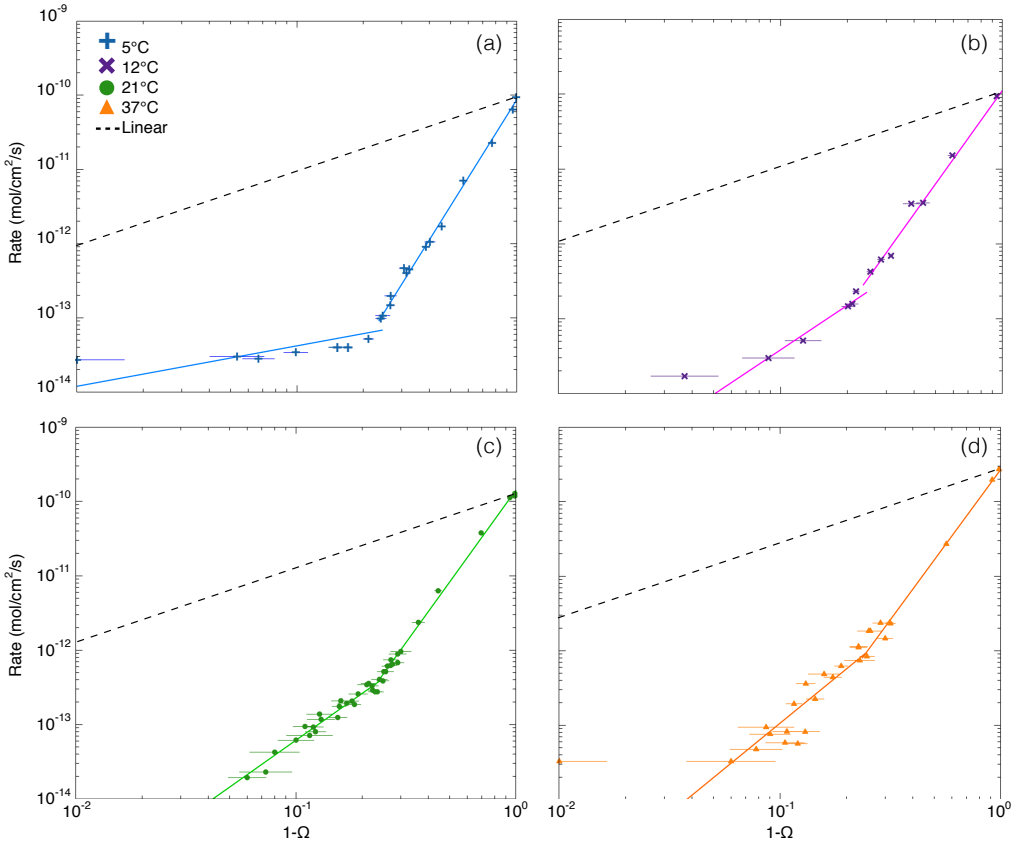

Figure 1.6: Rate vs. 1-Ω at 5 (a), 12 (b), 21 (c), and 37°C (d) overlaid with best-fit lines to the data before and after Ω = 0.75, not including data where Ω >0.9 (fitted values for *k* and *n* are listed in Table 1.1). The dashed lines in each panel show the expected behavior for a linear (*n*=1) dissolution rate law. The linear rate law is anchored by the rate constant at Ω=0, and greatly overestimates dissolution near equilibrium.

The deeply undersaturated (Ω<0.75) rate constants agree with values typically reported for calcite in solutions above pH >5 under atmospheric pCO_2 (order $1 \cdot 10^{-10}$ mol/cm^2/s, Plummer et al., 1978; Keir, 1980; Sjöberg and Rickard, 1985; Cubillas et al., 2005; Fischer and Lüttge, 2018; see also Table 5 in Subhas et al., 2015), and may be used to plot the expected behavior for a linear rate law by inserting them into Eq. (1.2c) with *n*=1 (the dashed lines in Figure **1.6**). In the region near equilibrium that is most relevant to the modern ocean (Ω>0.7), linear kinetics overestimate our measured rates by more than two orders of magnitude. The use of smaller *k*s would reduce the difference between the calculated and actual rates near

saturation, but the resulting fit would be entirely empirical and no longer grounded in the theory behind the 1-Ω rate law. Imposing linear kinetics also guarantees that dissolution rates across large ranges of Ω will be systematically over or underestimated. Our near equilibrium data require the reaction order to change with temperature from 0.34 to 2.47, and the rate constant to increase by over two orders of magnitude. These changes are interesting, but they represent simple curve fits and do not allow for meaningful mechanistic interpretations.

The temperature dependence of the far-from-equilibrium *k*s may still be used to gain insight into the dissolution mechanism. The apparent activation energy (E_a) of the dissolution reaction can be evaluated using the Arrhenius relation:

$$\ln(\mathrm{k}) = \ln(A) - \frac{E_a}{R} \cdot \frac{1}{T} \tag{1.3}$$

Here, A is a pre-exponential factor (mol/cm^2/s), E_a is the apparent activation energy (kJ/mol), and R is the molar gas constant (kJ/mol/K). Plotting the far-from-equilibrium rate constants in Arrhenius space (Figure **1.7**) yields a value for E_a/R of -3021±229, corresponding to an apparent activation energy of 25±2 kJ/mol. This E_a agrees with results of previous studies in which calcite was dissolved in low pCO_2 media (Table 1.2), suggesting a common mechanism controls far-from-equilibrium dissolution regardless of the solution.

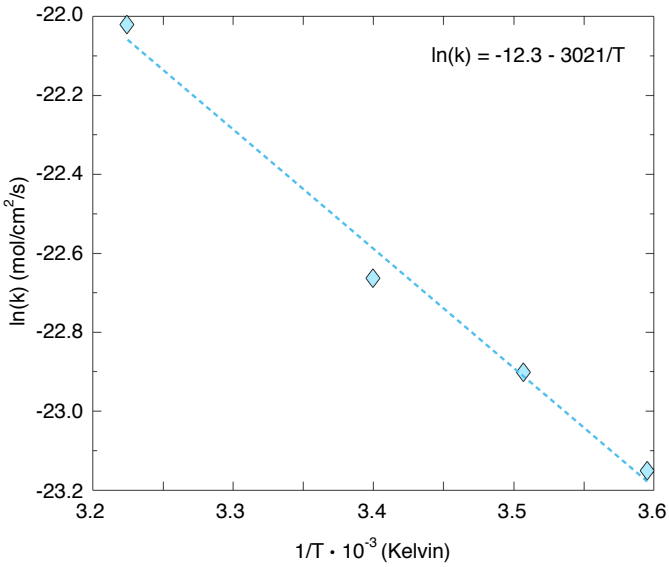

Figure 1.7: Arrhenius plot of rate constants derived from far-from-equilibrium (Ω<0.75) experiments. A linear fit to the data yields a slope of -3021±229 corresponding to an activation energy of 25±2 kJ/mol.

Table 1.2: E_a Compilation for bulk calcite dissolution far from equilibrium

Study	Solution	Temperature (°C)	pH	Ω	Activation Energy (kJ/mol)
Plummer et al., (1978)	DI Water	5-60	2-5	0*	8.4 (from Eq. 5)
Salem et al., (1994)	DI Water	15-35	9.2	0-0.04	8.7
Sjöberg (1978)	0.7M KCl	3-50	3.0	0*	10.5 (crystal)
Sjöberg & Rickard (1984)	0.7M KCl	1-62	2.7-3.7	0*	13±1 (Iceland Spar, from Fig. 7)
Finneran & Morse (2009)	0.07-5M Ionic Media	25-85	5.5-6.5	0.4-0.8	20±2
Gledhill & Morse (2006)	50-200g/L Brine	25-82.5	5-6.2	0.2-1	21±1
Gutjahr et al. (1996)	Ionic NaCl	20-70	7-9	0.4-1	24±3 (k_{diss} from Table 2)
Sjöberg (1978)	0.7M KCl	3-50	8.3	0*	25.7 (crystals) 35 (powder)
Sjöberg & Rickard (1984)	0.7M KCl	1-62	8.4	0*	31-36 (Carrara Marble, Eq. 9)
Pokrovsky et al. (2009)	0.1M NaCl, (pCO_2 2-50atm)	25-100	4.0	0*	48.2±4.6**
This study	Natural Seawater	5-37	5.5-6.5	0-0.75	25±2

*Ω is not reported, but the solution composition suggests Ω=0

**Pokrovsky et al. (2009) adjust this E_a to 14.7±3.5 when correcting for chemical transport

Calcite dissolution is linearly dependent on the concentration of H^+ for pH<4-5, is transport limited, (Alkattan et al., 1998; Arakaki and Mucci, 1995; Busenberg and Plummer, 1986; Chou et al., 1989; Plummer et al., 1979a, 1978), and exhibits a relatively small activation energy (8-10.5 kJ/mol Sjöberg and Rickard, 1984; Morse and Arvidson, 2002). Larger activation energies, like those compiled in Table 1.2 generally seen at higher pHs, indicate that dissolution is not purely transport limited and that additional reactions are occurring at the mineral surface (Morse and Arvidson, 2002; Sjöberg and Rickard, 1983). The exponential rate law (Eq. 1.2c) is a statement of mechanism if the dissolution rate is linear

(n=1) versus undersaturation, but our data clearly show that n varies with Ω. Given the magnitude of the E_a and the strong non-linearity of our data, a different mechanistic framework is required to understand the near-equilibrium dissolution rate of calcite in seawater.

1.4.1 Identification of changes in dissolution mechanism

As did Subhas et al. (2017), we applied a mechanistic framework originally developed for crystal growth (Chernov, 1984; Malkin et al., 1989) that was subsequently and successfully adapted by Dove et al. (2005, 2008) to describe dissolution. Dove et al.'s work is based upon AFM observations of silica minerals dissolving at different solution undersaturations. The authors saw three distinct dissolution mechanisms: retreat of pre-existing steps at edges and screw dislocations near equilibrium, opening of 2D "pancake" etch pits at defects farther from equilibrium and, finally, opening of 2D etch pits homogenously across the mineral surface at deeper undersaturations (see schematic in Figure **1.8**). The onset of each mechanism was accompanied by an increase in dissolution rate. The same general transitions observed by Dove et al. (2005) for quartz dissolution also occur in the non-seawater dissolution of calcite (Teng, 2004), although the size and shape of calcite etch pits can differ from 2D "pancakes" due to interactions with ions in solution (Ruiz-Agudo and Putnis, 2012; Klasa et al., 2013 and references therein). Other calcite dissolution models have been proposed (Fischer et al., 2012; Lasaga and Lüttge, 2001), but we continue with the Dove framework because it allows for the identification of dissolution mechanisms from bulk rate data and it can parse the effects of temperature on various kinetic and energetic parameters.

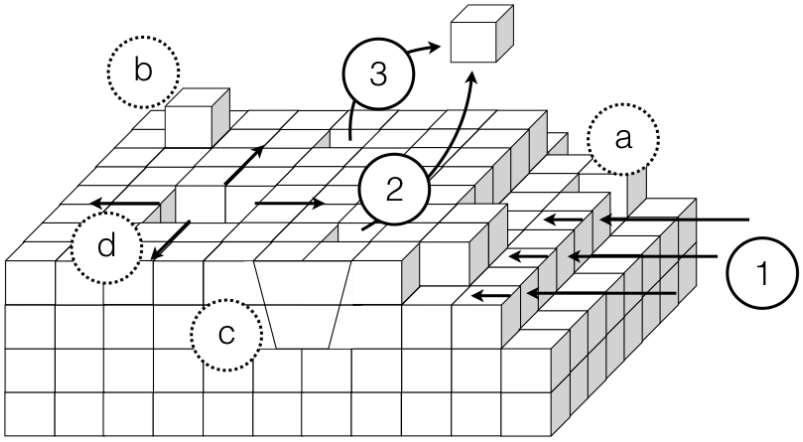

Figure 1.8: Simplified model of a dissolving calcite crystal where each cube represents a $CaCO_3$ unit cell. Numbered arrows demonstrate different dissolution mechanisms, while letters show surface features. At low driving forces, dissolution is limited to the retreat of pre-existing steps (1), kinks (a), and adatoms (b). Steps are frequently sourced from screw dislocations, but are only shown at edges here for simplicity. Defects such as edge-dislocations (c) impart strain on the crystal lattice, resulting in localized areas of excess surface energy. As the solution becomes more undersaturated, these areas become available for defect-assisted 2D dissolution (2). At even greater undersaturations, 2D dissolution occurs homogenously across the calcite surface (3) without the need for pre-existing defects. Both (2) and (3) produce 2D etch pits (d) that will propagate radially until they reach the edge of the mineral or encounter another etch pit and are eliminated

The exponential 1-Ω framework only considers the solution saturation state, but the Dove framework allows for changes in dissolution mechanism and incorporates information about a crystal's physical and energetic properties. This information is encapsulated in two equations describing the three different dissolution mechanisms: one equation for the spread of 2D etch pits, and one for the retreat of pre-existing steps. Recent observations have demonstrated that etch pits spread via pulsing stepwaves in deeply undersaturated solutions, and that the speed of the wave varies with the distance from its source (Fischer and Lüttge, 2018; Lasaga and Lüttge, 2001). The Dove rate equations make the simplifying assumption that the step speed does not depend on the source, and therefore uses a single equation to describe both defect-assisted and homogenous dissolution. This assumption is likely valid for bulk dissolution, as step speeds converge on a constant value within a new nanometers

from the pit source (Fischer and Lüttge, 2018). Full derivations of the Dove equations may be found in the appendix. The overall rate of dissolution by either defect-assisted or homogenous 2D etch pit growth (R_{2D}) is given by:

$$\ln\left(\frac{R_{2D}}{(1-\Omega)^{\frac{2}{3}}|\sigma|^{\frac{1}{6}}}\right) = \ln\left(h\beta C_e(\omega^2 h n_s a)^{\frac{1}{3}}\right) - \frac{\pi\alpha^2\omega h}{3(k_b T)^2}\left|\frac{1}{\sigma}\right| \qquad (1.4a)$$

Here, the left hand term is now the normalized dissolution velocity (m/s), $|\sigma|=\ln(\Omega)$ is a measure of the solution driving force, h is the step height (m), β is the rate constant for surface retreat (step kinetic coefficient, m/s), ω is the molecular volume (m^3), n_s is the density of active nucleation sites (sites/m^2), a is the lattice spacing (m), α is the step edge free energy (mJ/m^2), k_b is Boltzmann's constant, T is the temperature (Kelvin), and C_e is the mineral solubility. The rate equations were derived for a single component crystal, so C_e has units of molecules/m^3. Calcite is a two component crystal, but we relate calcite K_{sp} (mol^2/kg^2) in seawater to C_e by assuming constant $[Ca^{2+}]$=0.01M, such that $K_{sp}/[Ca^{2+}]=C_e$ after converting from mol/kg to molecules/m^3.

Although it appears complex, Eq. (1.4a) describes a straight line with a slope set by a single term (the step edge free energy, α), and an intercept set collectively by the kinetic coefficient (β) and the number of active nucleation sites (n_s). All other terms are either fundamental mineral properties assumed to be constant (h, ω, a), or are determined by the experimental conditions (C_e, T, Ω, σ).

Dissolution by the retreat of pre-existing steps and screw dislocations (R_{step}) is given by a different equation:

$$\ln\left(\frac{R_{step}}{(1-\Omega)^{\frac{2}{3}}|\sigma|^{\frac{1}{6}}}\right) = \ln\left(\frac{\omega\beta C_e mh}{P}\right) + \ln\left((1-\Omega)^{\frac{1}{3}}\left|\frac{1}{\sigma}\right|^{\frac{1}{6}}\right) - \ln\left(1+8\left(\frac{\omega\alpha}{Pk_bT}\right)\left|\frac{1}{\sigma}\right|\right) \quad (1.4b)$$

Here, the added terms are the number of elementary steps (m, order 1) and the perimeter of the screw dislocation core sourcing the steps (P, proportional to $2\pi mh$).

An advantage of this model is that bulk rate data exhibit distinct slopes when plotted as normalized rate versus $\left|\frac{1}{\sigma}\right|$ (Figure **1.9**), depending on the dominant dissolution mechanism. Even though both homogenous and defect-assisted dissolution are fit by Eq. (1.4a), we can distinguish between them based upon the distance from equilibrium. By definition, homogenous dissolution has a greater number of nucleation sites than defect-assisted dissolution. Data collected during homogenous dissolution are therefore expected to have a greater y-intercept than for defect-assisted dissolution. Additionally, we would expect the defect-assisted mechanism to have a shallower slope versus $\left|\frac{1}{\sigma}\right|$, as defects impose strain on the calcite surface and locally decrease the free energy of step formation per unit step height (α). The step-retreat mechanism is described by equation (1.4b), and curves upwards versus $\left|\frac{1}{\sigma}\right|$. Under this set of equations, it is important to note that the *absolute* rate always decreases as the solution approaches equilibrium (Figure **1.6**), and it is only the *normalized* rate that increases. The apparent increase near equilibrium is driven by the third term in Eq. (1.4b), where we take the natural log of (1-$\left|\frac{1}{\sigma}\right|$) (α is negative), and $\left|\frac{1}{\sigma}\right|$ becomes very large, and ultimately undefined, as Ω approaches 1.

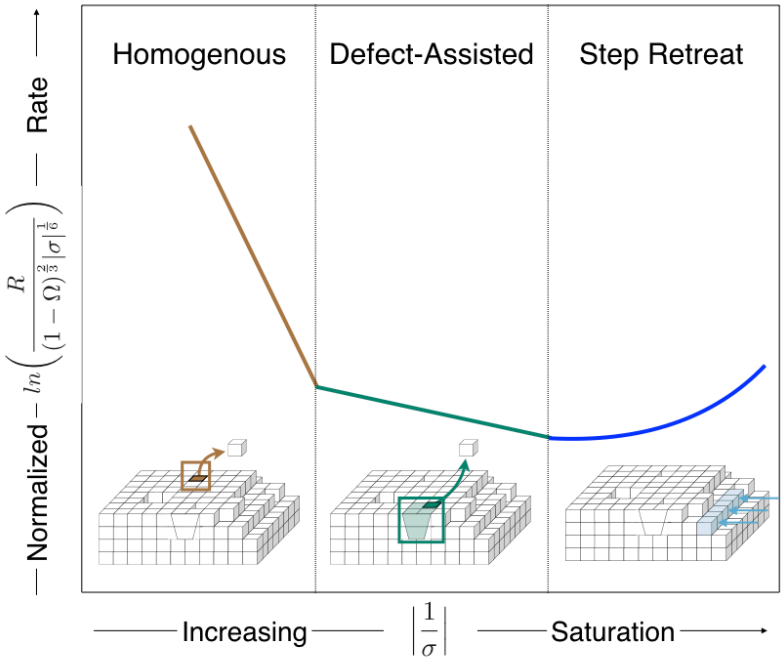

Figure 1.9: Expected data trends as the calcite surface transitions between dissolution mechanisms. Far from equilibrium (left panel), 2D etch pits open homogenously across the surface and the data are described by Eq. (1.4a). At intermediate driving forces, 2D dissolution may only proceed at defects (middle panel). Very near equilibrium, the solution driving force is only strong enough to support dissolution at pre-existing steps or screw dislocations (right panel). Data resulting from step retreat are described by Eq. (1.4b). Absolute rates of dissolution are slowest for step retreat, but the normalized rate curves upwards versus $\left|\frac{\mathbf{1}}{\boldsymbol{\sigma}}\right|$ as the solution approaches equilibrium.

Our results are plotted across the full range of saturations in Figure **1.10**, and they demonstrate each of the three expected trends in the surface framework. The non-linear nature of the x-axis emphasizes data collected at Ω>0.95, so the axis is truncated from $0<\left|\frac{1}{\sigma}\right|<25$ (0<Ω<0.96) in Fig. 8a-d to help view the data and fits more clearly. All temperatures exhibit a steep linear slope where $\left|\frac{1}{\sigma}\right|<3.5$ (Ω<0.75). Closer to equilibrium, dissolution at 12, 21, and 37°C shifts to a shallower linear slope, but this is not observed in

the 5°C data. Experimental dissolution rates measured at 12 and 37°C begin to 'curve upwards' after $\left|\frac{1}{\sigma}\right|$>10 (Ω>0.9, see also Figure **1.10**).

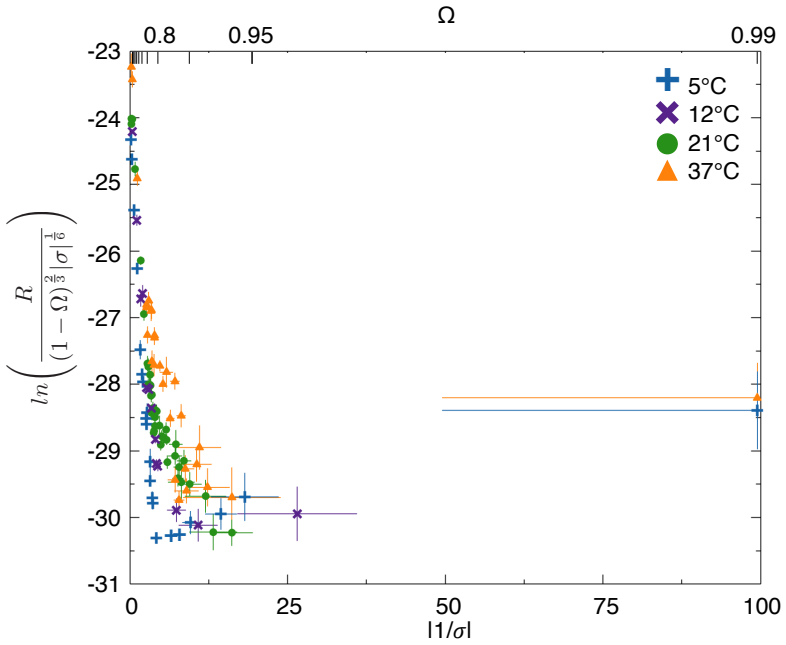

Figure 1.10: The same data as in Figure 1.3Figure 1.4, but recast as dissolution velocity (m/s) vs. $\left|\frac{\mathbf{1}}{\boldsymbol{\sigma}}\right|$ over the full range of undersaturations (0<Ω<0.99). Saturation state increases from left to right. Rates at 5, 12, and 37°C "curve upwards" as Ω approaches equilibrium, indicating dissolution by retreat of pre-existing steps. Tick marks on the top axis show Ω in increments of 0.1, with an additional tick at 0.95 to emphasize the highly non-linear nature of $\left|\frac{\mathbf{1}}{\boldsymbol{\sigma}}\right|$ axis.

We interpret each of the slope changes as mechanistic transitions that occur as the solution approaches equilibrium and falls below two critical energy barriers. Seawater calcite dissolution is dominated by homogenous etch pit formation from Ω=0 to Ω≈0.75, at which point etch pit formation may only occur at defects. These defect-assisted etch pits set the dissolution rate between Ω≈0.75 and Ω≈0.9, and dissolution at higher saturation states may only occur at pre-existing steps on edges and at screw dislocations. At 5°C, dissolution

appears to skip over the defect-assisted mechanism and instead transitions directly to the step-retreat mechanism.

The critical Ωs for mechanistic transitions that we have identified in seawater are much closer to equilibrium than they are in freshwater. Compared to observations by Teng (2004) in weak electrolyte solutions, the Ω_{crit} for the opening of defect-assisted etch pits in seawater is Ω=0.9 versus Ω=0.54, and the Ω_{crit} for homogenous etch pit formation (defined by Teng as Ω_{max}) is Ω=0.75 versus Ω=0.007. The rate of seawater calcite dissolution will be set by the density of pre-existing steps for Ω>0.9, and by the defect-density for $\Omega_{crit}>\Omega>\Omega_{max}$ (0.9>Ω>0.75). At colder temperatures relevant to the deep ocean, dissolution will be set by the density of pre-existing steps for 1>Ω>0.75. Once homogenous 2D dissolution is activated at $\Omega<\Omega_{max}$ (Ω<0.75), the overall rate will be limited by the maximum pit spreading rate.

The shift of calcite-seawater mechanistic transitions towards equilibrium is significant because it means that any model based upon a single rate equation, regardless of its reaction order, will not accurately capture dissolution responses to changes in saturation state. Our results suggest that typical ocean water column Ωs (>0.7) and temperatures (≤5°C) currently limit calcite to dissolution at pre-existing steps, but the oceans are acidifying due to fossil fuel burning and lowering both calcite and aragonite saturation states (Byrne et al., 2010; Doney et al., 2009; Feely et al., 2012, 2004). These perturbations in Ω may activate new surface mechanisms and elicit highly non-linear dissolution responses, both due to absolute changes in Ω and as regions where Ω<1 occur in warmer waters. As a rough comparison, we can calculate the magnitude of the offset between oceanographic models that assume linear (n=1) kinetics for Eq. (1.2c) (Dunne et al., 2012; Hales and Emerson, 1997; Ilyina and Zeebe, 2012) and our 5°C data. Arbitrarily beginning with a total alkalinity of 2230 μmol/kg at surface pressure, calcite is saturated (Ω=1) at a pH of ~7.6 at 5°C. Decreasing the pH by 0.1 units lowers Ω from 1.0 to ~0.8, maintaining step retreat as the rate-determining mechanism at 5°C and minimally affecting calcite dissolution rates. Further decreasing pH by 0.1 units drops Ω from ~0.8 to ~0.65, activating homogenous dissolution of the calcite surface. This second pH drop would increase calcite dissolution rates by a factor of ~25, whereas linear

kinetics would predict only a factor of ~2. The discrepancy between the different rate laws will only widen as the oceans continue to acidify.

Models based upon the non-linear n=4.5 reaction order from Keir (1980) (Archer, 1996, 1991; Archer et al., 2009; Berelson et al., 1994; Jahnke et al., 1994; Jansen et al., 2002) are similarly inadequate to describe dissolution. The high reaction order employed in these models is only applicable for $0<\Omega<0.75$ (Table 2) and does not capture the change in dissolution response when transitioning mechanisms near equilibrium. We find that the dissolution rate at 5°C is relatively constant versus Ω for $1>\Omega>0.75$, so a reaction order of n=4.5 will correctly predict far-from-equilibrium dissolution while systematically underestimating rates near equilibrium. A more appropriate approach would be to employ two different rate equations at 5°C, one for step retreat $\Omega>0.75$, and one for homogenous dissolution $\Omega<0.75$. This recommendation maintains the simplicity of the empirical rate equation while accounting for changes in dissolution mechanism.

1.4.2 Using temperature dependence to extract physical and energetic parameters of calcite dissolution in seawater

The inherent variability in step and defect densities between minerals complicate rate comparisons between studies (Arvidson et al., 2003; Fischer et al., 2014), but we can still advance our knowledge of calcite dissolution kinetics by analyzing the temperature dependence of our results within the surface framework. All of our calcite powders were sourced from the same batch and may be presumed to have the same initial step and defect densities. Tight control of solution saturation means that dissolution rate changes within each mechanistic regime may be directly related to the temperature dependence of fundamental physical and energetic properties in the calcite-seawater system. We step through each mechanism and calculate step edge free energies (α), kinetic coefficients (β), and active nucleation site densities (n_s). We also use the temperature dependencies of β and n_s to estimate the activation energy for detachment from retreating steps (ϵ_{step}) and the kinetic energy barrier for removing an ion to initiate an etch pit (ϵ_{init}).

The fitted slopes and intercepts (Figure **1.11**) are resolved for both homogenous and defect-assisted etch pit formation (Table 1.3); the cutoff of each fit is set to $\left|\frac{1}{\sigma}\right|$=3.5 (Ω=0.75) to remain consistent with our analysis in the 1-Ω framework. Our results are not sensitive to the precise cutoff choice. As noted in Section 1.4.1, dissolution at 5°C appears to skip over the defect-assisted mechanism, so only $\left|\frac{1}{\sigma}\right|$<3.5 for the 5°C data is included in our analysis of etch pit dissolution. The 5°C data have the highest density of measurements near equilibrium, so it will be used later to evaluate the energetics of the step retreat mechanism.

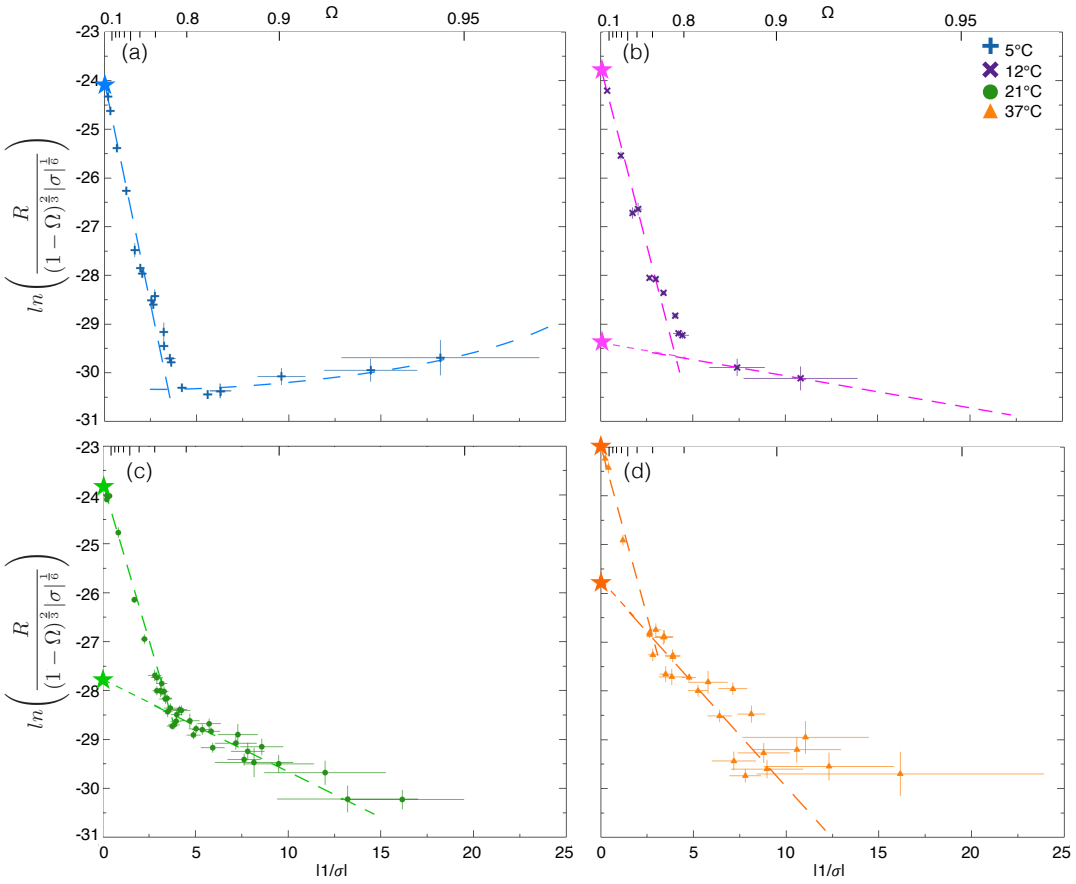

Figure 1.11: Dissolution velocities (m/s) at 5 (a), 12 (b), 21 (c), and 37°C (d) from $0<\left|\frac{\mathbf{1}}{\boldsymbol{\sigma}}\right|<25$ ($0<\Omega<0.96$). Saturation increases from left to right. All temperatures are fit to Eq. (1.4a) from $0<\left|\frac{\mathbf{1}}{\boldsymbol{\sigma}}\right|<3.5$. 12, 21, 37°C are fit to Eq. (1.4a) between $3.5<\left|\frac{\mathbf{1}}{\boldsymbol{\sigma}}\right|<25$ while 5°C is fit to Eq. (1.4b). The intercepts (stars on Y-axis) and slopes of the fits to Eq. (1.4a) are presented in Table 1.3.

Table 1.3: Fits to Eq. (1.4a) for 2D Dissolution

T (°C)	Homogenous Dissolution $0.01<\|1/\sigma\|<3.5$		Defect-Assisted Dissolution $3.5<\|1/\sigma\|<25$	
	Intercept $\ln\left(h\beta C_e(\omega^2 h n_s a)^{\frac{1}{3}}\right)$	Slope $\frac{\pi\alpha^2\omega h}{3(k_bT)^2}$	Intercept $\ln\left(h\beta C_e(\omega^2 h n_s a)^{\frac{1}{3}}\right)$	Slope $\frac{\pi\alpha^2\omega h}{3(k_bT)^2}$
5	-24.02 ± 0.02	-1.83 ± 0.04	N/A	N/A
12	-23.71 ± 0.04	-1.47 ± 0.03	-29.40 ± 0.90	-0.07 ± 0.11
21	-23.75 ± 0.01	-1.29 ± 0.03	-27.79 ± 0.25	-0.19 ± 0.04
37	-23.00 ± 0.11	-1.39 ± 0.06	-25.74 ± 0.26	-0.42 ± 0.05

By analyzing the fits to Eq. (1.4a) and making some simplifying assumptions, we can extract the physical parameters β, n_s, and α, and clarify their roles in setting the overall dissolution rate as a function of temperature. The intercepts and slopes are plotted in Figure **1.12** for homogenous ($0<\left|\frac{1}{\sigma}\right|<3.5$) and defect-assisted ($3.5<\left|\frac{1}{\sigma}\right|<10$) dissolution. The data are linear versus $1/T^2$ and are fit according to:

$$\text{Intercept}_{2D} = \ln\left(h\beta C_e(\omega^2 h n_s a)^{\frac{1}{3}}\right) = I_o + I_1 \cdot \frac{1}{T^2} \tag{1.5a}$$

$$\text{Slope}_{2D} = -\frac{\pi\alpha^2\omega h}{3(k_bT)^2} = S_o + S_1 \cdot \frac{1}{T^2} \tag{1.5b}$$

such that the overall rate is given by:

$$\text{Rate}_{2D} = \text{Intercept}_{2D} + \text{Slope}_{2D} \cdot \left|\frac{1}{\sigma}\right| = \left(I_o + I_1 \cdot \frac{1}{T^2}\right) + \left(S_o + S_1 \cdot \frac{1}{T^2}\right) \cdot \left|\frac{1}{\sigma}\right| \tag{1.5c}$$

I_1 and S_1 describe the temperature sensitivities of the intercept (proportional to β and n_s) and slope (proportional to α) terms of Eq. (1.4a). The values of I_o, I_1, S_o, and S_1 are listed in Table 1.4.

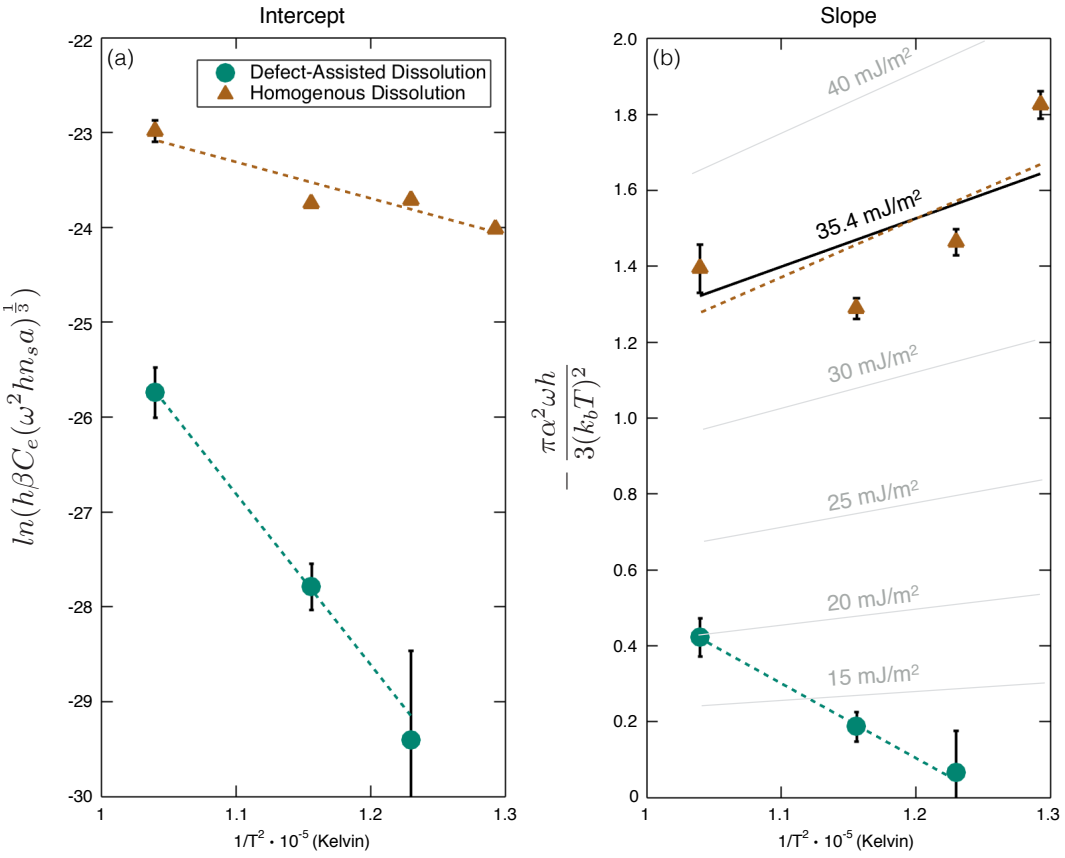

Figure 1.12: Temperature dependence of kinetic and energetic parameters of calcite dissolution in seawater. (a) Change in the intercept (proportional to β and n_s) and (b) slope (proportional to α) of the fit to Eq. (1.4a) for homogenous ($0<\left|\frac{\mathbf{1}}{\boldsymbol{\sigma}}\right|<3.5$, triangles) and defect-assisted ($3.5<\left|\frac{\mathbf{1}}{\boldsymbol{\sigma}}\right|<25$, circles) dissolution. Lines for constant α are plotted in (b) for comparison with the data. Fits to the data are presented in Table 1.4.

Table 1.4: Coefficients for the Observed Temperature Effect on the Intercepts and Slopes of Equation (1.4a) for 2D Dissolution

	I_0	$I_1 \cdot 10^5$	S_0	$S_1 \cdot 10^5$
Homogenous $0.01<\|1/\sigma\|<3.5$	-19.1 ± 1.18	-3.8 ± 1.0	0.33 ± 1.2	-1.5 ± 1.0
Defect-Assisted $3.5<\|1/\sigma\|<25$	-5.82 ± 1.29	-19.1 ± 1.1	-2.38 ± 0.12	1.9 ± 0.1

1.4.2.1 Dissolution by Homogenous Etch Pit Formation

Homogenous dissolution exhibits a relatively weak temperature dependence in its β and n_s terms (Figure **1.12**a). We can isolate the effect of β on the intercept term by making the simplifying assumptions that β is independent of Ω and that n_s is saturated at its maximum value when calcite is undergoing homogenous 2D dissolution. Direct observations of homogenous 2D calcite dissolution in non-seawater solutions place the maximum n_s between 10^{12} (Teng, 2004) and 10^{13} sites/m^2 (Ruiz-Agudo et al., 2009). Assuming an average n_s of $5 \cdot 10^{12}$ sites/m^2, we solve for β using the fitted intercepts (Table 1.3), rearranging Eq. (1.5a), and substituting in the constants given in Table 1.5. The resulting βs are 0.40±0.02, 0.54±0.05, 0.53±0.01, and 1.17±0.26 cm/s at 5, 12, 21, and 37°C, respectively.

Table 1.5: Constants and calculated values for β, n_s and α

Variable	Units	Temperature (°C) 5	12	21	37	Source
m	-	1	1	1	1	-
h	m	$3 \cdot 10^{-10}$	$3 \cdot 10^{-10}$	$3 \cdot 10^{-10}$	$3 \cdot 10^{-10}$	1
a	m	$3 \cdot 10^{-10}$	$3 \cdot 10^{-10}$	$3 \cdot 10^{-10}$	$3 \cdot 10^{-10}$	1
w	m^3	$6.12 \cdot 10^{-29}$	$6.12 \cdot 10^{-29}$	$6.12 \cdot 10^{-29}$	$6.12 \cdot 10^{-29}$	2
P	m	$1.88 \cdot 10^{-9}$	$1.88 \cdot 10^{-9}$	$1.88 \cdot 10^{-9}$	$1.88 \cdot 10^{-9}$	3
K_{sp}	mol^2/kg^2	$4.309 \cdot 10^{-7}$	$4.318 \cdot 10^{-7}$	$4.296 \cdot 10^{-7}$	$4.151 \cdot 10^{-7}$	4
C_e	atoms/ m^3	$2.595 \cdot 10^{22}$	$2.600 \cdot 10^{22}$	$2.587 \cdot 10^{22}$	$2.500 \cdot 10^{22}$	5
Homogenous 2D Dissolution (Eq. 4a)						
$n_{s\_homogenous}$	sites/m^2	$5 \cdot 10^{12}$	$5 \cdot 10^{12}$	$5 \cdot 10^{12}$	$5 \cdot 10^{12}$	1, 6
β_{2D}	m/s	$4.0 \pm 0.02 \cdot 10^{-3}$	$5.4 \pm 0.05 \cdot 10^{-3}$	$5.3 \pm 0.01 \cdot 10^{-3}$	$11.7 \pm 0.26 \cdot 10^{-3}$	this study
$\alpha_{homogenous}$	mJ/m^2	-37.6±0.7	-34.5±0.8	-33.2±0.7	-36.5±1.6	this study
Defect-Assisted 2D Dissolution (Eq. 4a)						
n_{s_defect}	sites/m^2	-	$4.7 \pm 1.2 \cdot 10^{5}$	$2.5 \pm 0.1 \cdot 10^{7}$	$1.3 \pm 0.9 \cdot 10^{9}$	this study
α_{defect}	mJ/m^2	-	-6.8±5.9	-12.7±2.7	-20.1±2.3	this study
Step-Propagation (Eq. 4b)						
β_{step}	m/s	$3 \cdot 10^{-7}$	-	-	-	this study
α_{step}	mJ/m^2	-0.5	-	-	-	this study

[1]Teng (2004)
[2]From calcite density of 2.71g/cm^3
[3]Estimated assuming a burgers vector $b = mh$. $P = 2\pi b$, analogously to Dove et al. (2005)
[4]CO2SYS equilibrium K_{sp} in seawater at each temperature. Sal = 35 psu
[5]$K_{sp}/[Ca^{2+}]$, converted to molecules/m^3. $[Ca^{2+}]$=0.01M
[6]Ruiz-Agudo et al. (2009)

The βs we derive agree with those observed in AFM studies in non-seawater solutions. In the surface nucleation equations, the speed of a moving step, ν, is related to β and the solution saturation state via (Chernov, 1984; Malkin et al., 1989):

$$v = \omega \beta C_e (1 - \Omega) \tag{1.6}$$

By extrapolating to Ω=0 and substituting the values for w, C_e, and β at each temperature, we calculate upper limits for ν of 6.2, 7.8, 10.3, and 16.4 nm/s at 5, 12, 21, and 37°C, respectively. Although faster than typical calcite values of 0.5-4 nm/s (Arvidson et al., 2006;

De Giudici, 2002; Harstad and Stipp, 2007; Lea et al., 2001; Ruiz-Agudo et al., 2009), they are in the range for observations at the edges of coalescing etch pits of 7.9-14.3 nm/s (Vinson and Luttge, 2005). Etch pit coalescence is expected when the calcite surface is saturated with nucleation sites, so our high step speeds support our assumption that the mechanism in this Ω region is homogenous 2D etch pit formation. We note that these equivalences of β are based upon non-seawater measurements of n_s. If the saturated value of n_s is different in seawater, then our βs will change accordingly.

We can use the temperature dependence of our derived kinetic coefficients to estimate the activation energy of detachment from steps (ϵ_{step}) on the calcite surface. β is related to ϵ_{step} via an Arrhenius-style relation (Chernov, 1984; Malkin et al., 1989; Zhang and Nancollas, 1992; Xu et al., 2010, Eq. A.8 in appendix), and measuring the slope of ln(β) versus 1/T yields a value of -2700±700, corresponding with an ϵ_{step} of -22±6 kJ/mol (Figure 1.13a). This is the first estimate of ϵ_{step} for calcite dissolution in seawater. It agrees with the value of -25±6 kJ/mol derived from AFM measurements of β for obtuse step retreat (Xu et al., 2010), further lending confidence to the strength and sensitivity of our bulk solution measurement approach.

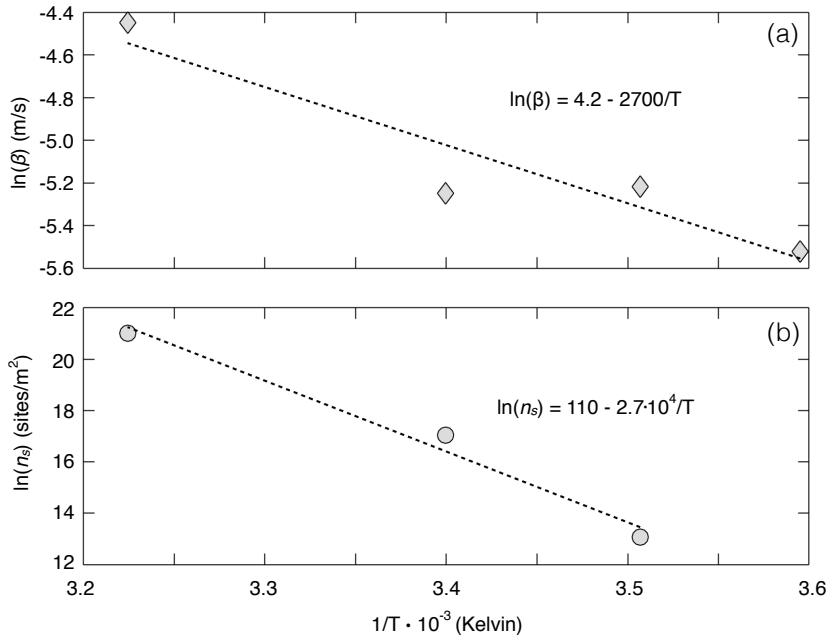

Figure 1.13: Arrhenius plots for the kinetic coefficient (a) and nucleation site density (b) derived from fits to Eq. (1.4a). (a) The slope of ln(β) versus 1/T is -2700±700, corresponding to an activation energy of detachment from kinks/steps of 22±6 kJ/mol. (b) The slope of ln(n_s) versus 1/T is 2.7±0.4•10^4, corresponding to a kinetic energy barrier to etch pit initiation of -230±30 kJ/mol.

Our calculated ϵ_{step} in seawater is not significantly different from that in freshwater, suggesting that changes in absolute ionic strength (IS) have little effect on step detachment energetics. Few studies have specifically measured the effect of IS on ϵ_{step}, so we cannot make a direct comparison with past research. The results are also unclear for the effects of IS on the bulk calcite dissolution/precipitation rate. Several studies have shown little to no effect of IS on calcite dissolution (Rickard and Sjöberg, 1983; Buhmann, 1987; Pokrovsky et al., 2005) and precipitation (Zhong and Mucci, 1989) rate, while others have found IS to catalyze precipitation (Zuddas and Mucci, 1998) and inhibit dissolution (Finneran and Morse, 2009; Gledhill and Morse, 2006). More remains to be done to understand how calcite dissolution mechanisms are affected by IS.

Our results further suggest that the sharp increase in rate at Ω≈0.75, that has been reported in previous seawater studies (Berner and Morse, 1974; Dong et al., 2018; Keir, 1980; Subhas et al., 2015, 2017), occurs when calcite transitions from defect-assisted to homogenous 2D dissolution after overcoming a critical step edge free energy. β and n_s provide kinetic information on the dissolving calcite surface (i.e., how fast etch pits spread and how many sites are actively dissolving), but they do not tell us anything about the energetic constraints for when homogenous dissolution is activated. For this, we can look at the slopes of the data below $\left|\frac{1}{\sigma}\right|$<3.5, as they are proportional to α. The calculated slopes (Table 1.3) are plotted in Figure **1.12**b versus $1/T^2$ and overlaid with lines of constant α. The overlaid lines trend downward with increasing temperature because the slope term in Eq. (1.4a) also contains $1/T^2$. The trend for homogenous dissolution (Figure **1.12** triangles) follows a line of constant α = -35.4 mJ/m^2. Though the scatter appears large, the squared dependence on α means that the step edge free energies are well constrained. Averaging the α values in Table 1.5 across temperatures yields 35.4±2.0 mJ/m^2. This α is lower, but of the same order of magnitude as the 60-68 mJ/m^2 range calculated for the spontaneous precipitation of calcite in non-seawater solutions (Koutsoukos and Kontoyannis, 1984; Pokrovsky, 1998a). Our observation suggests that homogenous dissolution is activated on the calcite surface once a critical surface energy barrier, $\alpha_{homogenous}$ = -35.4±2.0 mJ/m^2, is surpassed, regardless of temperature. It may also explain our earlier observation in Section 1.1.1 for why bulk dissolution studies historically recover similar rates far from equilibrium in seawater. Each study had surpassed $\alpha_{homogenous}$ and was measuring the dissolution rate of a single mechanism, homogenous 2D etch pit formation.

1.4.2.2 Dissolution by defect-assisted etch pit formation

Temperature has a much larger effect in the region 3.5<$\left|\frac{1}{\sigma}\right|$<10 associated with defect-assisted dissolution. According to Figure **1.12**a, the fitted intercepts for defect-assisted dissolution decrease with temperature by nearly four natural log units, compared to just one for homogenous dissolution. To understand this dependence, we must again attempt to distinguish between the effects of β and n_s on the intercept term of Eq. (1.4a). We can no

longer assume a constant n_s, but our analysis of homogenous dissolution provides new constraints on the values and temperature dependencies of β. Both mechanisms initiate differently, but once started, they are assumed to proceed via the same opening and spreading of 2D pits. We therefore assume that the same βs that we calculated for homogenous dissolution also apply for defect-assisted dissolution. We refer to this shared term as β_{2D} and list its values in Table 1.5. Given this assumption, we solve for n_s by again rearranging the intercept term and substituting in the constants and β_{2D} from Table 1.5. We calculate active nucleation site densities of $4.7\pm1.2\cdot10^5$, $1.3\pm0.1\cdot10^7$, and $1.8\pm0.9\cdot10^9$ sites/m^2 at 12, 21, and 37°C, respectively. Increasing temperature increases the number of pit nucleation sites.

The temperature dependence of n_s is related to the kinetic energy barrier for removing an ion from the surface to initiate an etch pit, ϵ_{init}. (Eq. A.9 in appendix, Dove et al., 2005). This energy barrier is distinct from the step edge free energy, as ϵ_{init} is related to initiating an etch pit, whereas α is related to stabilizing an etch pit. Newly initiated pits will quickly be eliminated unless a critical free energy barrier, that is in turn dependent on α, T, and Ω per Eq. (A.6), is surpassed. Taking the natural log of n_s versus 1/T gives a value of $-2.7\pm0.4\cdot10^4$, corresponding with an ϵ_{init} of -230±30 kJ/mol (Figure 1.13b). This is the first time that ϵ_{init} has been estimated for calcite in seawater.

It is evident that the slope term for defect-assisted dissolution is strongly temperature dependent in a way that is not explained by the theory and runs counter to what was observed for homogenous dissolution. Whereas homogenous dissolution follows the prediction for a single, critical $\alpha_{homogenous}$, the energy barrier for defect-assisted dissolution, α_{defect}, changes by nearly a factor of three (S_1 terms in Table 1.4) and has the opposite temperature dependence. This suggests that opposing kinetic and energetic effects set the overall rate of defect-assisted dissolution. Temperature has a positive effect on calcite dissolution rate by increasing n_s and β, allowing for more active nucleation sites and faster pit spreading rates. Warmer temperatures also increase the local step edge free energy, though, making it more difficult to form a stable etch pit. The change in the temperature trend of α implies that there are additional factors beyond α, β, and n_s that influence near-equilibrium dissolution rates.

1.4.2.3 Dissolution by retreat of pre-existing steps

It is difficult to set experimental waters to Ωs very near equilibrium, but the limited number of points we have suggest that dissolution initiates via step retreat at all temperatures and continues from just under saturation until an Ω_{crit} near 0.9. Dissolution at 5°C skips the defect-assisted mechanism seen at warmer temperatures and maintains the curved slope indicative of step retreat (Eq. 1.4b) from saturation until Ω≈0.75 (Figure **1.10**). Substituting in the constants in Table 1.5 to Eq. (1.4b), the 5°C data from $3.5<\left|\frac{1}{\sigma}\right|<25$ fit a step edge free energy of -0.5 mJ/m^2 and a β_{step} of $3\cdot10^{-5}$ cm/s. The kinetic coefficient required to fit the data is four orders of magnitude smaller than that used for homogenous/defect-assisted dissolution, but similar discrepancies between mechanisms have been seen in other minerals (Dove et al., 2005).

Of the temperatures investigated in this study, the 5°C experiments are most relevant to the modern ocean. The 5°C results are also the first evidence that the onset of a dissolution mechanism may be temperature dependent in seawater. We are unable to say with certainty why the defect-assisted dissolution mechanism is not activated, but one hypothesis is that the kinetic energy barrier to etch pit initiation is too large for etch pits to form at defects at 5°C. Projecting back the fitted intercept for defect-assisted dissolution reported in Table 1.4, we calculate an active nucleation site density of only 5 sites/cm^2 at 5°C. Considering that our grain size is on the 10s to 100s of microns scale, this would essentially mean that there are zero etch pits forming at defects. In this case, only step retreat is possible until the solution driving force overcomes $\alpha_{homogenous}$ and initiates homogenous dissolution.

Calcite has been shown to undergo simultaneous dissolution and precipitation across the full range of Ωs (Arakaki and Mucci, 1995; Subhas et al., 2017), so it is also possible that a temperature dependent change in the balance of these gross fluxes could explain the behavior we observe at 5°C. Precipitation is known to be influenced by the temperature and Mg:Ca ratio of the solution (Mucci, 1986; Mucci and Morse, 1984, 1983), and temperature

dependent step changes in behavior have already been observed in the calcite system (Morse et al., 1997). Precipitation occurs preferentially at high-energy sites (Burton et al., 1951; Burton and Cabrera, 1949), so any change in its rate could suppress the formation of etch pits at defects. This effect would be amplified if there were few available defects. Since back-precipitation may be identified on our calcite grains by areas of elevated ^{12}C (Subhas et al., 2017), we will be able to quantify the role of back-precipitation in the future by dissolving calcite surfaces near equilibrium at low temperatures.

1.4.3 Role of Solution Chemistry

The surface theory has provided valuable insights into calcite dissolution mechanisms across a wide range of saturation states, but phenomena such as the reversal of the temperature dependence of α and the skipping of defect-assisted dissolution at 5°C indicate that the theory is not complete. The surface framework we have used contains only indirect information about the chemical speciation of the solution and the mineral surface itself, despite the known importance of these effects (Arakaki and Mucci, 1995; Pokrovsky et al., 2009; Sand et al., 2016 and references therein). The surface model encapsulates all the effects of speciation in its step edge free energy term. This is because α is dependent upon the local crystal bonding environment, and this bonding environment is affected by interactions with ions in solution (Chernov, 1984). The speciation of the calcite surface is well understood in dilute solutions (Oleg S. Pokrovsky et al., 2009; Pokrovsky, 1998b; Pokrovsky et al., 2005; Pokrovsky and Schott, 2002; Schott et al., 2009; Van Cappellen et al., 1993; Wolthers et al., 2008), and significant work has been done to relate these species to dissolution and precipitation kinetics (Arakaki and Mucci, 1995; Chou et al., 1989; Oleg S. Pokrovsky et al., 2009; Pokrovsky et al., 2005; Pokrovsky and Schott, 2002; Wolthers et al., 2012a). Surface speciation models have only recently begun to include interactions with individual major seawater ions such as SO_4^{2-} and Mg^{2+} (Song et al., 2017; Dobberschütz et al., 2018, and references therein), and these models have yet to be applied to the kinetics of seawater dissolution. Our measurements imply that a complete understanding of a dissolution rate law for calcite in seawater will require a surface energetic framework that incorporates the chemical complexation of the solution and mineral surface.

The role of solution chemistry on the dissolution rate of calcite in seawater has been supported by recent work by Subhas et al. (2017) using carbonic anhydrase (CA) to increase the re-equilibration rate of H_2CO_3 in seawater. With the addition of CA, the authors observed a ~250x increase in calcite dissolution rates above $\Omega>0.7$, compared to seawater at the same pH without CA. This saturation region is associated with defect-assisted dissolution, which is the mechanism we found to have the strongest temperature dependence. Given that the rate constant for the hydration of $CO_{2(aq)}$ to H_2CO_3 increases exponentially with temperature in dilute solutions (Wang et al., 2010), it is possible that the behavior we have observed for $\Omega>0.75$ may be partially explained by an elevation in the formation rate of H_2CO_3. Future work evaluating the temperature dependence of calcite dissolution in the presence of carbonic anhydrase will help to further parse the effects of solution chemistry and surface processes on the overall dissolution rate.

1.5 Conclusions

We dissolved ^{13}C-labeled calcite in seawater over a range of temperatures and found that the dissolution rate is highly non-linear across the full range of saturations. Although we recovered the same activation energy and dissolution rates at $\Omega = 0$ as those found in non-seawater solutions, the strong non-linearity of our data near equilibrium necessitated the use of a different mechanistic model beyond the traditional, empirical rate law, $R=k(1-\Omega)^n$. Using a surface-based framework developed by Dove et al. (2005), we found that our results were consistent with calcite dissolution being dominated by the retreat of pre-existing steps for $1>\Omega>0.9$, defect-assisted etch pit formation for $0.9>\Omega>0.75$, and homogenous etch pit formation for $\Omega<0.75$. Calcite surface energetics are dramatically altered by seawater, as the mechanistic transitions we identified occur significantly closer to equilibrium than they do in dilute solutions. The shift towards equilibrium suggests that ocean acidification may cause marine carbonates to enter faster dissolution regimes more readily than anticipated from previous studies. Our work also provides the first seawater estimates of kinetic coefficients (β), nucleation site densities (n_s), and step edge free energies for each mechanism (α), as well as the activation energy for detachment from steps (ϵ_{step}) and the kinetic energy barrier to etch pit initiation (ϵ_{init}). Several unexplained phenomena suggest that a complete theory will

require the combination of a chemical speciation model with knowledge of the rate constants and energies we have measured for each of calcite's dissolution mechanisms.

Chapter 2

CALCITE DISSOLUTION RATES IN SEAWATER: LAB VS. IN-SITU MEASUREMENTS AND INHIBITION BY ORGANIC MATTER

2.1 Introduction

Ever since the first *in-situ* measurements of marine carbonate dissolution provided evidence for a non-linear rate response to undersaturation (Berger, 1967; Peterson, 1966), extensive work has been dedicated to untangling the relationship between dissolution rate and Ω. In the absence of a mechanistic understanding of the reactions in seawater, the oceanographic community has historically fit dissolution rates to an empirical equation of the form (Morse et al., 2007; Morse and Arvidson, 2002):

$$R_{diss} = k(1 - \Omega)^n \quad (1)$$

Here, k is the rate constant (mol cm^{-2} s^{-1}), Ω is a measure of the thermodynamic driving force, and n is the pseudo reaction order. Dissolution in low ionic strength aqueous solutions can be adequately described by Eq. (1) with n = 1 (Arakaki and Mucci, 1995; Cubillas et al., 2005; Svensson and Dreybrodt, 1992), as can the dissolution of packed calcite beds (Boudreau, 2013; Sulpis et al., 2017), but the dissolution of suspended calcite powder in seawater requires a non-linear reaction order ranging from 3-4.5 (Dong et al., 2018; Keir, 1980; Morse, 1978; Morse and Berner, 1972; Naviaux et al., 2019b; Subhas et al., 2015, 2017; Walter and Morse, 1985).

The non-linearity of Eq. (1) in seawater is consistent with the calcite surface transitioning through three dissolution mechanisms that become active at different critical saturations ("$\Omega_{critical}$s"): retreat of pre-existing steps for Ω = 1 to $\Omega_{critical} \approx 0.9$, the opening of etch pits at defects for Ω ≈ 0.9 to $\Omega_{critical} \approx 0.75$, and the opening of etch pits homogenously across the surface for Ω < 0.75 (Naviaux et al., 2019b). These surface processes have been previously identified in studies of calcite dissolution in low ionic strength aqueous solutions (Teng,

2004; Xu et al., 2012), but the $\Omega_{critical}$s for the activation of each mechanism occur significantly closer to equilibrium in seawater (Naviaux et al., 2019b). In this mechanistic framework, dissolution rates set by etch pit formation (R_{2D}), either at defects or homogenously across the surface, can be fit by (Dove et al., 2005):

$$\ln\left(\frac{R_{2D}}{(1-\Omega)^{\frac{2}{3}}|\sigma|^{\frac{1}{6}}}\right) = \ln\left(h\beta C_e(\omega^2 h n_s a)^{\frac{1}{3}}\right) - \frac{\pi\alpha^2\omega h}{3(k_b T)^2}\left|\frac{1}{\sigma}\right| \quad (2a)$$

Here, the left hand term is the normalized dissolution velocity (m s^{-1}), $|\sigma|=\ln(\Omega)$ is a measure of the solution driving force, h is the step height (m), β is the rate constant for surface retreat (step kinetic coefficient, m s^{-1}), ω is the molecular volume (m^3), n_s is the density of active nucleation sites (sites m^{-2}), a is the lattice spacing (m), α is the step edge free energy (J m^{-2}), k_b is Boltzmann's constant (J K^{-1}), T is the temperature (K), and C_e is the mineral solubility (atoms m^{-3}). Eq. (2a) describes a straight line with a slope set by a single term (the step edge free energy, α), and an intercept set collectively by the step kinetic coefficient (β) and the number of active nucleation sites (n_s). All other terms are either fundamental mineral properties assumed to be constant (h, ω, a), or are determined by the experimental conditions (C_e, T, Ω, σ).

Dissolution by the retreat of pre-existing steps and screw dislocations (R_{step}) dominates near equilibrium and is described by an equation that is non-linear with respect to $\left|\frac{1}{\sigma}\right|$:

$$\ln\left(\frac{R_{step}}{(1-\Omega)^{\frac{2}{3}}|\sigma|^{\frac{1}{6}}}\right) = \ln\left(\frac{\omega\beta C_e m h}{P}\right) + \ln\left((1-\Omega)^{\frac{1}{3}}\left|\frac{1}{\sigma}\right|^{\frac{1}{6}}\right) - \ln\left(1+8\left(\frac{\omega\alpha}{P k_b T}\right)\left|\frac{1}{\sigma}\right|\right) \quad (2b)$$

Here, the added terms are the number of elementary steps (m, order 1), and the perimeter of the screw dislocation core sourcing the steps (P, proportional to $2\pi mh$).

The work of Naviaux et al. (2019) more generally shows that n and k are variable functions of Ω and temperature, so attempts to describe marine calcite dissolution rates with a single fit to Eq. (1) will fail. The $\Omega_{critical}$s associated with each mechanistic transition are also temperature dependent, with the transition from step retreat to defect assisted etch pit formation being suppressed at 5°C. In other words, at the temperatures most relevant to undersaturated ocean waters, dissolution exhibits a weak dependence on Ω when $0.75 < \Omega < 1$ ($n < 1$) until the activation of homogenous etch pit formation at $\Omega_{critical} \approx 0.75$. Since each mechanistic regime responds differently to changing environmental variables, dissolution rates from one saturation range cannot be extrapolated to others.

Several fundamental issues remain to be solved in the field of seawater calcite dissolution kinetics, one of which is that dissolution rates measured in the lab (Keir, 1980; Morse, 1978; Morse and Berner, 1972) are consistently faster than those measured *in-situ* (Berelson et al., 1994; Berger, 1967; Fukuhara et al., 2008; Honjo and Erez, 1978; Milliman, 1975; Peterson, 1966). Some of the discrepancy results from comparisons between minerals of different size fractions (Morse, 1978) and dissolution histories (Arvidson et al., 2003; Arvidson and Luttge, 2010; Fischer et al., 2014, 2012), but the remaining offset is generally explained by the presence of inhibitors in natural seawater.

The most commonly invoked inhibitors are soluble reactive phosphate (SRP) and dissolved organic carbon (DOC). Both SRP and DOC adsorb to the calcite surface (de Kanel and Morse, 1978; Millero et al., 2001; Suess, 1973; Zullig and Morse, 1988) and have been shown to affect rates of calcite dissolution (Alkattan et al., 2002; Barwise et al., 1990; Berner et al., 1978; Berner and Morse, 1974; Compton et al., 1989; Compton and Sanders, 1993; Oelkers et al., 2011; Sjöberg, 1978; Thomas et al., 1993) and precipitation (Berner et al., 1978; Burton and Walter, 1990; Dove and Hochella, 1993; Hoch et al., 2000; Inskeep and Bloom, 1986; Kitano and Hood, 1965; Lin et al., 2005; Mucci, 1986; Reddy, 1977; Reynolds, 1978; Zullig and Morse, 1988). The magnitude of the effects vary greatly between studies,

and some carried out in seawater reported little influence of SRP (Walter and Burton, 1986) and DOC (Morse, 1974; Sjöberg, 1978) on calcite dissolution kinetics. These contrasting results warrant further study, and the finding that the calcite dissolution mechanism varies with Ω and temperature (Naviaux et al., 2019b) means that inhibitor effects should be explicitly investigated near equilibrium.

Another fundamental issue facing the oceanographic community is that individual measurements of the seawater CO_2 system parameters yield internally inconsistent values (Carter et al., 2018, 2013; Fong and Dickson, 2019; McElligott et al., 1998; Patsavas et al., 2015; Raimondi et al., 2019; Williams et al., 2017). Advances in measurement techniques (Dickson, 1993; Liu et al., 2011) have revealed that pH on the total hydrogen ion scale (pH_T) measured spectrophotometrically is offset from pH_T calculated from combinations of alkalinity (Alk), total dissolved inorganic carbon (DIC), and/or pCO_2. The discrepancy between measured and calculated pHs is itself pH dependent (Carter et al., 2018), so the offset cannot be explained simply by the inherent uncertainty in the seawater CO_2 system parameters (Orr et al., 2018). Whereas internal consistency between measurements and calculations can, in some cases, be attained by accounting for excess "organic alkalinity" (Cai et al., 1998; Patsavas et al., 2015; Yang et al., 2015) and adjusting the carbonic acid dissociation constants and the total boron-salinity ratio (Fong and Dickson, 2019), these adjustments are currently empirical. Hence, a more accurate description of seawater CO_2 chemistry is critical for our understanding of marine carbonate dissolution. For example, the position of the $\Omega = 1$ saturation horizon, defined as the depth in the water column below which calcium carbonate minerals should begin to dissolve, shifts by up to ~10% depending on the choice of parameters used to calculate Ω (Patsavas et al., 2015). Without a way to evaluate the "true" *in-situ* Ω, the position of the "true" saturation horizon remains unknown (Carter et al., 2018)

In this study, we attempt to reconcile and explain the long-standing discrepancies between calcite dissolution rates measured in the lab and in the field, as well as investigate how to best evaluate the "true" saturation horizon. We use a newly developed *in-situ* reactor to

quantify dissolution rates of ^{13}C-labeled inorganic calcite across an August 2017 transect of the North Pacific Ocean on the Calcite Dissolution Kinetics-IV (CDisK-IV) field campaign, and we compare these *in-situ* rates to rates measured under laboratory conditions. We use a surface energetic framework (Dove et al., 2005; Naviaux et al., 2019b) to demonstrate that the same dissolution mechanisms occur in the field as they do in the lab. We investigate the effects of several different natural inhibitors, and we demonstrate that our results may be used to describe previous *in-situ* inorganic calcite dissolution measurements.

2.2 Methods

2.2.1 Description of Materials

This manuscript focuses on the dissolution of ^{13}C calcite, but the *in-situ* reactor was tested prior to deployment using both ^{13}C calcite and ^{13}C-labeled coccolithophores (Subhas et al., 2018). Isotopically pure ^{13}C calcite was purchased from Sigma Aldrich (SKU 492027, > 99 atom%) and wet-sieved with 18.2 MΩ cm^{-1} water into 70-100 and 20-53 μm size fractions, the specific surface areas of which were determined by Kr-gas BET to be 0.09 ± 0.004 m^2 g^{-1} and 0.152 ± 0.006 m^2 g^{-1}, respectively (Naviaux et al., 2019b; Subhas et al., 2015). Laboratory measurements of calcite dissolution (protocol in Section 2.2.2) were carried out using both size fractions, and the dissolution rates agreed within experimental reproducibility (10% for dissolution rates of 10^{-15} – 10^{-10} mol cm^{-2} s^{-1}) once normalized to their respective surface areas (Naviaux et al., 2019). A more detailed discussion of the rinsing and surface area normalization procedures may be found in Naviaux et al. (2019). *In-situ* ^{13}C calcite dissolution measurements were carried out using only the 20-53 μm size fraction.

Coccolithophores (*E. huxleyi*) were cultured in ^{13}C-labeled seawater and were determined to have a specific surface area of 10.4 m^2 g^{-1} using Kr-gas BET (Subhas et al., 2018). A detailed description of the culturing and harvesting procedures may be found in Subhas et al. (2018). Subhas et al. measured the dissolution rates of both bleached and unbleached coccoliths, but only the bleached samples were used in the preliminary tests of the *in-situ* dissolution reactor.

2.2.2 Laboratory Measurements of Dissolution

Pure ^{13}C calcite and ^{13}C-labeled coccolithophores were dissolved under conditions of near constant alkalinity, DIC, Ω, and mineral surface area according to previously published methods (Naviaux et al., 2019b; Subhas et al., 2018, 2015, 2017). Briefly, 1-5 mg of pre-weighed, labeled material was placed within gas-impermeable Supelco bags (Sigma Aldrich: part no. 30336-U) that had been modified to include a custom sampling port with built-in filter. The bags were subsequently heat-sealed, evacuated of headspace, and filled with ~300g of seawater (seawater sourcing discussed below) of known alkalinity and DIC. The alkalinity of the seawater, and therefore its saturation state, was adjusted via titration with 0.1M HCl prior to filling the experimental bags. After filling, bags were placed in a water bath at 5 or 21°C and mounted on a shaker table set to 85 rpm. This shake rate has been shown to avoid diffusion limitation of the dissolution rate (Dong et al., 2018; Naviaux et al., 2019b; Subhas et al., 2015). Samples were withdrawn every six to twelve hours and measured simultaneously for DIC (± 2-4 μmol kg^{-1}) and $\delta^{13}C$ of the DIC ($\delta^{13}C$-DIC, ± 0.02‰) on a modified Picarro cavity ringdown spectrometer (Subhas et al., 2015). Alkalinity (± 1-3 μmol kg^{-1}) was measured potentiometrically at the beginning and end of each experiment via open-system Gran titration end-point determination (Dickson, 2007). Typical experiments dissolved < 10^{-7} moles of calcite, so alkalinity, DIC, and mineral surface area remained constant within measurement uncertainty. The $\delta^{13}C$ measurements at each timepoint were converted to number of moles dissolved, and the overall dissolution rate was determined from a linear fit to data collected after 24 hours. The initial non-linear equilibration period is well understood and is a result of simultaneous gross dissolution and precipitation fluxes coming into steady state (Subhas et al., 2017).

Laboratory saturation states were calculated using alkalinity-DIC pairs as input parameters in CO2SYS v1.1 (van Heuven et al., 2011) with the carbonic acid system K_1' and K_2' dissociation constants from the Lueker et al. (2000) refit to Mehrbach et al.'s (1973) data, calcite K_{sp}' from Mucci (1983), K_{HSO4} from Dickson (1990a), and K_{boron} from Dickson (1990). The total boron-salinity ratio was taken from Lee et al., (2010). The standard errors in DIC and alkalinity were propagated using a Monte Carlo approach (Subhas et al., 2015),

yielding final errors on Ω of 0.01-0.04 units. One of the goals of our research was to evaluate the offset between Ω calculated from alkalinity and DIC ($\Omega_{(Alk,\ DIC)}$), and Ω calculated from alkalinity and pH ($\Omega_{(Alk,\ pH)}$). Since the offset is systematic rather than random, the Ω errors we report are a description of our measurement precision, and do not include the uncertainty in the carbonic acid system dissociation constants (Orr et al., 2018).

Dissolution experiments were conducted in either Dickson Seawater Reference Material (Dickson, 2010) or archived seawater collected from the North Pacific during the CDisK-IV field campaign in August 2017. Dickson seawater was acquired from the Scripps Institution of Oceanography of the University of California, San Diego, where it was sterilized via UV-treatment, 0.2 μm filtration, and poisoned with $HgCl_2$. The practical salinity of the batches used ranged from 33.2 to 33.6, and the SRP and dissolved nitrate concentrations were between 0.3-0.5 and 0.36-5.1 μmol kg^{-1}, respectively. North Pacific seawater was collected from a CTD (conductivity, temperature, depth) cast from a depth of 75 m at 35°16.346 N, 150°59.515 W (Station 3), where it was immediately transferred into a 10L carboy and poisoned with $HgCl_2$ to a concentration of 0.0015% by weight. The archived water had a practical salinity of 33.905, SRP concentration of 0.293 μmol kg^{-1}, dissolved nitrate concentration of 2.07 μmol kg^{-1}, and was not filtered. The water was transferred into gas impermeable bags upon arrival on shore in September 2017, and dissolution experiments were conducted the following month.

Inhibition experiments were conducted by adding different compounds to Dickson seawater and evaluating the resulting change in calcite dissolution rates. Due to the varied and contradictory reports of the effects of SRP and DOC, experiments were designed to establish an upper limit to the inhibitory response that could be expected in open ocean environments. DOC in the upper water column is composed of, among other things, a complex array of mono and dicarboxylic acids (Moran et al., 2016). Gallic (CAS: 149-91-7) and oxalic acid (CAS: 133-62-7) were initially selected as model compounds to represent marine DOC. The effect of D-(+)-glucose (CAS: 50-99-7) was later investigated after it was noted that respiration in our archived seawater increased the DIC without a corresponding increase in

alkalinity (Section 2.3.3). Concentrated stock solutions of gallic acid, oxalic acid, KH_2PO_4 (CAS: 7778-77-0), and D-(+)-glucose were each prepared in 18.2 MΩ cm^{-1} water that had been adjusted to an ionic strength of 0.5M using NaCl. To eliminate variability in inhibitor concentrations between replicate experiments, ~1 mL of stock solution was injected into a 3 L reservoir of Dickson seawater before being divided into smaller batches for use in dissolution experiments. Final concentrations were 100 µmol kg^{-1} (glucose) or 20 µmol kg^{-1} (all other compounds).

2.2.3 *In-situ* Reactor Design and Lab Verification

Sixteen 1.7L Niskin bottles (General Oceanics SKU 101001.7) were modified to include a recirculating pump system that would allow ^{13}C labeled coccoliths, aragonite (Dong et al., 2019), and calcite to dissolve without diffusion limitation (Figure **2.1**). Once closed at depth, water sealed within the reactor flows over the material and accumulates ^{13}C-DIC from dissolution. The difference between the $\delta^{13}C$-DIC in the reactor bottle and that of the surrounding water column is a direct measure of the amount of dissolution that occurred, and dividing by the deployment time provides a rate.

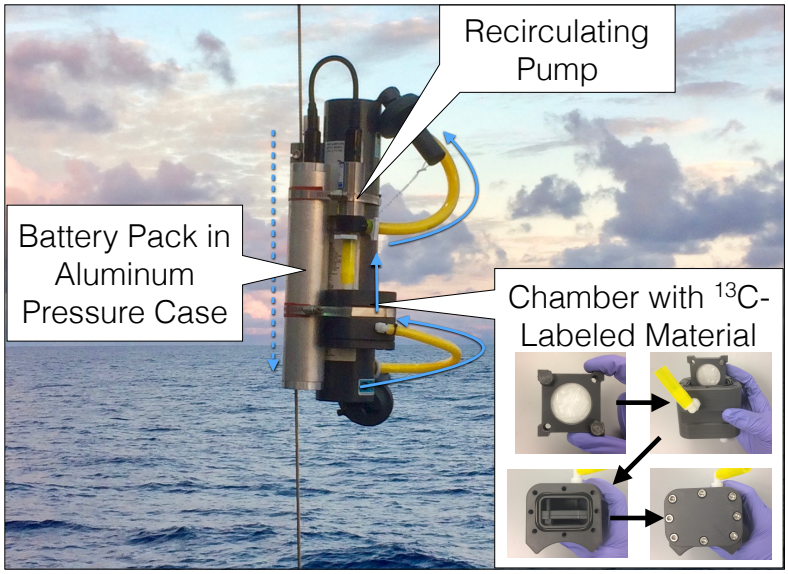

Figure 2.1: A standard 1.7L Niskin bottle was modified for dissolution experiments. A chamber containing ^{13}C-labeled material sealed within mesh packets was affixed to the

side, along with a recirculating pump and an aluminum pressure case to hold the batteries. The pump operates continuously and pushes water over the labeled material in the direction of the blue arrows.

To create the recirculating system, the bottom port of each Niskin was connected, using MasterFlex tubing (Tygon Fuel & Lubricant Tubing, 06401-82 and 06401-17), to a custom side chamber where labeled material could be easily accessed and exchanged between deployments. Additional tubing connected the top of the chamber to the inlet of a pump (Seabird SBE 5M mini pump, part 05M.2120), the outlet of which was routed to the top Niskin port by a final section of tubing. The pump drew water from the bottom of the Niskin to the top at a rate of 5 mL s^{-1} and was powered by four 1.5 V D-cell batteries held in an aluminum pressure case. A plastic insert was epoxied (DevCon 2 Ton Epoxy) inside each Niskin to decrease its internal volume and therefore enhance dissolution signals. The powder chamber had an internal volume of 300 ml, and the volume of all components totaled 1.1 liters. Given the flow rate of the pump, water recirculated within the reactor every four minutes, and the residence time of water in the powder chamber was just one minute.

Labeled material was pre-weighed and heat-sealed into packets of 47 mm diameter "Nuclepore" polycarbonate filters (Sigma Aldrich SKU: WHA111116) with pore sizes of 0.8 μm (coccoliths) or 8 μm (calcite) using a Safstar 12" Manual Impulse Heat Sealer (Amazon.com ASIN: B06X6MTLY3). Coccolith and calcite packets contained 0.5-1.5 mg and 10-12 mg of material, respectively. Calcite packets were subdivided in halves with ~5 mg of powder each to prevent clumping. Packets were pressed between two custom plastic mounts to ensure that they remained in the flow path of the water and did not clog the chamber inlet or outlet. The mounts had an open face diameter of 45 mm on each side and were held together by plastic screws at their corners. Up to two mounts could be placed within the reactor side chamber at once. An o-ring was placed in a groove at the top of the chamber and greased with Dow Corning Vacuum Lubricant (Amazon.com ASIN: B001UHMNW0) before bolting on a sealing plate.

The modified reactors were tested before deployment to ensure that they reproduced dissolution rates measured in calcite (Naviaux et al., 2019b) and coccolith (Subhas et al., 2018) benchtop experiments. One of the first issues that was investigated was the effect, if any, of sealing labeled material within Nuclepore packets. Benchtop experiments were conducted following the same methods as outlined above, but material was sealed in 0.8 µm (coccoliths) or 8.0 µm (calcite) Nuclepore packets rather than being dispersed as free powder within the Supelco bag. Dissolution rates of all materials within Nuclepore packets matched those derived from dispersed powder, but the δ^{13}C-DIC signals differed in how they evolved over time (Figure **2.2** inset). Whereas dispersed powder experiments display a period of initial curvature before becoming linear (Subhas et al., 2017), the Nuclepore packets produce a linear dissolution signal over the entire experimental period. The linear signal served to our advantage in the field, as it meant that dissolution rates could be determined from a two-point calculation, regardless of the reaction time.

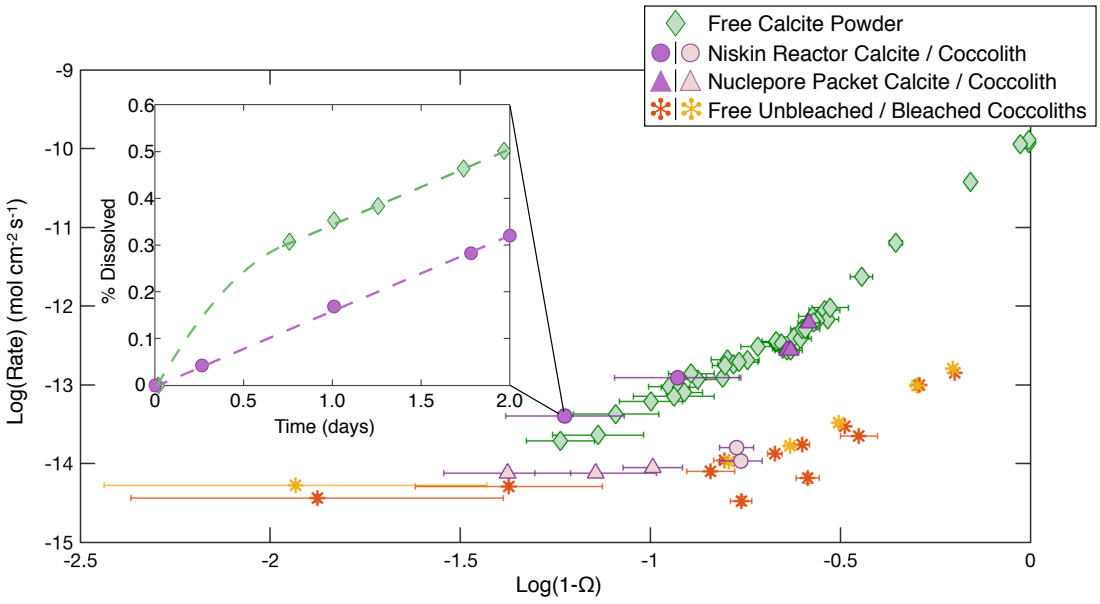

Figure 2.2: The dissolution rates of labeled material at 21°C in Nuclepore mesh packets (triangles) and fully assembled Niskin reactors (circles) agree with dissolution rates of dispersed calcite (diamonds) and coccoliths (stars) in Supelco bags. Rate errors are smaller than the symbols. Inset: The time evolution of the δ^{13}C signal (normalized by percent of

total mass dissolved for comparison) for dispersed powder and powder in Niskin reactors with dashed lines to guide the eye.

We applied the box model of Subhas et al. (2017) to our Nuclepore packet data to understand the linearization of the δ^{13}C-DIC versus time signal. The box model describes calcite dissolution rates using three main reservoirs: a reactive calcite layer, a diffusive boundary layer, and the bulk solution. Simultaneous dissolution and precipitation reactions occur between the reactive layer and the boundary layer, and the balance of fluxes sets the net dissolution rate. The δ^{13}C of DIC is calculated within each reservoir at every timestep. A complete description of the model may be found in the supplement to Subhas et al. (2017). We found that the signal linearization we observed could be explained by an increase in total boundary layer volume from ~1.3 µL to ~1.3 mL. This increase agrees with the approximate volume of each Nuclepore packet. As expected, a further increase of the boundary layer thickness would eventually lead to dissolution inhibition (Figure **2.3**).

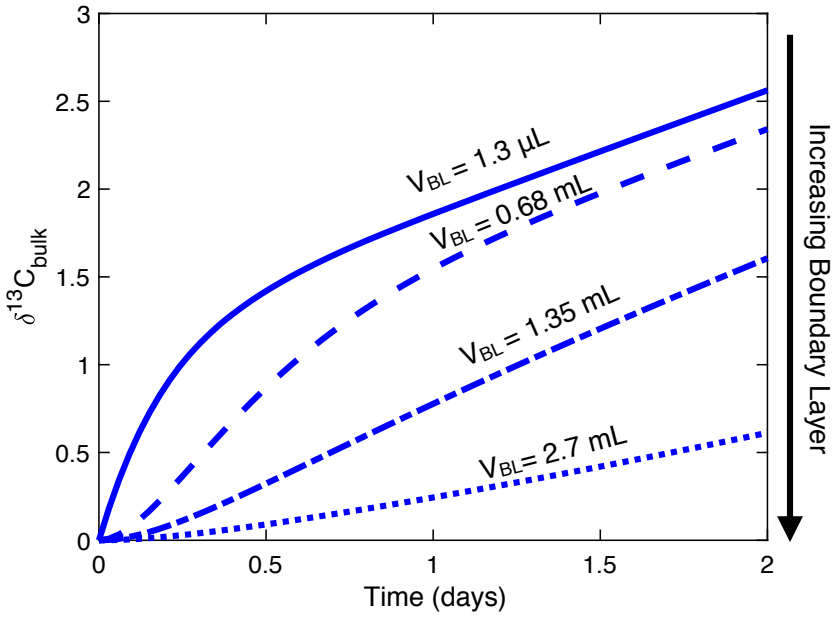

Figure 2.3: Example outputs from the model of Subhas et al. (2017) demonstrating that increased boundary layer volumes (V_{BL}) can cause dissolution signals to appear linear while expressing the same net rate (top three fits) Continuing to increase the boundary layer

eventually inhibits dissolution (bottom fit). These outputs were generated using: R_{Diss} = $5 \cdot 10^{-13}$ moles s^{-1}, R_{Diss}/R_{Precip} =1.12, Mass = 1.5 mg $CaCO_3$, Surface Area (SA)= 900 cm^2 g^{-1}, and varying boundary layer thickness (BL_T) from 10 μm to 20 mm to achieve the desired $V_{BL} = BL_T \cdot SA \cdot Mass$

Having demonstrated that Nuclepore packets themselves did not affect the net reaction rate in the range of saturations expected at sea, we assembled a prototype system with which to test how the packets performed in the *in-situ* reactor. Packets containing 1 mg or 10 mg (coccoliths, calcite) of material were loaded into the reactor side chamber before filling the reactor with 0.2 μm-filtered, $HgCl_2$-poisoned seawater collected off the coast of Catalina Island. Reactors were closed and submerged in a large water bath, at which point the experiment was considered started. Each reactor was sampled regularly over the course of two days for DIC, alkalinity, and δ^{13}C-DIC. Similar to their benchtop counterparts, no change in the alkalinity or DIC of the system was observed, and dissolution rates of both calcite and coccoliths agreed between all methods (Figure **2.2**).

2.2.4 Deployment of Reactors in the Field

In-situ dissolution rates were measured at four of five stations along a transect in the North Pacific from Honolulu, Hawaii to Seward, Alaska. Conductivity, temperature, depth (CTD) casts were taken prior to reactor deployments to determine the background profiles of salinity, temperature, silica, total DIC, alkalinity, pH, and δ^{13}C-DIC. Niskin reactors were attached to the hydrowire and lowered to the desired depths (as determined by the measured background Ω profile) and triggered shut. Another set of *in-situ* reactors was fixed to a weighted wire line, triggered shut at depth, and subsequently attached to surface floats and set free drifting from the ship. Reactor pumps operated continuously and served to flush the bottles with seawater and pre-rinse the labeled material as the Niskins descended through the water column. The Niskin reactors remained closed at depth for 24-58 hours and were sampled for silica, SRP, nitrate, alkalinity, pH, and δ^{13}C-DIC upon recovery. Samples were collected within three minutes of opening the Niskin and were drawn from the bottom port to minimize DIC exchange with ambient air.

2.2.5 Field Sampling Methods

The entire volume of each reactor was utilized for sample analysis. Four 10 ml samples were withdrawn and injected through a 0.2 μm syringe filter into evacuated exetainer vials for δ^{13}C-DIC measurements on a Picarro CRDS. Samples were standardized against pre-weighed amounts of solid ^{13}C-calcite to correct for signal drift over time. The standard deviation on sample replicates was ±0.05‰. The dissolution rate error was calculated from the relative error of the measurement divided by the change in δ^{13}C-DIC signal in the bottle compared to the background water column. Given the precision of the Picarro and the size of the signals, rate errors were typically below 5%. Nevertheless, rate errors could exceed 50% near equilibrium ($0.85 < \Omega < 1$) when dissolution signals were only 0.2-0.3‰ above background.

Immediately following δ^{13}C-DIC sampling, the Byrne group from the University of South Florida withdrew samples for pH and alkalinity measurements. Including the rinsewater, a total of 100 mL were used for pH measurements, and 600 mL for alkalinity. pH_T was spectroscopically measured to a precision of ± 0.001 units using a purified meta-Cresol Purple (mCP) dye indicator according to previously published methods (Liu et al., 2011). Alkalinity was measured following weak acid additions to a precision of ± 3 μmol kg^{-1} using a bromocresol purple dye indicator (Liu et al., 2015). Silica samples were subsequently taken and measured to ± 1.5 μmol L^{-1} using the standard molybdate reduction method (Mullin and Riley, 1955; Parsons, 2013). The remaining liquid was filtered (0.2 μm) into 15 mL Falcon tubes, refrigerated, and stored. These archived samples were sent immediately following the cruise in a cooler with Blue Ice to the University of Maryland for analysis of dissolved nitrate (± 0.25 μmol L^{-1}) and soluble reactive phosphate (± 0.03 μmol L^{-1}) concentrations.

Saturation states in the Niskin reactors were determined from Alk-pH pairs due to sample volume restrictions, rather than from Alk-DIC pairs as was done for laboratory experiments. The difference between the Ω calculated from these pairs will be discussed in greater detail in Section 2.3.1. Alkalinity and pH_T measurements were input into CO2SYS along with the temperature, salinity, depth, SRP, and silica concentrations at which the reactor was

deployed. The saturation state was calculated using the same acid dissociation constants and Monte Carlo error propagation procedure as in the lab, but the precision of the pH measurements meant that Ω was constrained to ± 0.005 units.

2.2.6 Quality Checking Reactors

Reactor failures were diagnosed by comparing the silica concentration in each reactor with that of the background profile as recovered from the CTD cast. Occasionally, bottles did not seal properly when closing and would mix in outside water as they were drawn up through the water column upon recovery. This artificially increased/decreased calculated dissolution rates as heavier/lighter δ^{13}C-DIC water infiltrated the bottle. Silica exhibits a large gradient with depth in the ocean, so leaks were clearly identified (Figure **2.4**) and dissolution data were discarded from any reactors whose silica concentrations deviated from background by more than 1 standard deviation (1.5 µmol L^{-1}).

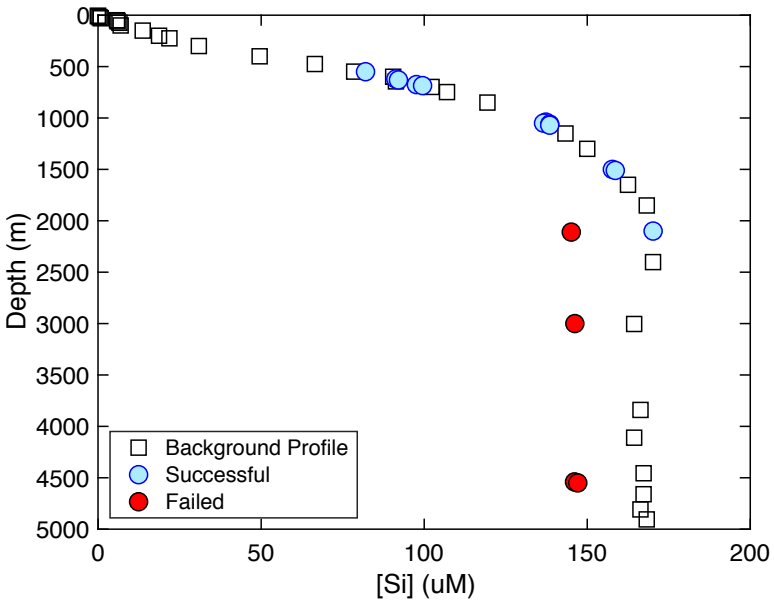

Figure 2.4: Example of how failed reactors were identified at Station 4. Background profiles of silica (squares) were determined prior to reactor deployment. Reactors were sampled for silica after recovery and were deemed successful (blue circles) if their measured silica concentration was within one standard deviation (± 1.5 µmol L^{-1}) of the

background profile. Data from failed reactors (red circles) were easily identified and subsequently discarded.

Miniature pressure/temperature loggers (Star-Oddi: model DST centi-TD) were mounted on each reactor to quantify variations in bottle depth resulting from ship heave and/or wire angle. If these changes were large, they would change the temperature and pressure experienced by the reactor, and therefore the calculated *in-situ* saturation state. Depth variations were on the order of 1-3 m and proved insignificant.

2.3 Results

2.3.1 Discrepancy in Ω Calculations

Consistent with previous reports (Carter et al., 2018, 2013; Fong and Dickson, 2019; McElligott et al., 1998; Patsavas et al., 2015; Raimondi et al., 2019; Williams et al., 2017), shipboard determinations of $\Omega_{(Alk, pH)}$s were systematically offset from $\Omega_{(Alk, DIC)}$s by ~5-10% (Figure **2**.**5**a-d). The shift in the saturation horizon ($\Omega = 1$) exceeded the measurement error at Stations 3, 4, and 5. Given that the CDisK-IV route was similar to the P16 North line from the World Ocean Circulation Experiment (WOCE), we compared our $\Omega_{(Alk, pH)}$ measurements with those from a P16 line conducted in 2015 (EXPOCODE: 33RO20150525) that measured pH spectrophotometrically to ensure that there was not a systematic error in our data. These data exhibit the same offsets as our own (Figure **2**.**6**a). Depth and pH_T are correlated, so the offset between measured and calculated pH increases from near zero at the surface to a maximum around 700-1000m. The offset then decreases deeper in the water column (Figure **2**.**6**b).

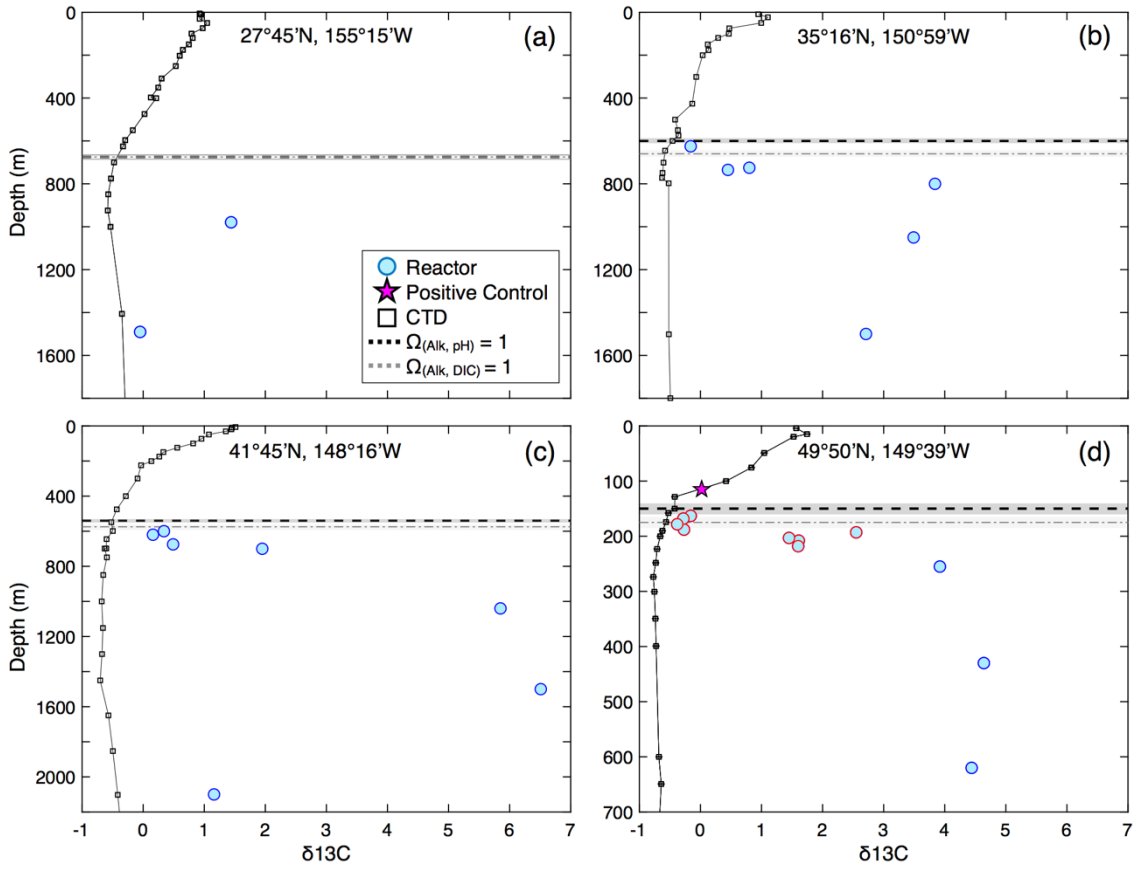

Figure 2.5: Background profiles of $\delta^{13}C$ (squares) measured at (a) Station 2, (b) Station 3, (c) Station 4, (d) Station 5, each plotted with the $\delta^{13}C$ measured in the Niskin reactors upon recovery (circles). Station 5 points outlined in red were deployed after a storm (see text for details). Errors on $\delta^{13}C$ measurements are smaller than the points. The dashed horizontal lines show $\Omega_{(Alk,\ pH)} = 1$ (black) and $\Omega_{(Alk,\ DIC)} = 1$ (grey) with corresponding uncertainty. The offset between $\Omega_{(Alk,\ pH)}$ and $\Omega_{(Alk,\ DIC)}$ exceeded measurement error at Stations 3, 4, and 5. Dissolution was observed when supersaturated for $\Omega_{(Alk,DIC)}$ but undersaturated for $\Omega_{(Alk,\ pH)}$ (b, d). No dissolution occurred when supersaturated for $\Omega_{(Alk,\ pH)}$ (star, d).

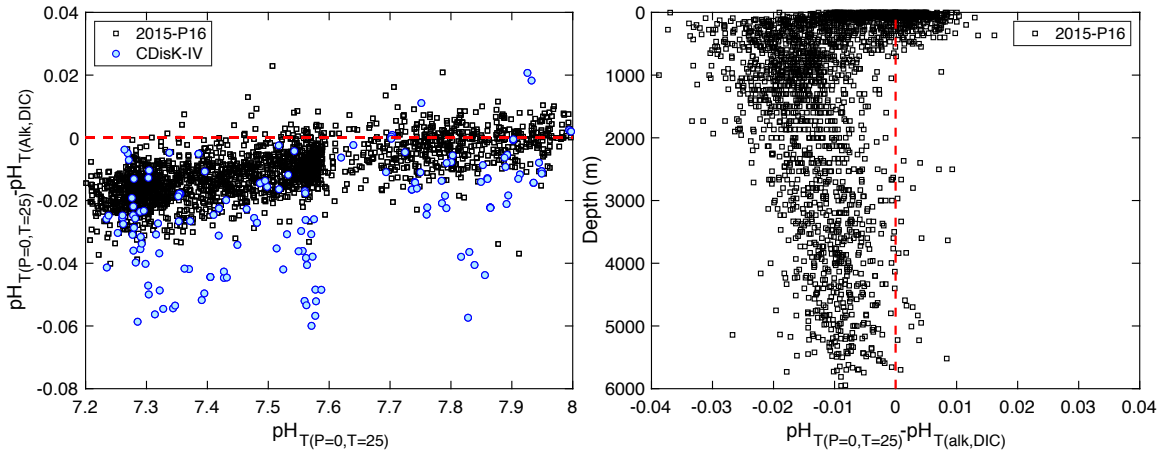

Figure 2.6: (a) The difference between measured pH_T and calculated $pH_{T(Alk, DIC)}$ versus measured pH_T for data collected on CDisK-IV and a 2015-P16 cruise. (b) 2015-P16 pH offsets versus depth.

Results from our dissolution reactors offer an independent verification of the Ω calculation that better describes seawater calcite chemistry. We deployed a reactor at Station 3 (151°W / 35.265°N) where waters were supersaturated according to our own measurements of Alk-DIC, but undersaturated according to Alk-pH. At a depth of 625m, we measured $\Omega_{(Alk, pH)} = 0.90 \pm 0.005$ and $\Omega_{(Alk, DIC)} = 1.07 \pm 0.06$. We observed an enrichment of 0.353‰ above the background profile of ^{13}C-DIC, whereas a positive control reactor deployed at $\Omega_{(Alk, pH)} = 1.29 \pm 0.005$ at Station 5 experienced no enrichment (Figure **2.5**a-3d). Consequently, we use $\Omega_{(Alk, pH)}$ for *in-situ* Ωs. The implications for historical $\Omega_{(Alk, DIC)}$s are discussed in Section 2.4.1.

No discrepancy between Ω calculations was observed when measuring Dickson seawater alkalinity, DIC, and pH under laboratory conditions. This could in part be due to the UV sterilization process destroying organic bases contributing to excess alkalinity, but this is an area for future study. We use uncorrected $\Omega_{(Alk, DIC)}$ for laboratory experiments.

2.3.2 *In-situ* Dissolution Results

Our *in-situ* measurements included 27 calcite reactors (Figure **2.5**a-d) deployed over depths, saturation states, and temperatures of 125-2100 m, Ω = 1.29-0.68, and 1.91-4.87°C, respectively; all of which passed the silica quality check criteria (Table 2.1). Dissolution Δ^{13}C-DIC signals of 0.20-7.18‰ were observed in undersaturated reactors, corresponding with dissolution rates of $1.63 \cdot 10^{-15}$ to $1.01 \cdot 10^{-13}$ mol cm^{-2} s^{-1}. No enrichment of δ^{13}C-DIC was seen in a positive control placed at Ω = 1.29, indicating that our signals represent true dissolution and are not a result of isotopic exchange. SRP and dissolved nitrate samples were collected from hydrocasts along the entire transect, as well as from 25 of the 27 Niskin reactors. Reactor nutrient concentrations varied from 2.1-3.3 μmol L^{-1} SRP and 29.8-46.7 μmol L^{-1} dissolved nitrate, with the lowest concentrations observed in the positive control reactor at 125 m.

Table 2.1: Results from *in-situ* Dissolution Reactors. Alkalinity and pH_T measured to ± 3 μmol kg^{-1} and ± 0.001 units, respectively, resulting in Ω ± 0.005 units

Station	Depth (m)	Alk (μmol kg^{-1})	$pH_{(P=0,T=25,S)}$	T (°C)	$\Omega_{(Alk, pH)}$	Practical Salinity	Phosphate (μm)	Nitrate (μm)	Silica (μM)	Powder Amount (mg)	$\delta^{13}C$ (‰)	Rate·10^{-15} (mol cm^{-2} s^{-1})	Rate error ·10^{-15} (mol cm^{-2} s^{-1})
2	979	2369	7.297	3.94	0.758	34.36	-	-	119.3	20.71	1.99	18.2	1.47
2	1491	2404	7.399	2.87	0.878	34.55	-	-	141.7	11.67	0.29	4.6	2.49
3	625	2306	7.343	4.87	0.897	34.04	2.61	39.91	83.7	21.41	0.36	2.6	1.17
3	725	2326	7.299	4.30	0.789	34.13	3.09	44.12	99.9	20.54	1.41	10.9	0.93
3	735	2327	7.294	4.25	0.777	34.14	3.03	43.05	100.8	10.82	1.07	15.8	1.76
3	800	2343	7.281	4.01	0.746	34.19	3.14	44.76	111.2	22.19	4.36	31.4	1.16
3	1050	2376	7.273	3.27	0.698	34.36	3.31	46.69	134.8	10.93	4.01	59.8	2.23
3	1500	2409	7.329	2.53	0.734	34.54	3.19	46.12	151.9	11.249	3.23	46.9	2.18
4	600	2313	7.335	4.46	0.885	34.06	2.74	41.98	87.3	21.9	0.84	7.9	1.70
4	700	2322	7.254	4.12	0.709	34.15	3.15	44.05	100.3	21.32	2.58	25.3	1.47
4	620	2318	7.323	4.37	0.858	34.08	2.88	40.84	91.3	21.65	0.70	4.8	1.10
4	675	2329	7.313	4.20	0.830	34.13	2.97	42.84	97.6	21.03	1.09	7.8	0.93
4	1040	2380	7.282	3.12	0.717	34.34	3.22	45.62	137.3	21.99	6.52	45.5	1.05
4	1500	2411	7.300	2.44	0.68	34.50	3.26	46.05	157.7	11	7.18	101.0	1.83
4	2100	2431	7.391	1.91	0.749	34.61	3.01	43.98	170.2	11.4	1.58	21.4	1.49
5	255	2293	7.241	3.77	0.745	33.85	2.94	43.12	88.2	21.78	4.65	19.8	0.68
5	430	2323	7.249	3.81	0.741	34.06	3.08	43.98	106.8	20.98	5.27	23.4	0.85
5	620	2347	7.267	3.57	0.750	34.21	3.14	44.26	120.0	21.47	5.05	22.2	0.48
5*	125	2246	7.462	3.95	1.287	33.19	2.11	29.77	47.4	21.21	0.00	0.0	-
						Post Storm Dissolution Measurements							
5	193	2278	7.273	3.68	0.736	33.76	2.86	41.48	78.5	22.02	3.18	25.8	1.21
5	208	2285	7.267	3.69	0.811	33.79	2.91	40.77	80.5	21.27	2.29	19.3	1.18
5	218	2295	7.275	3.71	0.801	33.81	2.89	41.69	82.1	20.79	2.30	19.9	1.29
5	203	2283	7.305	3.69	0.816	33.78	2.66	41.91	80.1	21.03	2.11	18.0	1.19
5	163	2277	7.285	3.64	0.883	33.70	2.75	39.7	71.0	23.23	0.38	2.9	1.28
5	188	2281	7.300	3.67	0.838	33.74	2.85	41.12	77.7	20.68	0.34	3.0	1.49
5	168	2277	7.281	3.65	0.872	33.70	2.71	39.84	74.3	23.17	0.27	2.1	1.14
5	178	2276	7.297	3.67	0.829	33.73	2.69	40.2	75.1	21.61	0.20	1.6	1.23

*Positive control

In-situ calcite dissolution rates exhibited a non-linear dependence on saturation state within the N. Pacific Ocean (Figure **2.7**). Dissolution rates increase gradually with undersaturation until Ω ≈ 0.75-0.80, after which calcite dissolves more rapidly in response to changes in Ω. This change in behavior is evident from the kink in the slope of the log-log plot near log(1-Ω) = -0.7 to -0.6 (Figure **2.7**b). Reactors deployed above the thermocline from 0 – 250 m showed greater rate variability than reactors at 250 – 2200 m. The variability in shallow reactors is related to whether they were deployed before or immediately after a storm that occurred at Station 5 (Figure **2.7** red outline). Whereas *in-situ* dissolution rates measured before the storm (diamonds at 1 - Ω = 0.25) followed the rate vs. Ω trend established at previous stations, data collected immediately following the storm (diamonds closer to equilibrium than 1 - Ω = 0.2) did not. The storm caused the water column temperature, salinity, as well as the oxygen and chlorophyll concentrations to all change dramatically. We hypothesize why the rate data are more scattered in Section 2.4.3.

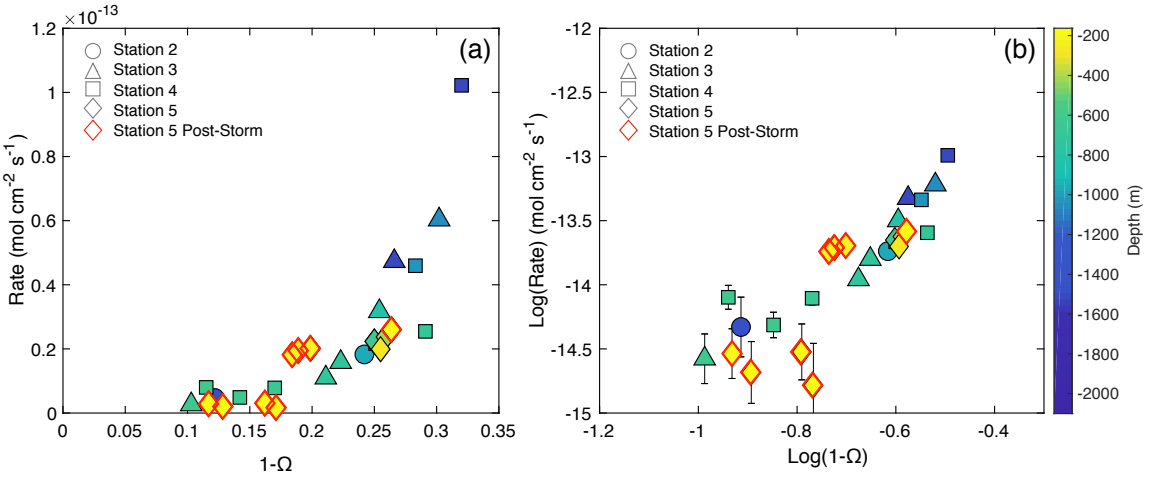

Figure 2.7: Dissolution rate (mol cm^{-2} s^{-1}) of synthetic calcite versus (a) 1-Ω and (b) Log(Rate) versus Log(1-Ω). Points are colored by their deployment depth, and reactors deployed after a storm at Station 5 are outlined in red. Error bars are plotted for both rate and Ω, but are frequently smaller than the symbols.

2.3.3 Laboratory Results

Dissolution rates measured in Dickson seawater at 5° C exhibit the same trends versus 1-Ω as documented *in-situ* (Figure **2**.**8**a), but rates measured in the laboratory are faster by a factor of ~4. No dissolution was observed in the lab at $\Omega = 1.05 \pm 0.02$ (not shown). Once undersaturated, 5°C laboratory dissolution rates increase from 0 to $\sim 1 \cdot 10^{-13.5}$ mol cm^{-2} s^{-1} by $\Omega = 0.99$ (Figure **2**.**9**) and remain nearly independent of Ω until $\Omega_{crit} \approx 0.8$. The offset between lab and *in-situ* rates is due to some difference in water chemistry that will be explored below, rather than a methodological bias, as experiments run soon after the cruise in archived N. Pacific seawater produced comparable rates as measured *in-situ* (Figure **2**.**8**b).

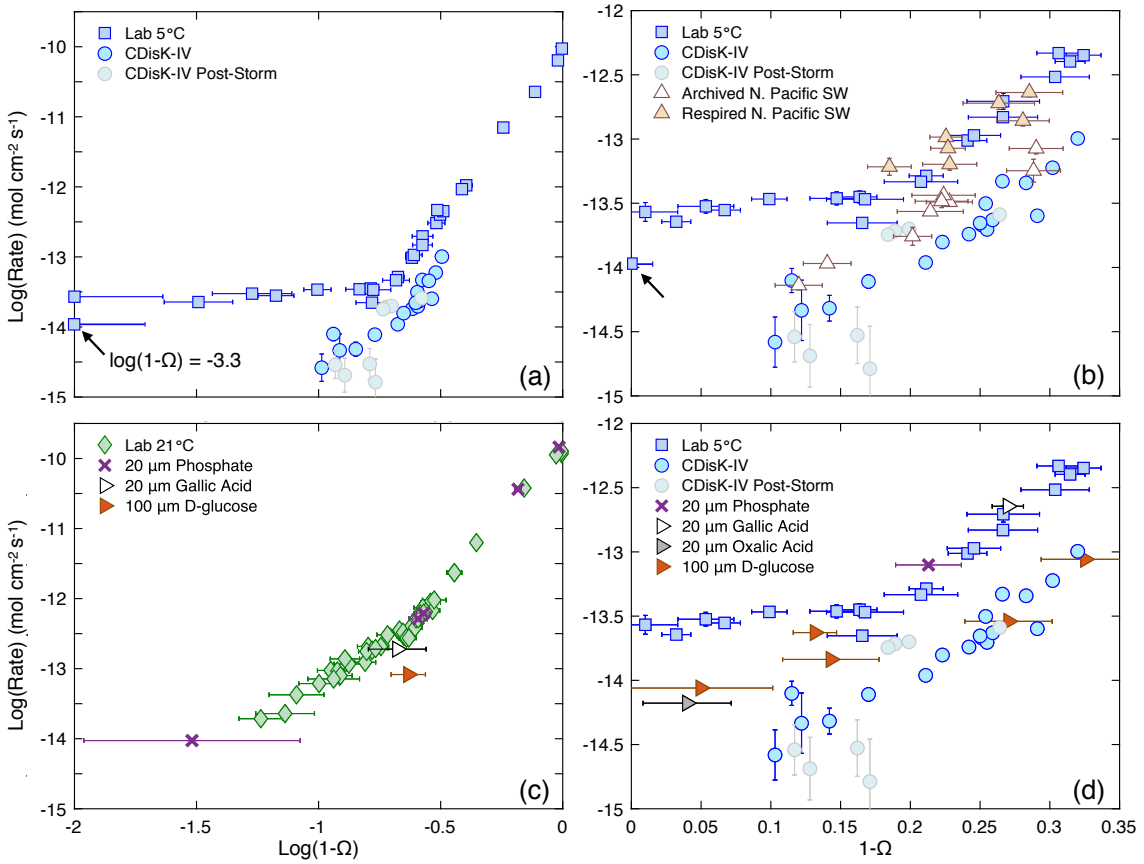

Figure 2.8: Comparisons of Log(Rate) (mol cm^{-2} s^{-1}) versus either Log(1-Ω) (a, c) or 1-Ω (b, d) for calcite dissolution experiments in the lab and *in-situ*. (a) Dissolution at 5°C in poisoned, filtered, UV-treated Dickson seawater (squares) versus dissolution measured *in-situ* in the N. Pacific (circles). The light grey circles are *in-situ* dissolution measurements made after the storm at Station 5. (b) Dissolution rates at 5°C in archived North Pacific seawater before (white triangles) and after (brown triangles) DIC increased by 152 µmol kg^{-1}. The arrow in (a) and (b) indicates a point at Log(1-Ω) = -3.3 which may be more clearly seen in the expanded version of this figure (Fig. S3). (c) Dissolution rates in Dickson seawater at 21°C (diamonds, from Naviaux et al. 2019) and with Dickson seawater spiked with different potential inhibitors. (d) The same as (c), but versus 1-Ω and with experiments conducted at 5°C. The point at Log(1-Ω) = -3.3 is left off of (d) for visual clarity.

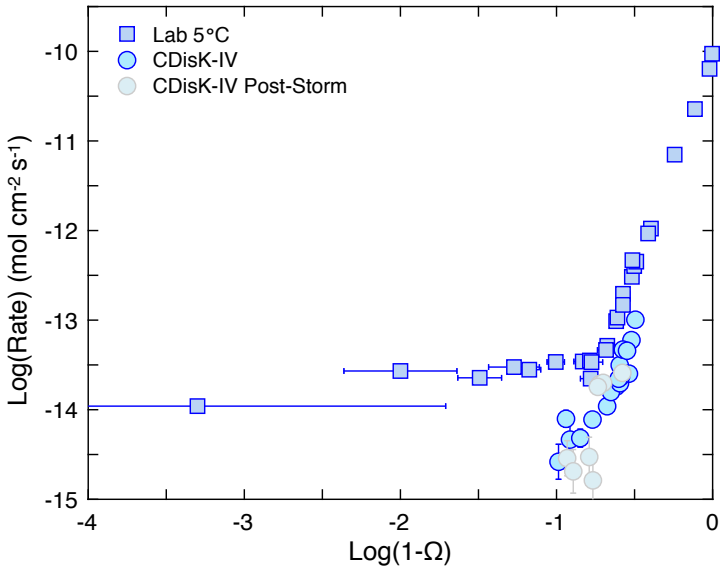

Figure 2.9: Expanded version of Figure 2.8a of Log(Rate) (mol cm^{-2} s^{-1}) versus Log(1-Ω) for calcite dissolution experiments in the lab and *in-situ*. No dissolution was observed at Ω = 1.05 ± 0.02 in the lab, but dissolution did occur at Log(1-Ω) = -3.3. The point at Log(1-Ω) = -3.3 is within error of Ω = 0, but still serves to demonstrate a slight Ω dependence for dissolution rates very near equilibrium.

Despite being stored in the dark in gas impermeable bags without headspace, the DIC of the archived seawater was found to have increased by 152 µmol kg^{-1} after 3 months. A leak in the bag would allow water to evaporate and alter both DIC and alkalinity, but the alkalinity of the water remained constant. No further change in water chemistry occurred over the following 6 months. Experiments conducted in the altered, archived seawater produced dissolution rates that matched the rates measured in Dickson seawater (Figure **2.8**b). We refer to this altered, archived seawater as "respired," and discuss our reasoning and the implications of the faster dissolution rate in Section 2.4.3.2.

Spiking Dickson seawater with different potential inhibitors had variable effects on dissolution, with the addition of 100 µmol kg^{-1} D-glucose slowing rates to comparable values as those measured in the N. Pacific (Figure **2.8**c, d). The degree of inhibition varied by compound, with temperature, and with distance from equilibrium. Glucose slowed calcite

dissolution rates by a factor of ~4 at 5 and 21°C for $\Omega < 0.8$, but had less of an effect closer to equilibrium. Gallic acid and orthophosphate had no effect on dissolution at either 5 or 21°C, but oxalic acid slowed rates near-equilibrium at 5°C by a factor of ~2. As discussed below, we attribute the variable effects of each compound to changes in dissolution mechanism across different saturation ranges.

2.4 Discussion

2.4.1 Implications for Ocean Saturation State

Our dissolution experiments suggest that $\Omega_{(alk,\ DIC)}$ calculations systematically overestimate *in-situ* calcite saturation. Three pieces of evidence indicate that the more undersaturated values for *in-situ* $\Omega_{(Alk,\ pH)}$ better capture marine calcite chemistry than $\Omega_{(Alk,\ DIC)}$: (1) At sea, carbonate dissolution was documented at Stations 3 and 5 in waters that were supersaturated for $\Omega_{(Alk,\ DIC),}$ but undersaturated for $\Omega_{(Alk,\ pH)}$. No dissolution occurred when waters were supersaturated by $\Omega_{(Alk,\ pH)}$. (2) *In-situ* dissolution exhibits a kink in rate at the same Ω_{crit} as in the lab, but only when comparing *in-situ* $\Omega_{(Alk,\ pH)}$ and lab $\Omega_{(Alk,\ DIC)}$. (3) Laboratory dissolution rates measured in archived N. Pacific seawater were comparably slow as those measured *in-situ*, despite using Alk-DIC pairs in the lab to place the rates in Ω space.

Until new values for the carbonic acid dissociation constants are experimentally verified or refined (Fong and Dickson, 2019), there will be systematic offsets between datasets depending on their choice of CO_2 chemistry input parameters. To illustrate this point, we plot the calcite Ω profiles at each of our stations in Figure **2.10** alongside $\Omega_{(Alk,\ pH)}$ from the 2015-P16 cruise, and $\Omega_{(Alk,\ DIC)}$ from the Global Data Analysis Project v2 (GLODAP, Olsen et al., 2016) database. The profiles of $\Omega_{(Alk,\ pH)}$ agree quite well with one another, but they are clearly offset from GLODAP $\Omega_{(Alk,\ DIC)}$. The discrepancy extends to abyssal waters, and therefore cannot be due to ocean acidification, which has only extended to intermediate waters in the Pacific (Byrne et al., 2010). Proxies thought to represent marine carbonate chemistry over glacial time periods, such as boron/calcium ratios, are frequently calibrated to GLODAP $\Omega_{(Alk,\ DIC)}$ (Yu and Elderfield, 2007). Whereas the uncertainties in the proxies themselves may be large, our *in-situ* dissolution results suggest a consistent offset in Ω

accuracy, rather than precision, with $\Omega_{(Alk, DIC)}$ being biased towards more saturated values. Caution should be used when applying such proxies until a thorough reevaluation of marine carbonate system parameters (Fong and Dickson, 2019) has been conducted.

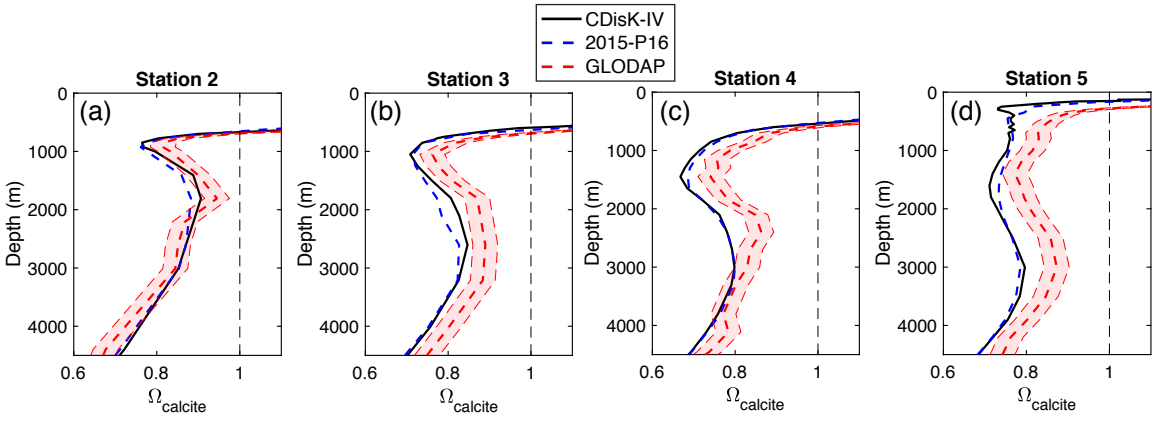

Figure 2.10: (a)-(d) Profiles showing the systematic offset between $\Omega_{(Alk, pH)}$ (from CDisK-IV and 2015-P16) and $\Omega_{(Alk, DIC)}$ (from GLODAP) at each station. The GLODAP profiles were derived from 2006-P16 cruise measurements (EXPOCODE: 325020060213) of Alk and DIC data flagged as "acceptable." Ω was calculated using the same CO_2 system parameters as discussed in the main text. GLODAP Alk and DIC were measured to better than ± 3 µmol kg^{-1}, corresponding with $\Omega_{(Alk, DIC)}$ ± 0.03. Measurement errors for $\Omega_{(Alk, pH)}$ are ± 0.005 and are not visible.

2.4.2 Laboratory versus *In-situ* Dissolution Rates

Dissolution in the lab and *in-situ* follow the same rate behavior versus undersaturation and undergo a change in surface mechanism at the same $\Omega_{critical}$ (Figure **2.11**a). Fits to the data are presented in Table 2.2. We use $\Omega_{critical} = 0.8$ rather than the 0.75 used previously (Naviaux et al., 2019b), as additional laboratory data collected at 5°C support a transition closer to equilibrium. The near-equilibrium fit to the *in-situ* data is constrained by only a few measurements, so the reaction order changes slightly depending on whether $\Omega_{critical} = 0.75$ or $\Omega_{critical} = 0.8$ is used. Nevertheless, this difference does not affect our overall analysis. In the traditional Rate = $k(1-\Omega)^n$ equation, dissolution in the lab and *in-situ* are both weakly dependent on undersaturation from $0.8 < \Omega < 1$, after which the reaction order increases to ~4.7. The log of the rate constant necessarily increases with n from -13.1 ± 0.2 to -10.0 ± 0.1

mol cm^{-2} s^{-1} for the 5°C lab data, and from -13.5 ± 0.4 to -10.8 ± 0.4 mol cm^{-2} s^{-1} for the *in-situ* data. We emphasize that the kink at $\Omega_{critical} \approx 0.8$ means that the use of a single n and k pair will systematically misfit dissolution rates.

Table 2.2: Fits to Empirical Rate Equation				
Condition	1 > Ω > 0.8		0.8 > Ω > 0	
	$Log_{10}k$ (mol cm^{-2} s^{-1})	n	$Log_{10}k$ (mol cm^{-2} s^{-1})	n
Laboratory 5°C	-13.1 ± 0.2	0.11 ± 0.1	-10.0 ± 0.1	4.76 ± 0.09
N. Pacific *In-situ*	-13.5 ± 0.4	0.8 ± 0.5	-10.8 ± 0.4	4.7 ± 0.7

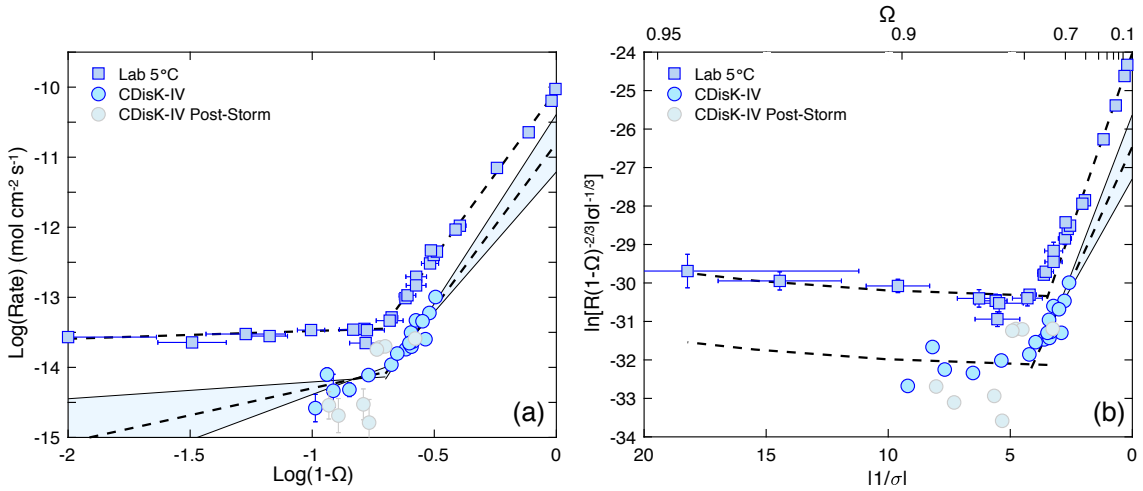

Figure 2.11: (a) Log(Rate) (mol cm^{-2} s^{-1}) versus Log(1-Ω) for our lab and *in-situ* measurements. The fits to the data are from Table 2.2. (b) The normalized dissolution rate (m s^{-1}) versus $\left|\frac{1}{\sigma}\right|$. The x-axis is reversed from Naviaux et al. (2019) to ease comparison with (a). Tick marks are included at intervals of 0.1 Ω units, with one extra tick at Ω=0.95 to emphasize the non-linear nature of the $\left|\frac{1}{\sigma}\right|$ axis. Data from $20>\left|\frac{1}{\sigma}\right|>4.4$ (0.95>Ω>0.8) are fit to Eq. (2b) for dissolution by the retreat of pre-existing steps. Data from $4.4>\left|\frac{1}{\sigma}\right|>0$ (0.8>Ω>0) are fit to Eq. (2a) for dissolution by homogenous etch pit formation. Fitting parameters are in Table 2.3.

The 2D nucleation framework from Dove et al. (2005) allows for the identification of dissolution mechanisms and surface energetics by plotting normalized dissolution rates

versus $\left|\frac{1}{\sigma}\right|$ and fitting to Eq.'s (2a) and (2b) (Dong et al., 2018; Naviaux et al., 2019b; Subhas et al., 2018, 2017) (Figure **2.11**b). The fits to the data and the values for each parameter are available in Table 2.3. Normalized dissolution rates in the lab and *in-situ* are non-linear for $\left|\frac{1}{\sigma}\right| > 4.4$ ($\Omega > 0.8$), consistent with dissolution proceeding from the retreat of pre-existing steps and screw dislocations (Eq. 2b). The *in-situ* data can be fit by Eq. (2b) using the same step edge free energy, α (= -0.5 mJ m^{-2}), as the 5°C lab data, but the *in-situ* data require a step kinetic coefficient, β, that is one order of magnitude lower ($5 \cdot 10^{-8}$ versus $3 \cdot 10^{-7}$ m s^{-1}). Both datasets become linear upon surpassing $\left|\frac{1}{\sigma}\right| \approx 4.4$ ($\Omega = 0.8$), consistent with a mechanistic transition from step retreat to homogenous etch pit formation. The slopes of the data, which are proportional to the step edge free energies, are similar in this far-from-equilibrium region, but the intercepts differ by 2 - 4 natural log units. The intercept of Eq. (2a) is set by both β and the number of active etch pit nucleation sites, n_s, so we make the simplifying assumption that n_s is the same both in the lab and *in-situ* ($5 \cdot 10^{12}$ sites m^{-2}, Naviaux et al., 2019). This assumption is justified because the *in-situ* dissolution rates are slower across each mechanistic regime, and β is the only kinetic variable appearing in both Eq. (2a) and (2b) that affects the magnitude of the rate. Our fits suggest that the components slowing dissolution *in-situ* inhibit the surface retreat rate via β, while minimally affecting the step edge free energies and Ω_{crit}s for the transition between dissolution mechanisms.

Table 2.3: Fits to 2D Nucleation Equations							
Condition	Step Retreat (Eq. 2b) $\left\|\frac{1}{\sigma}\right\| > 4.4$ ($\Omega > 0.8$)			Etch Pit Formation (Eq. 2a) $4.4 > \left\|\frac{1}{\sigma}\right\|$ ($0.8 > \Omega$)			
	$\beta \cdot 10^{-7}$ (m s^{-1})	α (mJ m^{-2})		$\beta \cdot 10^{-3}$ (m s^{-1})	α (mJ m^{-2})		
Laboratory 5°C	3 ± 0.5	-0.5		4.0 ± 0.02	-37.6 ± 0.7		
N. Pacific *In-situ*	0.4 ± 0.2	-0.5		0.35 ± 0.2	-32 ± 3		
Shared Constants							
m[1] (m)	h[2] (m)	a[2] (m)	ω[3] (m^3)	P[4] (m)	K_{sp}'[5] (mol^2 kg^{-2})	C_e[6] (atoms m^{-3})	n_s[1] (sites m^{-3})
1	$3 \cdot 10^{-10}$	$3 \cdot 10^{-10}$	$6.12 \cdot 10^{-29}$	$1.88 \cdot 10^{-9}$	$4.309 \cdot 10^{-7}$	$2.595 \cdot 10^{22}$	$5 \cdot 10^{12}$

[1]Naviaux et al. (2019), [2]Teng (2004), [3]calculated from calcite density of 2.71 g cm^{-3}, [4]estimated assuming burgers vector $b = mh$, $P = 2\pi b$ analogously to Dove et al., 2005, [5]K_{sp}' at 5°C from Mucci (1983), [6]from $K_{sp}'/[Ca^{2+}]$, where $[Ca^{2+}] = 0.01$ M, Naviaux et al (2019)

Dong et al. (2018) documented a pressure dependent enhancement of calcite dissolution rates in the lab, but we are unable to evaluate this effect *in-situ*. The magnitude of the rate enhancement reported by Dong et al. (~2-4x at 700 dbar) is comparable to the scatter of our *in-situ* measurements pre/post-storm. Whereas *in-situ* dissolution rates generally increase with depth (Figure **2.7**), we do not have enough data to identify a change in rate due to Ω, versus a rate enhancement due to pressure. This was a goal of our cruise, but weather and ship problems prevented us from completing this part of the work.

2.4.3 Role of Inhibitors

2.4.3.1 Soluble Reactive Phosphate (SRP)

Our results show that SRP does not inhibit bulk calcite dissolution rates at any of our investigated temperatures or saturation states, even when concentrations exceed modern ocean water column values by an order of magnitude (Figure **2.8**). The idea that SRP is the primary inhibitor in our system is also challenged by our results in archived N. Pacific seawater. The archived seawater had low SRP similar to our laboratory Dickson seawater (0.293 vs. 0.3-0.5 μM), but dissolution rates were slower than in the laboratory water.

SRP is still cited as the canonical calcite dissolution inhibitor (Finneran and Morse, 2009; Morse et al., 2007), but we are not the first to call this into question. Seminal works by Berner and Morse (1974) and Sjöberg (1978) reported SRP inhibiting calcite dissolution rates at concentrations < 10 μM, but later experiments by Walter and Burton (1986) saw no inhibitory effects for SRP < 50 μM. More recently, an atomic force microscopy study by Klasa et al. (2013) documented inhibition for ammonia salts of phosphate, but not for sodium salts typically used in previous studies.

A plausible hypothesis proposed by Walter and Burton (1986) is that dissolution inhibition by SRP is only significant at pHs > 8. The dominant forms of SRP above pH ~ 8 are HPO_4^{2-} and PO_4^{3-}, and seawater precipitation studies have shown that the concentration of PO_4^{3-} ions (Mucci, 1986), and the ratio of PO_4^{3-} to HPO_4^{2-} ions (Burton and Walter, 1990), are better predictors of rate inhibition than the total SRP concentration. The pH-dependence hypothesis may explain why inhibition was reported by Sjöberg (1978, pH = 8.3), but not for this study (pH = 5.5 – 7.5), Walter and Burton (1986, pH = 7.0 – 7.5), or Klasa et al. (2013, pH = 5 and 8), but it cannot explain all results. Though it is possible that the inhibition documented by Berner and Morse (1974, pH 7 – 7.5) was due to pH-probe drift (Walter and Burton, 1986), Alkattan et al. (2002) more recently reported SRP concentrations ≥ 50 μM inhibiting calcite dissolution rates from pH -1 – 3.

We acknowledge that the effects of SRP are complex, and that our results only extend to its role, or lack thereof, in seawater calcite dissolution kinetics. SRP adsorbs to the calcite surface (de Kanel and Morse, 1978; Millero et al., 2001) and has a clear inhibitory effect on calcite precipitation kinetics (Dove and Hochella, 1993). Klasa et al. (2013) did not report any change in the calcite surface retreat rate in undersaturated solutions, but the presence of SRP significantly altered etch pit morphology. Seawater calcite dissolution rates may not be impacted by SRP concentrations ≤ 20 μM from pH 5.5 – 7.5, but it is important to consider the effects of SRP on precipitation rates and surface morphology when studying marine carbonates.

2.4.3.2 Dissolved Organic Carbon

All of our results point to DOC being the primary class of compounds inhibiting calcite dissolution rates in natural seawater. Increased SRP concentrations had no effect on dissolution rates, but the addition of DOC in the form of D-glucose and oxalic acid caused laboratory-derived dissolution rates to slow to comparable values as those observed *in-situ*. This conclusion is further supported by the experiments in archived N. Pacific seawater, in which calcite dissolution rates were initially slow, but matched rates in Dickson seawater after its DIC increased. The archived water was stored in a gas impermeable bag and did not leak, so we propose that the dissolution rate increased due to the quantitative conversion of non-redfieldian organic matter to DIC by respiration. This hypothesis is based on two pieces of evidence: (1) The temporal pattern of the archived water DIC is similar to a biological activity curve. Exponential respiration rapidly consumes available resources, the non-redfieldian nature of which is suggested by the lack of change in alkalinity despite the 152 μmol kg^{-1} change in DIC. No further growth occurs after the limiting resource is exhausted, and the DIC and alkalinity of the archived seawater remained constant for the following 6 months. We speculate that O_2 was the limiting resource, as the DIC increase was comparable to the seawater O_2 concentration before it was transferred to an airtight bag. (2) The chemical addition experiments revealed that DOC can inhibit calcite dissolution kinetics. Organic respiration is a potential mechanism by which an inhibitory organic compound could be converted to a non-inhibitory form in our closed system.

Inhibition by DOC qualitatively explains the internal variability of the shallow and post-storm *in-situ* dissolution measurements. Dissolution reactors deployed below 250 m fell on a consistent rate versus Ω trend, but reactors above 250 m at Station 5 did not (Figure **2.7**). This has parallels to vertical profiles of DOC, where concentrations as high as 80-250 μM in surface waters decrease rapidly to < 50 μM below ~200 - 400 m (Druffel et al., 1992; Hansell, 2013; Hansell and Carlson, 1998a). Furthermore, a phytoplankton bloom was observed after the storm at Station 5, and blooms are known to be associated with dramatic increases in DOC (Eberlein et al., 1985; Hansell and Carlson, 1998b; Ittekkot et al., 1981; Kirchman et

al., 2001)**.** The shallow reactors would have been most susceptible to the variable DOC concentrations after the storm, as well as any potential effects from the phytoplankton bloom.

The conclusion that DOC inhibits calcite dissolution appears to stand in contrast with previous reports (Morse, 1974; Oelkers et al., 2011; Sjöberg, 1978), but, as evident from the fitted *k* values in Table 2.2, dissolution rates in natural seawater are only slower by a factor of ~4 compared to those in poisoned, filtered, UV-treated seawater. It is possible that the ~10% error in Ω and/or rate typical of older studies (Morse, 1974; Sjöberg, 1978) obscured the inhibitory effect of DOC, especially close to equilibrium where rates would have been near the detection limit. For more recent studies (Jordan et al., 2007; O. S. Pokrovsky et al., 2009), the disagreement may simply be due to what the authors deemed "significant" inhibition. For example, Oelkers et al. (2011) measured calcite dissolution kinetics in 0.1M NaCl in the presence of 18 different organic ligands. The authors reported "negligible" ~2.5x rate inhibition by gum xantham, but this decrease is of the same magnitude as the rate offset we document in natural seawater. Finally, biological activity has been shown to enhance DOC adsorption onto calcite (Zullig and Morse, 1988), so it is possible that studies in sterile solutions have underestimated the amount of DOC adsorption, and therefore dissolution inhibition, that occurs in natural environments.

DOC in the ocean is abundant and poorly characterized (Aluwihare et al., 2002; Benner et al., 1992; Hansell, 2013; Hansell and Carlson, 1998b; Repeta et al., 2002), so there are likely a wide range of compounds that can inhibit calcite dissolution kinetics. The inhibitor concentrations in this study were specifically chosen to maximize any potential inhibitory response. Our results therefore only establish that DOC, as a class of compounds, can explain why *in-situ* dissolution rates are slower than in the lab. A study in seawater analogous to that of Oelkers et al. (2011) in dilute solutions will be necessary to further narrow the field of potential dissolution inhibitors.

2.4.4 Implications for *In-situ* Calcite Dissolution Rates

Our data envelope all previous *in-situ* dissolution measurements of inorganic calcite, regardless of depth or location (Figure **2**.**12**). Honjo & Erez (1978) measured the dissolution

rates of crushed calcite in the Sargasso Sea (33°22.0'N, 55°00.8'W) at a depth of 5518 m, and their two overlapping points fall directly upon our 5°C laboratory data. Troy et al. (1997) used AFM to quantify the dissolution rate of Iceland spar calcite moored at Station ALOHA (22°45'N, 158°W) from 350-1000 m. Their rates are more consistent with the slower dissolution rates we measured *in-situ*. Peterson (1966) measured the mass loss of moored calcite spheres in the Central Pacific (18°49'N, 168°0.31'W) after 4 months. Saturation data were not reported by Peterson, so we plot his points against $\Omega_{(Alk,\ pH)}$ measured on the 2015-P16 cruise at the same latitude (18°49'N, 152°W). When doing so, Peterson's rates span the range between our lab and *in-situ* measurements and reveal a reaction rate kink at the same Ω_{crit}. The P16 $\Omega_{(Alk,\ pH)}$ is used, rather than the $\Omega_{(Alk,\ DIC)}$ at the location of Peterson's experiments from Takahashi (1975), due to the discrepancy in the Ω calculations that was discussed in Section 2.3.1. The difference is small, but plotting against the Takahashi Ω shifts the data ~0.02 units closer to equilibrium (Figure **2**.**13**). We note that the Takahashi Ω value implies that the dissolution measured by Peterson from 500-2000 m occurred in supersaturated waters, whereas $\Omega_{(Alk,pH)}$ does not. Finally, Fukuhara et al. (2008) moored crushed calcite in the Central Pacific (29°59.95'N, 175°00.17'E) from 1668-5167 m. The data are not included in Figure **2**.**12**, as the authors did not report the surface area of their material. Nevertheless, the rates are similar to our own (order of $\sim 1 \cdot 10^{-14}$ mol cm^{-2} s^{-1}) if we assume the same surface area as that measured by Honjo & Erez for crushed calcite (0.35 m^2 g^{-1}).

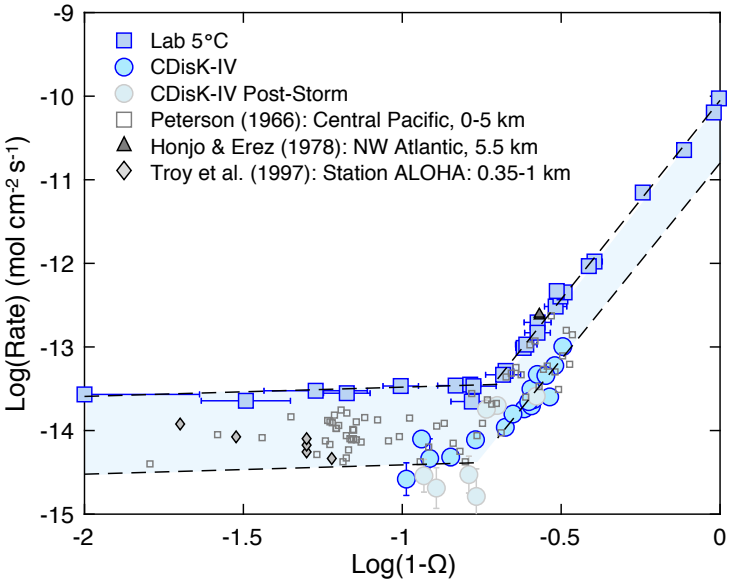

Figure 2.12: Compilation of *in-situ* dissolution rates of inorganic calcite overlaid upon our measured lab and *in-situ* rates. The rate data from Honjo & Erez (1978) are from their Table 2 for reagent calcite and large calcite crystals, and Ω is from Takahashi (1975). Rate and Ω data for Troy et al. (1997) are from their Figure 12. Troy et al. documented dissolution above the saturation horizon, but these data are not included. Peterson (1966) rate data are from Fig. 2 of his paper, with Ω from 2015-P16 at a comparable location (see text for details, as well as Fig. S5). The shaded area represents theoretical bounds for dissolution in low DOC (top curve) and high DOC (bottom curve) seawater. The bounds are fit by the 5°C *n* and *k* values in Table 1. The lower bound is fit by $R=10^{-14.3\pm0.2}(1-\Omega)^{0.11\pm0.1}$ for $0.8 < \Omega < 1$, and $R=10^{-10.8\pm0.4}(1-\Omega)^{4.7\pm0.7}$ for $0 < \Omega < 0.8$.

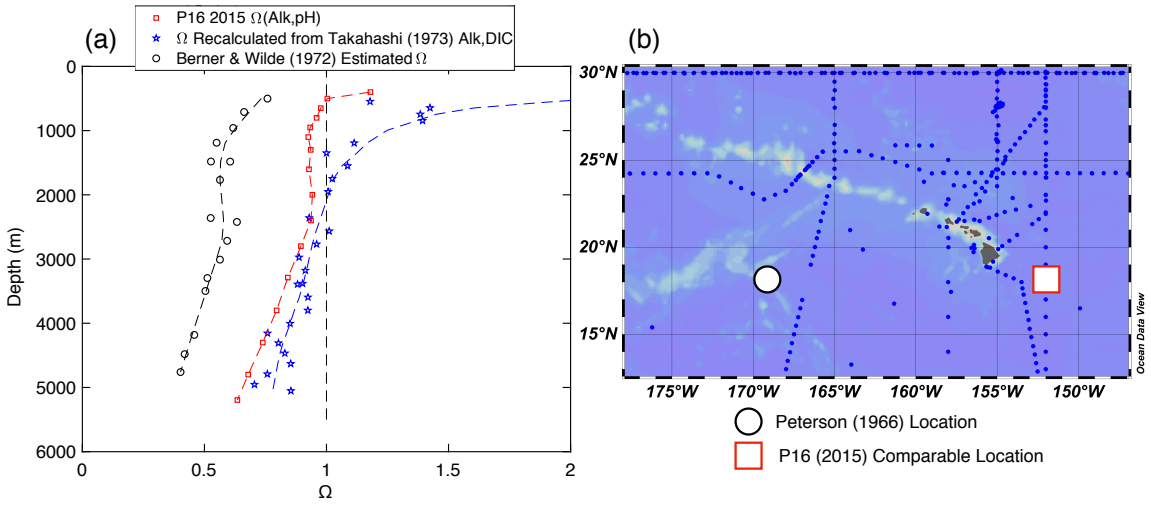

Figure 2.13: (a) Estimates for the saturation state at the location of Peterson's (1966) moored calcite spheres. Ω estimates by Berner & Wilde (1972) are from their Table 2 and were based upon measurements of pH and carbonate alkalinity near Peterson's deployment site. Takahashi subsequently returned to the Peterson deployment site in 1973 and measured the total alkalinity, DIC, salinity, and temperature. The Takahashi data was taken from GLODAP v2 Bottle Data (Station ID: 33541, EXPOCODE: 318M19730822) and input into CO2SYS using the carbonate system parameters outlined in the main text. The resulting $\Omega_{(Alk, DIC)}$ is similar to the ΔpH profile in Fig. 8 published by Takahashi (1975), but our calculated Ω has a shallower slope versus depth. The profiles match to a depth of 3000 m, but we calculate Ω=0.7 at 5000 m compared with Takahashi Ω = 0.4 (ΔpH = 0.2, Fig. 8 of their paper). Given the issues with $\Omega_{(Alk, DIC)}$ discussed in the text, Peterson's data were plotted versus $\Omega_{(Alk, pH)}$ measured at the same latitude on a 2015 P16 cruise. (b) The P16 line was 20° East of the Peterson site, but the profile is similar in shape to the original Berner & Wilde estimate. Peterson documented dissolution from 500-2000 m, and these depths are undersaturated by P16 $\Omega_{(Alk, pH)}$, but supersaturated for Takahashi $\Omega_{(Alk, DIC)}$.

The heterogeneity of the nature and concentrations of DOC in the ocean implies that calcite dissolution rates possess an innate degree of variability. In fact, some of this variability was documented in our post-storm data. Given our understanding of DOC as a source of rate variance, our lab and *in-situ* data may be considered end member cases for dissolution rates in low/high DOC waters, and can help explain differences among previous *in-situ* rate measurements. Studies producing relatively slow dissolution rates used calcite material that was exposed to high DOC surface seawater as it was lowered through the water column (Peterson, 1966; Troy et al., 1997; Fukuhara et al., 2008) and may be described by the *in-situ*

parameters in Table 2.2. The historical data compilation supports the use of a small reaction order for $0.8 < \Omega < 1$, so we fit the lower bound using the same n as our laboratory data, such that $R_{(mol\ cm\text{-}2\ s\text{-}1)} = 10^{-14.3\pm0.2}(1\text{-}\Omega)^{0.11\pm0.1}$ for $0.8 < \Omega < 1$. The Dickson seawater used in the lab was filtered, poisoned, and UV treated, and represents the upper bound for dissolution rates in low DOC waters. This upper bound is fit by the laboratory n and k values in Table 2.2. Honjo and Erez (1978) present a useful *in-situ* example of this upper bound, as the authors prevented their material from contacting ambient seawater until reaching the desired depth. Their crushed calcite was exposed only to low DOC abyssal waters, and the rate that they recovered matched the upper limit of our lab measurements. For the purposes of modeling water column calcite dissolution, we recommend that the lower bound be used, as natural carbonates form in high DOC surface waters and dissolve as they sink.

2.5 Conclusion

We dissolved ^{13}C-labeled inorganic calcite both in the lab and *in-situ* across a transect of the N. Pacific. We find that $\Omega_{(alk,\ pH)}$ provides a better description of marine carbonate chemistry than $\Omega_{(alk,DIC)}$, and in doing so, we echo the need for a thorough reevaluation of pK_1', pK_2', and the total boron-salinity ratio (Fong and Dickson, 2019). When uncorrected, the use of $\Omega_{(alk,DIC)}$ can shift down the $\Omega = 1$ saturation horizon by ~5-10%. Caution should therefore be used when calibrating proxies to GLODAP $\Omega_{(alk,DIC)}$ water chemistry. Calcite dissolution rates exhibited the same dependence on undersaturation in the lab and *in-situ*, with fits to the empirical $Rate = k(1\text{-}\Omega)^n$ equation yielding reaction orders of $n < 1$ for $0.8 < \Omega < 1$, and $n = 4.7$ for $0 < \Omega < 0.8$. The change in the reaction order at 5°C at $\Omega_{crit} = 0.8$ is consistent with a change in dissolution mechanism from step retreat to homogenous etch pit formation. *In-situ* dissolution rates were slower than those in the lab by a factor of ~4 due to the presence of natural inhibitors. Chemical spike experiments revealed that soluble reactive phosphate had no effect on calcite dissolution kinetics under our experimental conditions, but the addition of DOC in the form of oxalic acid and D-glucose slowed dissolution to match *in-situ* observations. DOC appears to act by inhibiting the rate of retreat of the calcite surface. Our lab and *in-situ* rate data form an envelope around previous *in-situ* dissolution measurements and may be considered outer bounds for dissolution rates in low/high DOC waters. The lower

bound is most realistic for particles sinking out of surface waters and should be used for modeling water column calcite dissolution rates. It may be fit by $R_{(mol\ cm\text{-}2\ s\text{-}1)} = 10^{-14.3\pm0.2}(1-\Omega)^{0.11\pm0.1}$ for $0.8 < \Omega < 1$, and $R_{(mol\ cm\text{-}2\ s\text{-}1)} = 10^{-10.8\pm0.4}\ (1-\Omega)^{4.7\pm0.7}$ for $0 < \Omega < 0.8$.

Chapter 3

A NEAR-EQUILIBRIUM COUPLED MECHANISTIC MODEL FOR CALCITE DISSOLUTION IN SEAWATER WITH 0, 14, AND 28 MILLIMOLAR TOTAL SULFATE

3.1 Introduction

Calcite dissolution kinetics have historically been fit using the empirical equation:

$$R = k(1 - \Omega)^n \quad (3.1)$$

Here, k is the rate constant (mol cm^{-2} s^{-1}), $\Omega = \frac{[Ca^{2+}][CO_3^{2-}]}{K'_{sp}}$ such that 1-Ω is a measure of the thermodynamic driving force of the solution, and n is a reaction order that varies from ~1 in low ionic strength water (Arakaki and Mucci, 1995; Boudreau, 2013; Cubillas et al., 2005; Sulpis et al., 2017; Svensson and Dreybrodt, 1992), to ~3-4.5 in seawater (Dong et al., 2018; Keir, 1980; Morse, 1978; Morse and Berner, 1972; Naviaux et al., 2019b, 2019a; Subhas et al., 2015, 2017; Walter and Morse, 1985). The simplicity of Eq. 1 has led to its widespread use in the mineral dissolution community, but this simplicity comes at the cost of mechanistic interpretability.

Calcite dissolution kinetics may be broadly broken down into four interrelated pieces: 1) the thermodynamic driving force of the solution (Ω), 2) the chemical speciation of the solution, 3) the chemical speciation of the mineral surface, and 4) the active surface dissolution mechanism (i.e. whether dissolution is dominated by the retreat of pre-existing steps, the formation of etch pits at defects, or the formation of etch pits homogenously across the mineral surface). We distinguish between each aspect in our discussion, but their effects on the overall dissolution rate are intertwined. As an example, changing the solution composition may alter the dissolution rate through changes in Ω, through changes in the mineral surface speciation, or through both simultaneously. Ultimately, the goal is to create

a unified theory of mineral dissolution that captures the complex relationships between each of the above mechanistic pieces.

Studies of calcite dissolution in low ionic strength water have made the most progress towards a unified mechanistic theory. Early research identified three rate-controlling chemical reactions in solution, that when combined, recreated the linear (n = 1 in Eq. 3.1) relationship of calcite dissolution rate versus Ω in freshwater (Busenberg and Plummer, 1986; Chou et al., 1989; Plummer et al., 1979a, 1978):

$$\mathrm{CaCO_{3(s)}} + \mathrm{H^+} \rightarrow Ca^{2+} + \mathrm{HCO_3^-} \quad (3.2a)$$

$$\mathrm{CaCO_{3(s)}} + \mathrm{H_2CO_3} \rightarrow Ca^{2+} + 2\mathrm{HCO_3^-} \quad (3.2b)$$

$$\mathrm{CaCO_{3(s)}} + \mathrm{H_2O} \rightleftharpoons Ca^{2+} + CO_3^{2-} + \mathrm{H_2O} \quad (3.2c)$$

In acidic conditions (pH <5), calcite dissolution exhibits a first order dependence on the activity of hydrogen ion in solution (Eq. 3.2a). H_2CO_3 is a neutral molecule that may also act as a proton donor and whose contribution to the overall rate becomes important in more basic conditions and at higher pCO_2 levels (Eq. 3.2b). Water catalyzed dissolution is thought to be constant and independent of solution chemistry, as the activity of the solid is assumed to be one (Eq. 3.2c).

In addition to pure solution chemistry, another avenue of research focused on understanding calcite dissolution in terms of reactive sites (Berner and Morse, 1974) and complexes on the mineral surface (Amrhein et al., 1985; Sjöberg and Rickard, 1984b). X-ray photoelectron spectroscopy provided direct evidence of a hydrated layer at the calcite surface (Stipp and Hochella, 1991), and adsorbed OH^-, HCO_3^-, Ca^{2+}, and CO_3^{2-} were identified as important precursors controlling the rate of dissolution near equilibrium (Busenberg and Plummer, 1986). With these results in mind, Van Cappellen et al. (1993) developed a constant capacitance model (CCM) of calcite surface complexation. In this model, dissolved cations/anions in solution adsorb at the mineral-solution interface (the “0-plane”) by

exchanging H^+/OH^- at hydroxylated cation sites (>Ca-OH^0) or protonated anion sites (>CO_3-H^0). Note that "*>i*" represents an ion associated with the mineral lattice. A key assumption in the Van Cappellen model is that formation of surface complexes is fast, and their detachment sets the dissolution rate. The model recreated observed trends in calcite surface charge versus pH and was able to correlate calcite dissolution rates at $\Omega = 0$ with densities of surface species.

In one of the most influential papers in the field, Arakaki and Mucci (1995) coupled the Van Cappellen et al. CCM with Eq.'s 3.2a-c to suggest the following reactions between surface complexes and ions in solution:

$$> CO_3^- + 2H^+ \underset{k_5}{\overset{k_1}{\rightleftarrows}} > Ca^+ + H_2CO_3 \tag{3.3a}$$

$$> Ca^+ + H_2CO_3 \underset{k_6}{\overset{k_2}{\rightleftarrows}} > CO_3H + CaHCO_3^+ \tag{3.3b}$$

$$> CO_3H + CaHCO_3^+ \underset{k_7}{\overset{k_3}{\rightleftarrows}} > Ca^+ + H_2CO_3 + CaCO_3^0 \tag{3.3c}$$

$$CaCO_{3(Solid)} \underset{k_8}{\overset{k_4}{\rightleftarrows}} CaCO_3^0 \tag{3.3d}$$

which could be combined into the complete rate equation:

$$\text{Rate} = k_1 > CO_3^-\{H^+\}^2 + (k_2 - k_5) > Ca^+\{H_2CO_3^*\} + k_4 - (k_6 - k_3) > CO_3H\{CaHCO_3^+\} - k_7 > Ca^+\{H_2CO_3^*\}\{CaCO_3^0\} - k_8\{CaCO_3^0\} \tag{3.4}$$

Here, > *i* is the density of surface complex *i* (mol m^{-2}), $\{i\}$ is the activity of dissolved species *i*, and k_i is the rate constant for reaction *i* in Eq.'s 3.3a-d.

By including the activities of ions in solution alongside the densities of surface complexes, the Arakaki and Mucci model, hereafter referred to as the A&M model, successfully fit freshwater calcite dissolution rates from $0.8 > \Omega > 0$ over a wide range of pCO_2 and pH. The A&M model also reproduced far-from-equilibrium rate behavior observed in bulk dissolution studies. In acidic (pH < 5) conditions, Eq. 3.4 reduces to a linear rate versus H^+ relationship as all $>CO_3^-$ are protonated to $>CO_3H$ and the k_1 term dominates. In more alkaline conditions, Eq. 3.4 is linear versus Ω. Another convincing aspect of the model is that the fitted values of $\frac{k_4}{k_8\{CaCO_3^0\}}$ provide an excellent estimate of calcite K_{sp} in freshwater.

The A&M model was able to describe dissolution rates without accounting for variations in surface dissolution mechanism, but this success may have been a function of the data used to validate the model. The existence of different surface mechanisms was well known at the time of A&M (Burton et al., 1951; Burton and Cabrera, 1949; Cabrera and Levine, 1956; Lasaga and Blum, 1986; MacInnis and Brantley, 1992; Schott et al., 1989; Zhang and Nancollas, 1990), but it was not until Teng (2004) that the "critical Ωs" ($\Omega_{critical}$s) for activating each mechanism were well constrained. Teng found that calcite dissolution in low ionic strength water proceeded by the retreat of pre-existing steps for $1 > \Omega > 0.54$, 2D etch pit formation at defects for $0.54 > \Omega > 0.007$, and finally homogenous 2D etch pit formation for $0.007 > \Omega$. A&M validated their model on dissolution rates between $0.8 > \Omega > 0$ from Plummer et al. (1978), and A&M state that they recreate the linear rate behavior versus 1-Ω. However, it is unclear from the figures in A&M how well the model actually fits the raw data on the extreme ends of the Ω range. The original data in Plummer et al. (1978) does not include Ω calculations, so we instead plot in Figure 3.1 the data from another paper by the same authors using the same pH stat method (Busenberg and Plummer, 1986). It is clear from this raw data that the linear behavior does not extend for the entire Ω range. All dissolution rates begin to fall off the linear trend around $\Omega > 0.5$, where calcite transitions from defect-assisted etch pit formation to pure step-retreat. There is also a large increase in the dissolution rate near $1\text{-}\Omega \sim 1$ that is likely due to the activation of homogenous etch pit formation. We therefore hypothesize that the fitted rate constants in the A&M were derived

primarily from calcite dissolving via a single surface mechanism, defect-assisted etch pit formation.

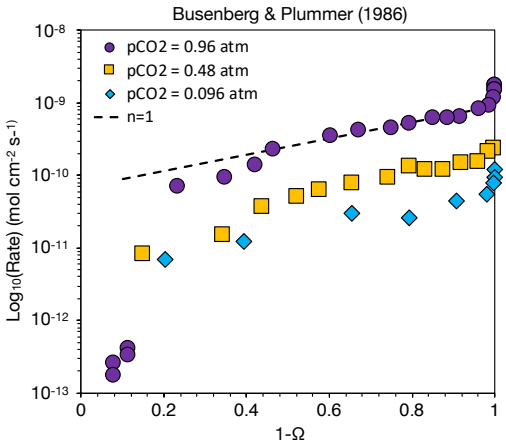

Figure 3.1: Data transcribed from Table 10 of Busenberg and Plummer (1986) on calcite dissolution rates (mol cm^{-2} s^{-1}) versus 1-Ω in $Ca(HCO_3)_2$ solutions at different pCO_2 levels. The n = 1 line is a fit to Rate = k(1-Ω) using a k of $9 \cdot 10^{-10}$ mol cm^{-2} s^{-1}.

A mechanistic understanding of calcite dissolution in seawater has progressed more slowly than it has in freshwater, but several recent advances have helped to close the gap. Naviaux et al. (2019b) measured the near-equilibrium temperature dependence of calcite dissolution rates and demonstrated that the $\Omega_{critical}$s in seawater occurred much closer to equilibrium than they did in freshwater. Naviaux et al also provided the first estimates in seawater of the step kinetic coefficient (β), density of active nucleation sites (n_s), step edge free energy (α), activation energy of detachment from kinks/steps (ϵ_{step}), and activation energy of etch pit initiation (ϵ_{init}). Though β, n_s, ϵ_{step}, and ϵ_{init} had similar values to those reported in freshwater, the temperature dependence of α reversed sign depending upon which surface dissolution mechanism was active, suggesting a complete theory of calcite dissolution kinetics would require knowledge of the chemical speciation of the solution and/or mineral surface.

The solution speciation of seawater is notoriously complex, but recent advances have allowed for changes in speciation resulting from different major ion compositions to be

calculated (Hain et al., 2015). Historically, seawater speciation has been calculated using either a "bottom up" or "top down" approach. In the bottom up approach, thermodynamic parameters from freshwater experiments are adjusted to the desired conditions using ionic strength and interaction corrections (Millero and Pierrot, 1998; Millero and Schreiber, 1982; Pitzer, 1973). This strategy is used by the U.S Geological Survey modeling software, PHREEQC (Parkhurst, 1995), and has the advantage that it can be applied to solutions of varying compositions. However, the bottom up approach is more accurate in low to mid ionic strength conditions than in seawater (Hain et al., 2015). The top down approach used by programs such as CO2SYS (van Heuven et al., 2011) only considers the empirically determined values for association constants in seawater. CO2SYS provides the best estimates for modern seawater chemistries, but cannot be applied to alternative compositions that may have existed in the past. The MyAMI model released by Hain et al., (2015) combines the strength of each approach by using the Pitzer equations (Pitzer, 1973) to calculate changes in seawater association constants *relative* to empirically determined values:

$$\mathrm{pK}^*_{\mathrm{predicted}}|_{(\mathrm{T,S,X})} = \mathrm{pK}^*_{\mathrm{empirical}}(\mathrm{T,S})|_{\mathrm{X}_0} + \Delta\mathrm{pK}^*_{\mathrm{MyAMI}}|_{(\mathrm{T,S,X})} \quad (3.5a)$$

$$\Delta\mathrm{pK}^*_{\mathrm{MyAMI}}|_{(\mathrm{T,S,X})} = \mathrm{pK}^*_{\mathrm{MyAMI}}(\mathrm{T,S,X}) - \mathrm{pK}^*_{\mathrm{MyAMI}}(\mathrm{T,S,X}_0) \quad (3.5b)$$

Here, pK^* is the negative logarithm of the association constant, K^*. The "*" signifies that the constant is empirical and conditional on the temperature (T), salinity (S), and chemical composition (X) of the solution. X_0 is modern seawater composition.

Surface complexation models are widespread for calcite in low ionic strength water (Heberling et al., 2011; Oleg S. Pokrovsky et al., 2009; Pokrovsky, 1998b; Pokrovsky et al., 2005; Pokrovsky and Schott, 2002; Wolthers et al., 2012b, 2008), and generally come in two forms, simple CCMs such as the one in Van Cappellen et al. (1993), and more complex Stern models (SMs). In a CCM, all potential determining ions (PDIs) may coordinate with the 0-plane hydrolysis layer at the mineral surface. CCMs can account for a wide range of dissolution/precipitation rate behaviors (Schott et al., 2009), but they tend to overestimate the mineral surface capacitance (Heberling et al., 2011) and the effect of pH (Al Mahrouqi

et al., 2017). SMs provide a more realistic estimate of surface capacitance than CCMs, but they do so at the cost of model complexity. In addition to the surface hydrolysis layer, SMs explicitly model the inner (1-plane) and outer (2-plane) Helmholtz planes. Both SMs and CCMs are validated using surface potential measurements. However, the differences in sophistication between SMs and CCMs mean that the surface complexes proposed by each model differ greatly. SMs and CCMs have recently been extended to seawater solutions (Ding and Rahman, 2018; Song et al., 2019, 2017), but they have yet to be coupled with dissolution/precipitation rate data.

The goal of this paper is to combine the latest solution and surface chemistry models to test if the reactions proposed by A&M can also describe calcite dissolution rates in seawater. We achieve this by fitting Eq. 3.4 to the dissolution data from Naviaux et al. (2019b), as well as to novel dissolution rate measurements made in artificial seawater of varying total sulfate (SO_{4T}) concentrations. The sulfate experiments serve dual purposes: 1) Marine sulfate levels have varied between 0.1 and 28 mM over the last 3.5 billion years (Canfield and Farquhar, 2009; Fakhraee et al., 2019; Luo et al., 2010). Some work has shown that sulfate inhibits calcite dissolution rates far from equilibrium (Sjöberg, 1978), these results are not applicable to ocean saturations which are typically much closer to equilibrium. Given the changes in surface dissolution mechanism that occur near equilibrium (Naviaux et al., 2019b; Subhas et al., 2017), it is important to evaluate the effects of sulfate across the full range of Ω. 2) The sulfate data provides additional constraints on the A&M model fit, thereby allowing for a more robust test of the model.

3.2 Experimental Methods

Dissolution rate measurements were made by dissolving pure ^{13}C inorganic calcite in solutions of varying compositions according to previous methods (Dong et al., 2019, 2018; Naviaux et al., 2019a, 2019b; Subhas et al., 2015, 2017). All rate data for this manuscript were collected using ^{13}C-calcite that had been wet sieved to a size fraction of 20-53 μm, the specific surface area of which was established using Kr gas BET to be 0.152 ± 0.006 $m^2\ g^{-1}$ (Naviaux et al., 2019a, 2019b). Experiments were conducted in either Dickson Seawater

Reference Material (Dickson, 2010) or in phosphate free, "Aquil," artificial seawater (Morel et al., 1979) with varying concentrations of sulfate (Table 3.1) The ionic strengths of the Aquil solutions were held constant by compensating changes in sulfate with KCl. KCl was used because its components do not directly interact with the carbonic acid system species. Solution saturation states were calculated using pairs of alkalinity (Alk) and dissolved inorganic carbon (DIC) measurements as input parameters in either CO2SYS v1.1 (van Heuven et al., 2011), or a modified version of CO2SYS discussed below. Dickson seawater Ω was calculated with the carbonic acid system K_1' and K_2' dissociation constants from the Lueker et al. (2000) refit to Mehrbach et al.'s (1973) data, calcite K_{sp}' from Mucci (1983), K_{HSO4} from Dickson (1990a), and K_{boron} from Dickson (1990). The total boron-salinity ratio was taken from Lee et al., (2010). The standard errors in DIC (± 2-4 μmol kg^{-1}) and alkalinity (± 1-3 μmol kg^{-1}) were propagated using a Monte Carlo approach (Subhas et al., 2015), yielding final errors on Ω of 0.01-0.04 units.

Table 3.1: Composition of "Aquil" Artificial Seawater

	Composition (mol kg^{-1})		
Compound	Full Seawater	14 mM SO_{4T}	0 mM SO_{4T}
NaCl	$4.0976 \cdot 10^{-1}$	$4.0976 \cdot 10^{-1}$	$4.0976 \cdot 10^{-1}$
$CaCl_2 \cdot 2H_2O$	$1.029 \cdot 10^{-2}$	$1.029 \cdot 10^{-2}$	$1.029 \cdot 10^{-2}$
KBr	$8.2 \cdot 10^{-4}$	$8.2 \cdot 10^{-4}$	$8.2 \cdot 10^{-4}$
NaF	$7 \cdot 10^{-5}$	$7 \cdot 10^{-5}$	$7 \cdot 10^{-5}$
KCl	$9.160 \cdot 10^{-3}$	$2.316 \cdot 10^{-2}$	$3.716 \cdot 10^{-2}$
H_3BO_3	$4.73 \cdot 10^{-4}$	$4.73 \cdot 10^{-4}$	$4.73 \cdot 10^{-4}$
Na_2SO_4	$2.81 \cdot 10^{-2}$	$1.40 \cdot 10^{-2}$	0
$NaHCO_3$	$2.32 \cdot 10^{-2}$	$2.32 \cdot 10^{-2}$	$2.32 \cdot 10^{-2}$
$SrCl_2 \cdot 6H_2O$	$6.2 \cdot 10^{-5}$	$6.2 \cdot 10^{-5}$	$6.2 \cdot 10^{-5}$
$MgCl_2 \cdot 6H_2O$	$5.288 \cdot 10^{-2}$	$5.288 \cdot 10^{-2}$	$5.288 \cdot 10^{-2}$

3.3 Background and Modification of MyAMI Code

We briefly discuss the origin of the seawater speciation calculations our model is based upon, before discussing the modifications that we made. The original MIAMI model (Millero and

Pierrot, 1998) utilizes the Pitzer equations (Pitzer, 1973) to calculate the activity coefficients and equilibrium constants for seawater of arbitrary composition. In their "MyAMI" model, Hain et al. (2015) modified MIAMI to: 1) Use a truncated version of the general Pitzer equation ignoring higher order electrostatic terms. 2) Only consider the interactions of a subset of chemical species (Na^+, Cl^-, Mg^{2+}, SO_4^{2-}, HSO_4^-, Ca^{2+}, Sr^{2+}, K^+, $MgOH^+$, $B(OH)_4^-$, H_3BO_3, H_2CO_3, HCO_3^-, CO_3^{2-}, H^+, OH^-) deemed most relevant to the carbonic acid system equilibrium constants. 3) Calculate the change in equilibrium constants relative to empirically determined values, rather than deriving the equilibrium from activity calculations. Note that empirical equilibrium constants for the carbonic acid system are defined using "Total" concentrations of each species, where:

$$[HCO_3^-]_{Total} = [NaHCO_3] + [MgHCO_3^+] + [CaHCO_3^+] + [SrHCO_3^+] \quad (3.6a)$$

$$[CO_3^{2-}]_{Total} = [NaCO_3^-] + [MgCO_3] + [CaCO_3] + [SrCO_3] \quad (3.6b)$$

4) Derive equilibrium constants on the total pH (pH_T) scale, where $pH_T = -\log_{10}([H^+]_T) = -\log_{10}([H^+]_{Free} + [HSO_4^-])$. 5) Run more efficiently using a least square optimization algorithm to fit the equilibrium constants.

The MyAMI code takes as inputs temperature (T), salinity (S), and seawater composition (X). Concentrations of calcium ($[Ca^{2+}]$) and magnesium ($[Mg^{2+}]$) may be varied by the user, whereas total sodium, potassium, strontium, chloride, boron, and sulfate are assumed to vary with salinity according to the ratios in Table 4 of Millero et al. (2008). For a given T, S, $[Ca^{2+}]$, and $[Mg^{2+}]$, MyAMI outputs the change in the empirical equilibrium constants, ΔpK^*_{MyAMI}, such that the predicted equilibrium constant is given by Eq. 3.5a.

We further modified the MyAMI code for the analysis in this manuscript. We refer to this modified code as "Mod-MyAMI". The first modification, as recommended by Hain et al., (2016), was to update the Pitzer-model calcium-bicarbonate coefficients from those in Table 1 of Harvie et al. (1984), to those in Table 5 of He and Morse (1993). The second

modification was to remove the salinity dependence of [SO_{4T}] so that its concentration could be explicitly varied by the user. All code is available at https://github.com/jnaviaux/Sulfur_PyMyAMI.

Empirical equilibrium constants were calculated for seawater of modern composition, as well as for seawater with SO_{4T} = 14 mM, and SO_{4T} = 0 mM. The resulting values are in Table 3.2. These updated pK values were input into CO2SYS alongside Alk-DIC pairs to calculate Ω in Aquil seawater.

Table 3.2: Outputs from Mod-MyAMI Code. pK^* values are on the pH_T scale. γ^T and γ^F represents the "total" and "free" ion activity coefficients, respectively

Equilibrium Constant	$pK^*\|_{(28\ mM\ SO_{4T})}$	$pK^*\|_{(14\ mM\ SO_{4T})}$	$pK^*\|_{(0\ mM\ SO_{4T})}$
$K_w^* = [H^+]_T[OH^-]_T = K_w \frac{1}{\gamma_H^T \gamma_{OH}^T}$	13.217	13.274	13.337
$K_0^* = \frac{[H_2CO_3^*]}{CO_2} = K_0 \frac{\gamma_{CO_2}^F}{\gamma_{H_2CO_3}^F}$	1.547	1.545	1.543
$K_1^* = \frac{[H^+]_T[HCO_3^-]_T}{[H_2CO_3^*]} = K_1 \frac{\gamma_{H_2CO_3}^F}{\gamma_H^T \gamma_{HCO_3}^F}$	5.847	5.899	5.957
$K_2^* = \frac{[H^+]_T[CO_3^{2-}]_T}{[HCO_3^-]_T} = K_2 \frac{\gamma_{HCO_3}^F}{\gamma_H^T \gamma_{CO_3}^F}$	8.966	9.022	9.085
$K_{HSO4}^* = \frac{[H^+]_T[SO_4^{2-}]}{[HSO_4^-]} = K_{HSO_4} \frac{\gamma_{HSO_4}^F}{\gamma_H^T \gamma_{SO_4}^F}$	0.999	1.050	1.107[A]
$K_B^* = \frac{[H^+]_T[B(OH)_4^-]}{[H_3BO_3]} = K_B \frac{\gamma_{H_3BO_3}^F}{\gamma_H^T \gamma_{B(OH)_4}^F}$	8.598	8.648	8.705
$K_{spA}^* = \frac{[CO_3^{2-}]_T[Ca^{2+}]}{\Omega_{aragonite}} = K_{spA} \frac{1}{\gamma_{CO_3}^T \gamma_{Ca}^F}$	6.188	6.193	6.198
$K_{spC}^* = \frac{[CO_3^{2-}]_T[Ca^{2+}]}{\Omega_{calcite}} = K_{spC} \frac{1}{\gamma_{CO_3}^T \gamma_{Ca}^F}$	6.369	6.374	6.379

[A] Although this value was calculated, it was not necessary for the 0mM SO_{4T} experiments

3.4 Implementation into PHREEQC

3.4.1 Comparison with CO2SYS

PHREEQC is often used for speciation calculations, but it performs poorly when applied to seawater-like compositions (Hain et al., 2015). To demonstrate this, we compare the carbon

chemistry outputs from PHREEQC and CO2SYS in Figure 3.2. When using the default PHREEQC database, the equilibrium between $H_2CO_3^*$ and $HCO_3^-{}_T$ is offset by ~0.05 log units compared to its empirically determined value in seawater, and the equilibrium between $HCO_3^-{}_T$ and $CO_3^{2-}{}_T$ is offset by ~0.1 units.

Although sufficient for general use, this difference in carbonate speciation has a profound effect on the calculated calcite saturation state (Figure 3.2b,c). The Ω calculated by CO2SYS (Ω_{CO2SYS}) was used as a benchmark with which to compare the Ω calculated by PHREEQC ($\Omega_{PHREEQC}$). In both cases, DIC was set to 2 mM, and the solution saturation state was varied by changing pH_T. Under conditions where $\Omega_{CO2SYS} = 1$, the default PHREEQC database greatly underestimates the solution saturation and calculates $\Omega_{PHREEQC} = 0.68$. Updating the PHREEQC database to use the empirical seawater $pK_{spC}^* = 6.369$ (Mucci, 1983b) improves the discrepancy, but the offset between $\Omega_{PHREEQC}$ and Ω_{CO2SYS} still reaches 0.16 units when $\Omega_{CO2SYS} = 1$ (Figure 3.2c). Seawater calcite dissolution experiences two surface mechanism changes within ~0.2 Ω units (Naviaux et al., 2019b), so the PHREEQC database require further modification before its results can be coupled with experimental dissolution rates.

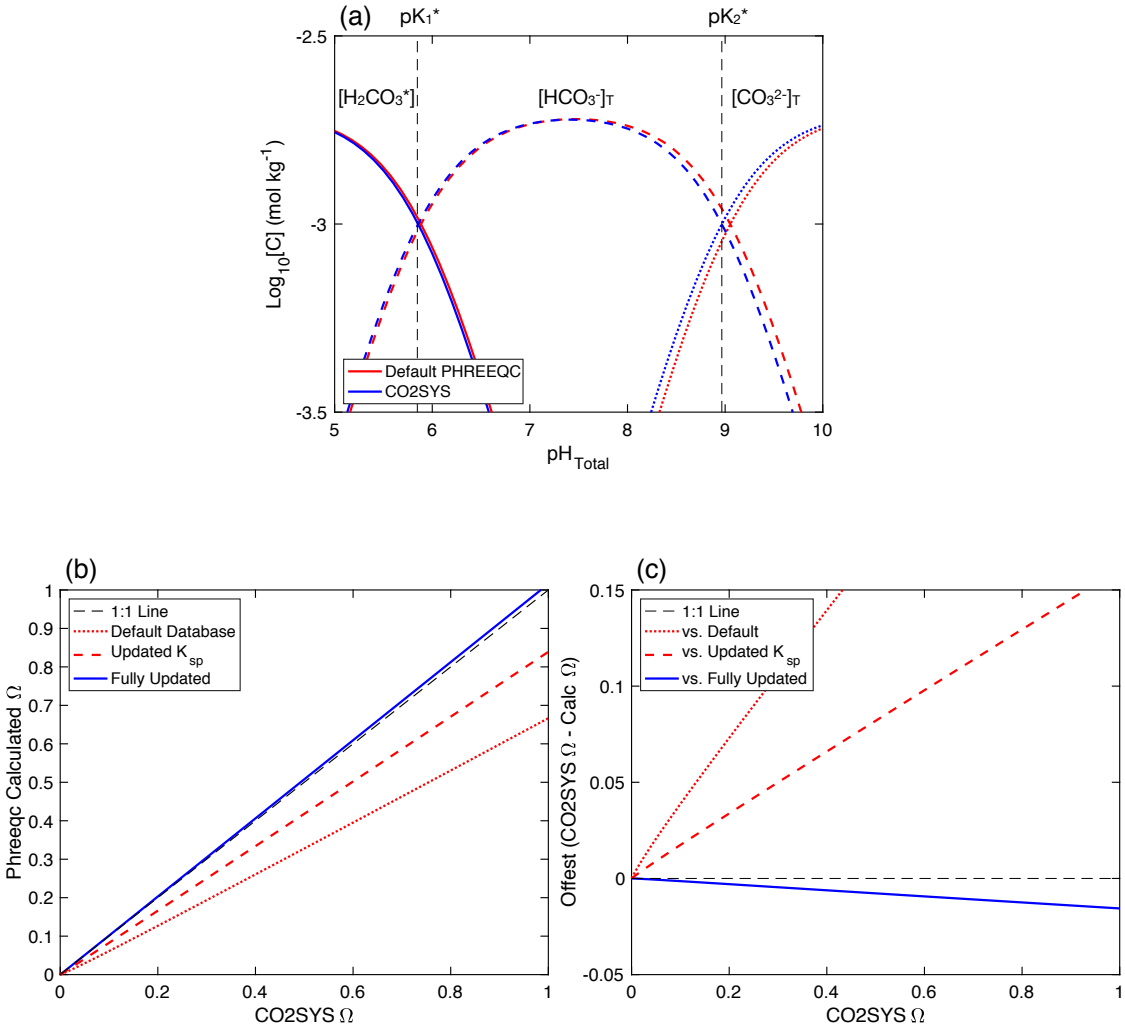

Figure 3.2: (a) Log_{10}Concentration versus pH_T in seawater at T=25°C, S=35, total DIC = 2 mM, for $[H_2CO_3^*]$, $[HCO_3^-]_T$, and $[CO_3^{2-}]_T$ calculated using the default PHREEQC database (red), and an updated database using the constants in Table 3.2 (blue). Empirical seawater pK^* values are included for reference. The equilibrium between each species is offset towards higher pH values when computed by the default PHREEQC database. (b) Ω_{CO2SYS} versus $\Omega_{PHREEQC}$ calculated by different iterations of PHREEQC databases for DIC = 2 mM and varying pH_T. See text for details. (c) The offset between Ω calculations versus Ω_{CO2SYS}. Even with updated K_{sp}^*, the default PHREEQC database is over 0.15 Ω units offset from Ω_{CO2SYS}. The fully updated PHREEQC database agrees within 0.02 Ω units from $0 < \Omega < 1$.

Final agreement between Ω calculations was achieved by removing the individual carbon system ion pairing reactions (components in Eq. 3.6a, b) from the PHREEQC database and

calculating $HCO_3^{-}{}_T$ and $CO_3^{2-}{}_T$ using the empirical pK values in Table 3.2. Once the Ω calculation from PHREEQC agreed with that from CO2SYS, we could then use PHREEQC to calculate the surface and chemical speciation for each of our experimental measurements. Note that the pKs in Table 3.2 are based upon concentrations, so the updated PHREEQC database now calculates concentrations of solution species, rather than activities. The updated database also no longer calculates the $CaHCO_3^+$ and $CaCO_3^0$ ion pairs, both of which are important in the A&M model. We can circumvent this limitation by applying the ratio of $CaHCO_3^+/HCO_3^{-}{}_T$ and $CaCO_3^0/CO_3^{2-}{}_T$ calculated by the default PHREEQC database to our final output. In seawater over the full Ω range, the default PHREEQC database calculates that $CaHCO_3^+$ will be 2.2% of $HCO_3^{-}{}_T$, and $CaCO_3^0$ will be 12.4% of $CO_3^{2-}{}_T$. These ratios will be carried forward in our fitting of the A&M equations, but we recognize that this is an area of future model improvement.

3.4.2 Choice of Surface Speciation Model

Three different surface speciation models were evaluated: a CCM by Song et al. (2019, 2017), a CCM by Ding and Rahman (2018), and a SM by Ding and Rahman adapted from Heberling et al. (2011). Though each model was validated against calcite surface potential measurements in seawater, they envision very different speciations taking place at the mineral surface. We chose to proceed using the CCM from Ding and Rahman, as it was most similar to the Van Cappellen et al. model used by A&M (Table 3.3). Future work will need to test alternative rate equations against the other surface complexation models.

Table 3.3: Comparison of surface binding constants among complexation models			
	$Log_{10}K$ (25°C, 1 atm)		
Surface Binding Reaction	Van Cappellen et al. (1993) I = 0	Pokrovsky and Schott (2002) I = 0	Ding and Rahman (2018) 0.06 < I < 1.1
$> CaOH + H^+ \rightleftarrows > CaOH_2^+$	12.2	11.85	11.8
$> CaOH + CO_3^{2-} + 2H^+ \rightleftarrows > CaHCO_3^0 + H_2O$	24.15	23.50	N/A
$> CaOH_2^+ + SO_4^{2-} \rightleftarrows > CaSO_4^- + H_2O$	N/A	N/A	-2.10
$> CaOH_2^+ + CO_3^{2-} \rightleftarrows > CaCO_3^- + H_2O$	3.35	5.25	6.00
$> CO_3H \rightleftarrows > CO_3^- + H^+$	-4.9	-5.1	-5.1
$> CO_3^- + Ca^{2+} \rightleftarrows > CO_3Ca^+$	2.1	3.4	2.85
$> CO_3^- + Mg^{2+} \rightleftarrows > CO_3Mg^+$	N/A	N/A	0.68

3.5 Results and Discussion

3.5.1 Dissolution Experiments with Variable [SO_{4T}]

Experimentally measured calcite dissolution rates are plotted versus pH_T in Figure **3.3**a, and 1-Ω in Figure **3.3**b,c. In agreement with previous studies (Sjöberg, 1978), removing sulfate increases calcite dissolution rates far-from-equilibrium, with rates being ~2x faster in 0 mM S_T Aquil than in 28 mM S_T seawater. Decreasing SO_{4T} increases dissolution rates for pH_T < 7.2, but pH is a poor metric for differentiating rates near equilibrium, so the effects are not as obvious for pH_T > 7.2. When plotted versus 1-Ω, it is clear that the effects of changing SO_{4T} depend strongly on the distance from equilibrium (Fig. 3.2c,d). Dissolution rates are fastest in low SO_{4T} Aquil far-from-equilibrium, but the differences between each of the three media decrease from $Log_{10}(1-\Omega)$ = 0 to -0.3 (Ω = 0 to 0.5). As the saturation continues to increase, dissolution rates in low SO_{4T} Aquil surpass rates in 28 mM SO_{4T} Aquil. The decrease in dissolution rates does not appear to scale directly with the change in SO_{4T}. At $Log_{10}(1-\Omega)$ = -0.82 (Ω = 0.85), dissolution rates in 14 mM SO_{4T} Aquil are ~3-4x slower than in full seawater, but rates in 0 mM SO_{4T} Aquil are over 20x slower.

Changing [SO_{4T}] may also affect the $\Omega_{critical}$s for transitions between surface dissolution mechanisms, but more data will be required to know this with certainty. Dissolution rates in

full seawater form two straight lines in Log-Log space, with a change in slope at $Log_{10}(1-\Omega) = -0.6$ ($\Omega = 0.75$). Once this critical undersaturation is surpassed, etch pits are no longer limited to formation at defects, and instead begin opening homogenously across the calcite surface (Naviaux et al., 2019b). Similarly to full seawater, the slope of rate versus Ω for 14 mM SO_{4T} Aquil appears linear from $-1.25 < Log_{10}(1-\Omega) < -0.6$, suggesting that dissolution in this media also proceeds by defect-assisted etch pit formation. The difference between the magnitude of the slope in 28 mM and 14 mM SO_{4T} from $-1.25 < Log_{10}(1-\Omega) < -0.6$ suggests that decreasing SO_{4T} lead to an increase in the calcite surface step edge free energy (Naviaux et al., 2019b). Dissolution rates in 14 mM SO_{4T} Aquil also follow a relatively linear dependence with Ω farther from equilibrium, though there may be additional curvature near the rate crossover point at $Log_{10}(1-\Omega) = -0.3$.

Calcite dissolution rates in 0 mM SO_{4T} Aquil exhibit a similar kink in slope at $Log(1-\Omega) = -0.6$, but the behavior on either side of this Ω differs from the other solutions. The 0 mM SO_{4T} Aquil exhibits greater curvature across the full Ω range, such that it forms an "S" shaped pattern. The "S" shape is largely driven by two points; the near-equilibrium point at $Log_{10}(1-\Omega) = -1.22$ ($\Omega = 0.94$), and the rate crossover point at $Log_{10}(1-\Omega) = -0.3$. Due to signal drift of the Picarro CRDS, the point nearest equilibrium was within error of 0 dissolution rate. Even if this point is ignored, the rate behavior in sulfate free Aquil is still quite different than in full seawater. More data will be required to constrain the surface dissolution mechanism.

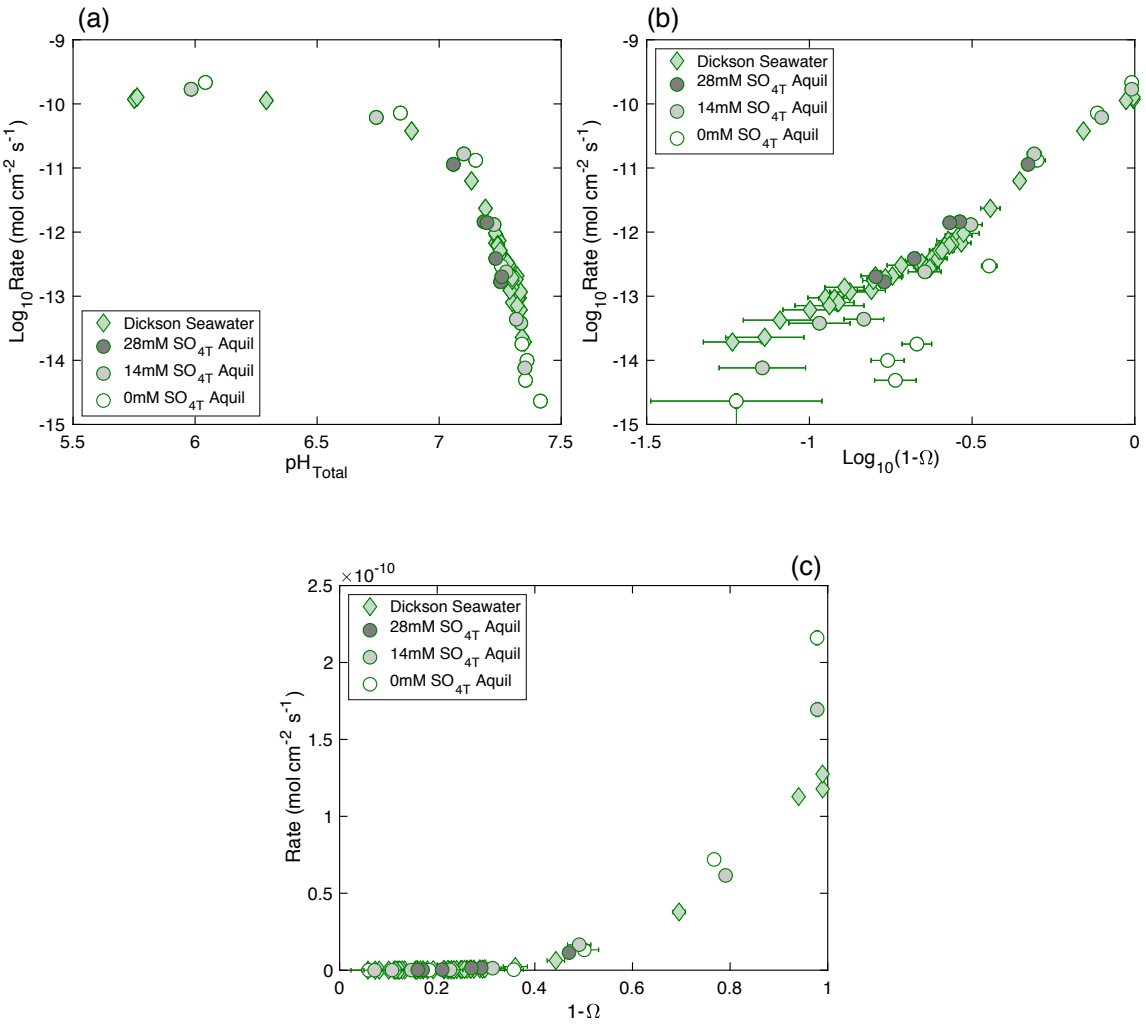

Figure 3.3: Dissolution rate (mol cm^{-2} s^{-1}) of inorganic calcite at 21°C in Dickson seawater (diamonds, 28 mM SO_{4T}, from Naviaux et al. 2019) and Aquil with 28 mM SO_{4T} (dark grey) 14 mM SO_{4T} (grey) or 0 mM SO_{4T} (open circles) plotted as (a) Log_{10}(Rate) vs. pH_T, (b) Log_{10}(Rate) vs. Log_{10}(1-Ω), (c) Rate vs. 1-Ω. Error bars are typically smaller than symbols. The 0 mM SO_{4T} point closest to equilibrium is within error of 0 dissolution rate.

3.5.2 Surface and Solution Speciation Calculations

The coupled PHREEQC speciation results for the bulk solution and calcite surface are plotted versus pH_T in Figure **3**.**4**a,b. Solution carbon speciation is plotted for each [SO_{4T}], but surface speciation is only plotted for 28 mM (solid lines) and 0 mM (dashed lines) SO_{4T} for visual clarity. We plot all surface species in the Ding and Rahman (2018) CCM, but focus our

discussion on $>CaOH_2^+$, $>CO_3^-$, and $>CO_3H$, as these species appear in Eq. 3.4. Similarly to freshwater, surface calcium and carbonate groups are dominated by $>CaOH_2^+$ and $>CO_3^-$ for $pH_T < 6$ (Figure **3.4**b). As the pH increases, $>CaOH_2^+$, $>CO_3^-$, and $>CO_3H$ are replaced by $>CaCO_3^-$ and $>CO_3Ca^+$ groups. The concentration of $>CO_3H$ decreases more rapidly than $>CaOH_2^+$ and $>CO_3^-$. Removing sulfate does change the distribution of surface species slightly, but the magnitude of the change is difficult to see given the nearly 7 order of magnitude spread in surface species concentrations. For the solution, removing sulfate shifts every pK^* towards higher values (Table 3.2), such that, at any given pH_T, there is more $[H_2CO_3^*]$, less $[HCO_3^-]_T$, and less $[CO_3^{2-}]_T$ (Figure **3.4**a).

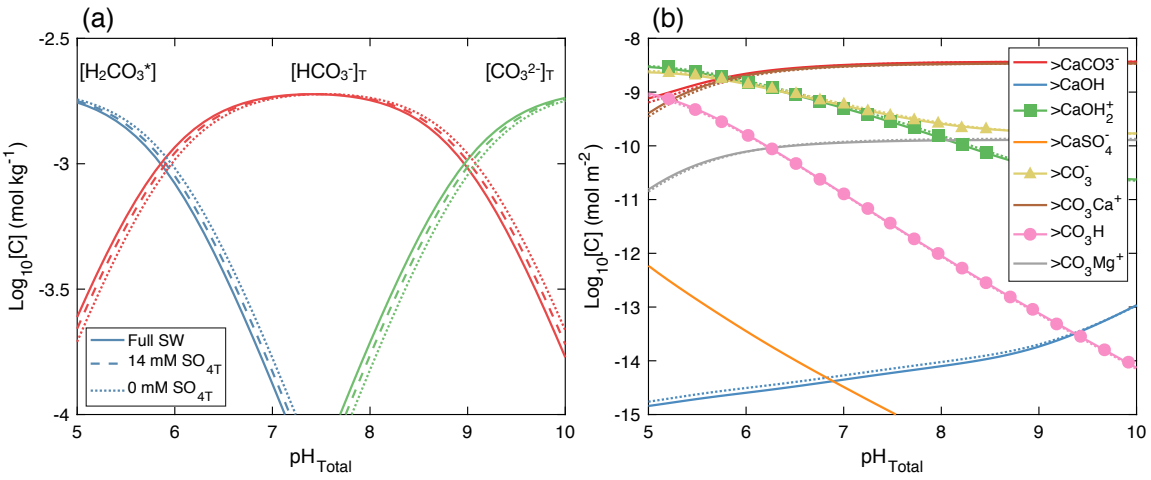

Figure 3.4: Log_{10}(Concentration) versus pH_T for (a) solution carbon speciation in 28 (solid lines), 14 (large dashes), and 0 mM (small dashes) SO_{4T} seawater and (b) mineral surface speciation in 28 (solid lines) and 0 mM SO_{4T} seawater. Symbols indicate surface species present in Eq. 3.4.

Removing sulfate necessarily affects pH_T by decreasing $[HSO_4^-]$, so changes in speciations are more informative when plotted versus Ω (Figure **3.5**a-c). Plotting versus Ω also facilitates comparisons with dissolution rate data near equilibrium. For the speciation of the surface, we see that complexes change by 1-2 orders of magnitude between $0 < \Omega < 0.1$, and then evolve more gradually as Ω approaches 1. Removing sulfate decreases $>CaOH_2^+$ and $>CO_3^-$ by ~3% and $>CO_3H$ by 26%, with the difference being nearly constant from $0.1 < \Omega < 1$

(Figure **3.5**c). For the solution speciation, normalizing by Ω reveals that carbon speciation is not affected by removing sulfate (Figure **3.5**a). However, the acidity of the solution, as measured by $[H^+]_T = [H^+]_F + [HSO_4^-]$, decreases by 22% when going from 28 to 0 mM SO_{4T} (Figure **3.5**b,c).

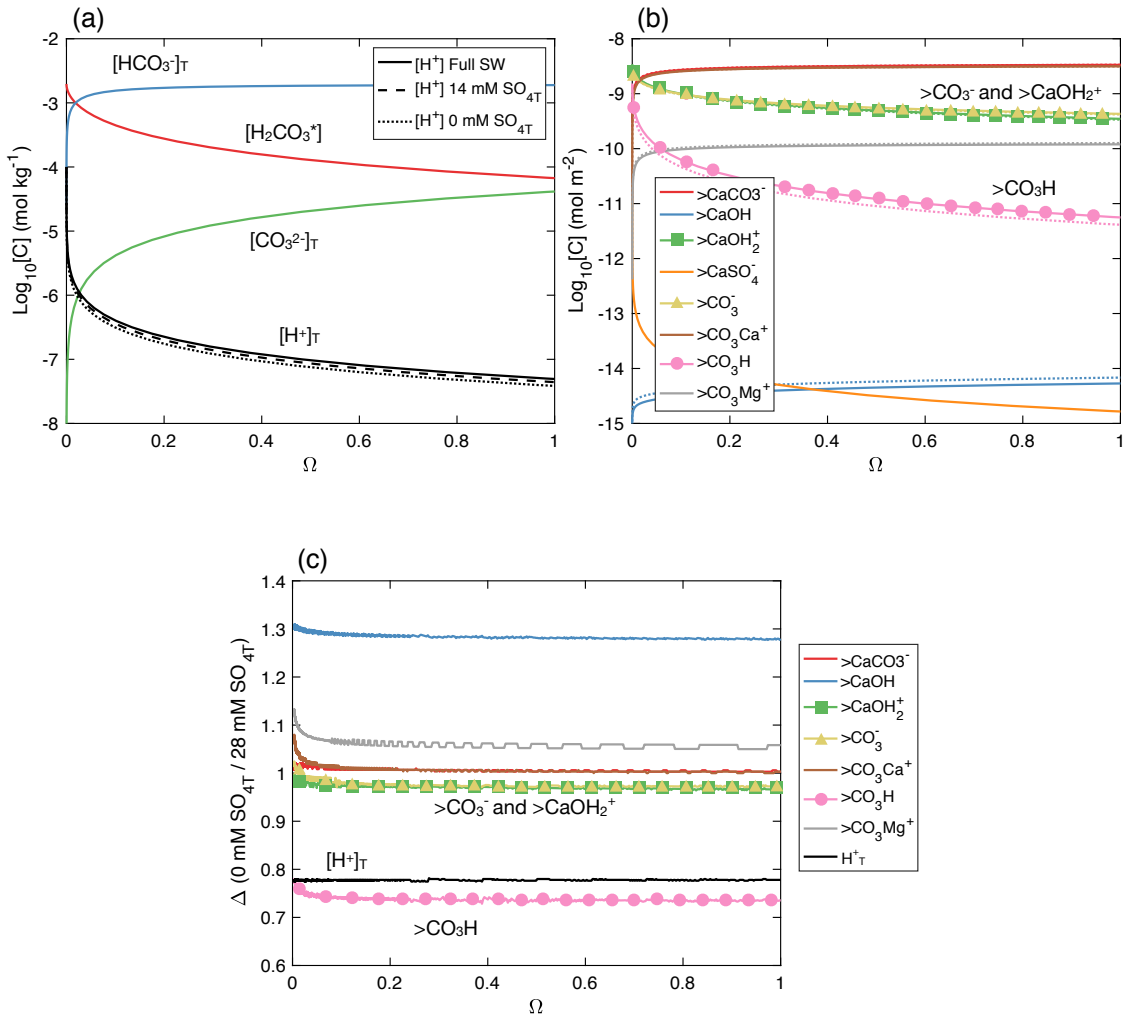

Figure 3.5: Log_{10}(Concentration) versus Ω for (a) solution carbon speciation in 28 (solid lines), 14 (large dashes), and 0 mM (small dashes) SO_{4T} seawater and (b) mineral surface speciation in 28 (solid lines) and 0 mM SO_{4T} seawater. (c) the relative difference between species concentrations in 0 mM and 28 mM SO_{4T} seawater versus Ω. Symbols indicate surface species present in Eq. 3.4.

3.5.3 Proposed Kinetic Model

The updated PHREEQC database was used to calculate $>CaOH_2^+$, $>CO_3^-$, $>CO_3H$, $[H_2CO_3^*]$, $[HCO_3^-]_T$, and $[CO_3^{2-}]_T$ at intervals of 0.001 Ω units from $0.01 < \Omega < 1$. Though not calculated explicitly, $[CaHCO_3^+]$ was taken to be 2.2% of $[HCO_3^-]_T$, and $[CaCO_3^0]$ was taken to be 12.4% of $[CO_3^{2-}]_T$ as discussed above. The calculated Ωs were used to match experimental dissolution rate data with the corresponding speciation calculations. The best fits to the rate constants in Eq. 3.4 were found using MATLAB's lsqnonlin least squares minimization function. Given initial estimates of rate constants, this function simultaneously minimized the difference between the measured and calculated dissolution rates in each solution. Dissolution rates corresponding with homogenous etch pit formation ($\Omega < 0.75$) could not be fit by Eq. 3.4, but the model successfully fit all data from $0.9 < \Omega < 0.75$ where dissolution in full SO_4 seawater occurs via defect-assisted etch pit formation. The success of this fit near equilibrium is impressive, as it indicates that the same chemical reactions set calcite dissolution rates in both freshwater and seawater for defect-assisted etch pit formation. The best fit parameters are in Table 3.4, and the predicted rates are plotted versus the experimental measurements in Figure 3.6.

Table 3.4: Best fit to rate constants in Eq. 3.4 when rate is expressed in mol cm^{-2} s^{-1} and surface species densities are in mol m^{-2}

Rate Constant	Units	This Study (Seawater, $0.75<\Omega<0.9$)	A&M (Freshwater)	Ratio (This Study / A&M)
k_1	s^{-1}	$6.17 \cdot 10^{8}$	$4.381 \cdot 10^{6}$	141
k_2-k_5	s^{-1}	$1.03 \cdot 10^{-7}$	42.52	$2.4 \cdot 10^{-9}$
k_4	mol cm^{-2} s^{-1}	$4.31 \cdot 10^{-12}$	$6.914 \cdot 10^{-11}$	$6.2 \cdot 10^{-2}$
k_6-k_3	s^{-1}	3.73	61.67	$6.0 \cdot 10^{-2}$
k_7	s^{-1}	$9.09 \cdot 10^{3}$	$2.332 \cdot 10^{5}$	$3.9 \cdot 10^{-4}$
k_8	mol cm^{-2} s^{-1}	$5.77 \cdot 10^{-8}$	$1.275 \cdot 10^{-5}$	$4.5 \cdot 10^{-3}$

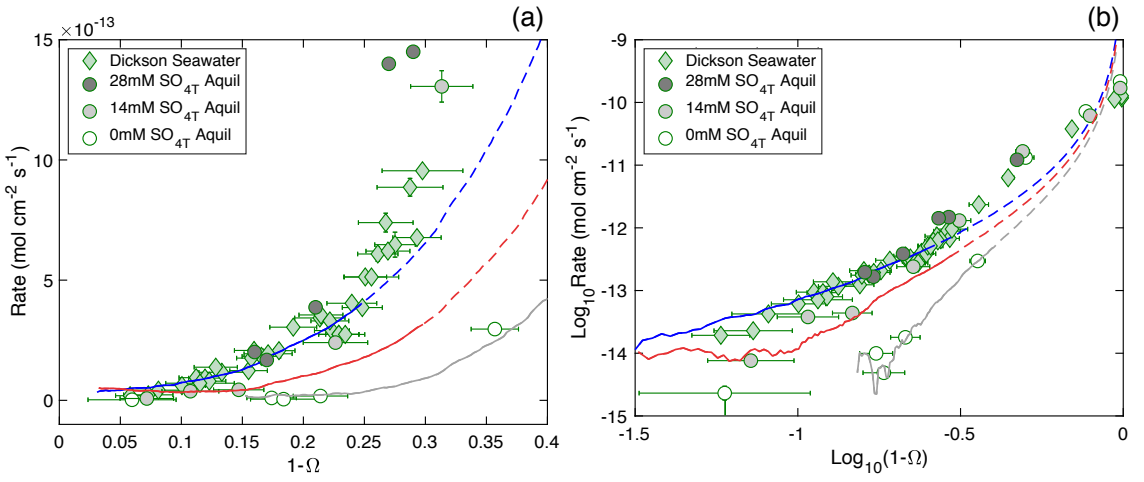

Figure 3.6: Fits of Eq. 3.4 to experimental rate (mol cm^{-2} s^{-1}) versus 1-Ω data in (a) linear axes and (b) Log-Log axes. Dissolution in Dickson seawater is fit by the blue curve, 14 mM SO_{4T} Aquil by the red curve, and 0 mM SO_{4T} Aquil by the grey curve. Data near equilibrium is well described by the model (solid lines), but extrapolating the fit to Ω = 0 (dashed lines) systematically misfits dissolution rates. Note that the chatter in the fits near equilibrium is because net dissolution is the difference between large gross dissolution and gross precipitation fluxes which have been calculated using interpolated speciation data.

As suggested by previous work (Subhas et al., 2017), dissolution rates in seawater result from the difference between large gross dissolution and precipitation fluxes. The contribution of each term in Eq. 3.4 to the overall dissolution rate is plotted in Fig. 3.7. The largest contributors to the forward rate are the k_1 and k_4 terms corresponding with attack of water and protons, respectively. Note that protons can be from H^+ or HSO_4^- in this model. The back reaction is set by k_7 and (k_6-k_3) terms, with a small contribution from the k_8 term. The (k_2-k_5) term for attack by $H_2CO_3^*$ is negligibly small.

One piece of evidence that A&M used to validate their fitted rate constants was to estimate the calcite solubility product, as $\frac{k_4}{k_8 K_{CaCO_3^0}} = \{Ca^{2+}\}\{CO_3^{2-}\} = K_{sp}^0$. We can do the same calculation using our fitted values along with the stoichiometric association constant for $CaCO_3^0$ in seawater (pK_{CaCO3} = 2.1 ± 0.1, Millero and Schreiber, 1982). Note that pK_{CaCO3} was not included in the full speciation model because of its effect on other ions in solution, but we use it here as it allows for a more accurate calculation. We recover a pK_{sp}^* of 6.23,

which is impressively close to the accepted value of 6.369 (Mucci, 1983b). The relative agreement between the calculated and known pK_{sp}^{*} values further supports the validity of our model.

Our fitted rate constants help to explain why changes in dissolution rate do not scale linearly with changes in $[SO_{4T}]$. We see from Fig X that removing sulfate lowers the gross forward rate via changes to the acidity of the solution, and the gross backwards rate via changes to the surface speciation. The k_1 term is multiplied by $[H+]_T^2$, and since the $[HSO_4^-]$ contribution to $[H+]_T$ falls with the removal of sulfate, the gross contribution of the k_1 term also falls. According to the speciation model, removing sulfate causes $>CO_3H$ sites to be replaced by $>CO_3Mg^+$ and $>CO_3Ca^+$ (Fig. 2.5c), thereby lowering the backwards (k_6-k_3) term in Eq. 3.4. The k_1 term decreases more rapidly than the (k_6-k_3) term, allowing for the net rate to scale non-linearly to the change in $[SO_{4T}]$.

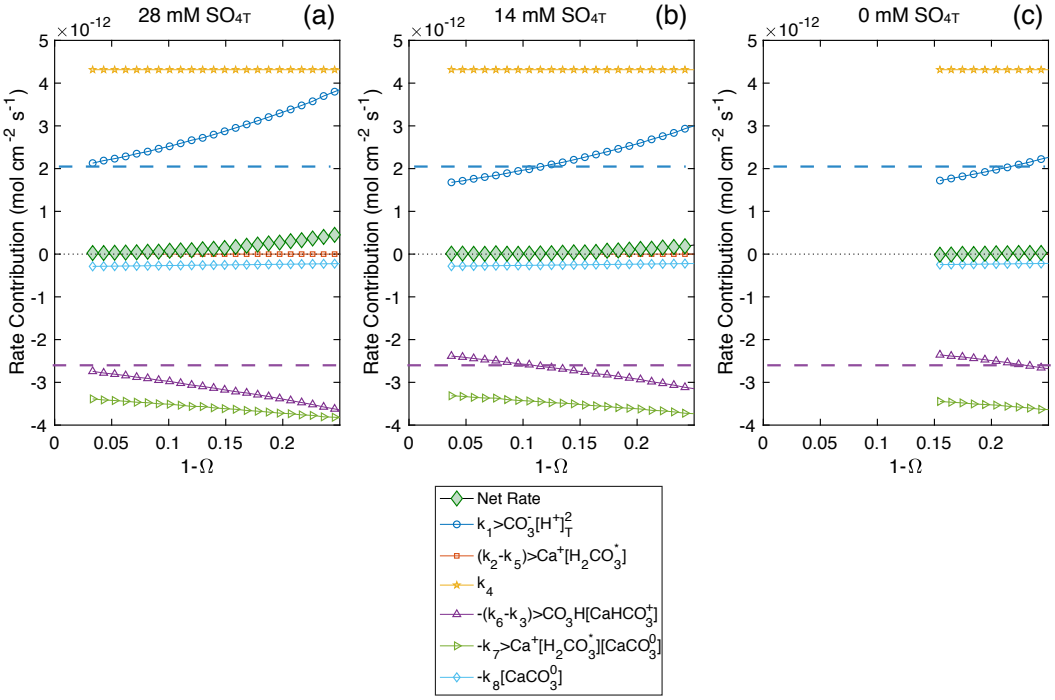

Figure 3.7: Contribution of each term of Eq. 3.4 to the overall dissolution rate in (a) Dickson seawater, (b) 14 mM SO_{4T} Aquil, and (c) 0 mM SO_{4T} Aquil. The "Net Rate" curves stop when the overall rate becomes negative. Horizontal dashed lines are provided to help see changes in the k_1 and k_6-k_3 terms between solution compositions.

3.5.4 Comparison of Model Fits in Seawater versus Freshwater

The most obvious difference when comparing fits between seawater and freshwater dissolution data is the Ω range for which Eq. 3.4 is valid. A&M fit dissolution rates from $0 < \Omega < 0.8$, whereas we are only able to fit a 0.15 Ω unit spread from $0.75 < \Omega < 0.9$ in seawater. Though the Ω ranges are much different, they approximately correspond with the same surface dissolution mechanism: defect-assisted etch pit formation. It is therefore valid to directly compare the fitted rate constants in Table 3.4.

With the exception of k_1, all rate constants are smaller in seawater than their corresponding values in freshwater (Table 3.4). This is consistent with the fact that calcite dissolves more slowly near equilibrium in seawater by >2 orders of magnitude (Naviaux et al., 2019b; Subhas et al., 2015). Though large, the magnitude of the seawater k_1 rate constant is borne

out of the measured dissolution rate changes from removing sulfate. Attempts to fit the data using a smaller k_1 value were unsuccessful.

Examining the fitted (k_2-k_5) terms suggests that the attack of $H_2CO_3^*$ is a vanishingly small contributor to the overall dissolution rate in seawater. This is an unexpected result, as carbonic anhydrase (CA), an enzyme that catalyzes the equilibration between $CO_{2(aq)}$ and $H_2CO_3^*$, has been shown to greatly increase seawater calcite dissolution rates near equilibrium (Subhas et al., 2017). It was thought that the mechanism of CA rate enhancement was through an increase in [$H_2CO_3^*$] availability, but this is challenged by our modeling results. Interestingly, the (k_2-k_5) term is the largest contributor to the overall dissolution rate in freshwater. This may be because the pCO_2 of the A&M experiments was very high ($0.2 < pCO_2$ (atm) < 1.0), leading to greater [$H_2CO_3^*$] than would occur under atmospheric pressures. However, more recent research has suggested that $H_2CO_3^*$ is irrelevant to freshwater calcite dissolution, and that pCO_2 affects the dissolution rate through changes in $>CaOH_2^+$ (Oleg S. Pokrovsky et al., 2009). Future research will be required to directly test the effect of $H_2CO_3^*$ on calcite dissolution.

Differences between freshwater and seawater dissolution may also be seen in the rate constants for the backwards reactions. A&M found that the (k_6-k_3) term was mainly responsible for lowering the dissolution rate from pH 5-6 for $pCO_2 = 0.97$ atm, but that the k_8 term was more important at lower pCO_2 (0.1 atm) or higher pH (>6.5). In seawater, we find that the k_7 and (k_6-k_3) terms contribute similarly to the backwards rate, with the (k_6-k_3) term becoming more important farther from equilibrium. The k_8 term contributes the least to the backwards reaction, likely because only ~12.4% of $CO_3^{2-}{}_T$ exists as $CaCO_3^0$ in seawater.

3.6 Summary and Conclusions

We measured calcite dissolution rates in artificial seawater of varying [SO_{4T}] across the full range of saturation states. We found that the effect of sulfate varied depending upon the distance from equilibrium. In agreement with previous studies (Sjöberg, 1978), removing sulfate increased the calcite dissolution rate by a factor of ~2 far from equilibrium ($\Omega \sim 0$). However, removing sulfate had the opposite effect for $\Omega > 0.5$, with calcite dissolution rates

in sulfate free seawater slowing by > 20x. The magnitude of rate inhibition did not scale directly with sulfate concentration. These finding have significant implications for calcite dissolution rates in ancient oceans, where sulfate concentrations were much lower than in the modern (Canfield and Farquhar, 2009; Fakhraee et al., 2019; Luo et al., 2010).

We used these dissolution measurements, along with the latest speciation models, to test if the same mechanistic rate equation developed for calcite dissolution in freshwater (Arakaki and Mucci, 1995) could also be applied to seawater. The equation is based upon four reversible reactions that capture the interaction between the solution and mineral surface chemistries. We successfully fit the equation to all of our rate measurements for $\Omega > 0.75$ using a least squares minimization technique. This Ω range corresponds with dissolution by defect-assisted etch pit formation (Naviaux et al., 2019b), which is likely the same mechanism that produced the data for the original freshwater model. We find that removing sulfate simultaneously decreases the gross forward *and* backwards rates, with the combined effect being a decrease in the net dissolution rate. Within the context of the model, the change in rate from removing sulfate is only possible if HSO_4^- is considered alongside H^+ as dissolution agents in the forward reaction. The validity of our model is supported by the fact that our fitted rate constants reproduce the value for calcite pK_{sp}^* in seawater.

Our model couples the effects of Ω with the speciations of the solution and mineral surface, and in doing so, successfully describes calcite dissolving via defect-assisted etch pit formation. We were unable to fit any of our data for $\Omega < 0.75$, where dissolution proceeds by homogenous etch pit formation. This discrepancy may be improved in the future by testing alterative models of surface speciation (Ding and Rahman, 2018; Song et al., 2019, 2017) and/or rate equations for far from equilibrium mineral dissolution (Lasaga and Lüttge, 2001; Lüttge, 2006).

Chapter 4

RATE ENHANCEMENT FROM CARBONIC ANHYDRASE: MECHANISTIC INSIGHTS FROM IMMOBILIZATION WITHIN CARBON CAPTURE REACTORS

4.1 Introduction

Humans are burning fossil fuels at an unprecedented rate, leading to accelerated melting of polar ice sheets (Chen et al., 2006; Rignot et al., 2011; Velicogna, 2009), acidification of the oceans (Doney et al., 2009; Feely et al., 2012; Zeebe, 2012), and potential increases in the strengths and/or frequencies of hurricanes (Bender et al., 2010; Emanuel, 1987; Knutson et al., 2010; Powell and Reinhold, 2007) and forest fires (Dale et al., 2001; De Groot et al., 2013; Flannigan et al., 2013; Wotton and Flannigan, 1993), among other things. Our unfettered release of CO_2 into the atmosphere is also expected to have grave economic and social consequences (Stern and Stern, 2007; Tol, 2002; Yi, 1996). Climate change represents an existential threat to humanity, but even the major changes to our energy infrastructure set forth in the Paris Climate Agreement are expected to insufficient to keep global warming below 2°C (Rogelj et al., 2016). Any emissions reduction strategy should therefore include a source of negative emissions, i.e. carbon capture and storage technologies, before it is considered viable.

The Earth's oceans will eventually neutralize anthropogenic CO_2 via the dissolution of carbonate minerals, but the natural timescale of this process is far longer (~2000-6000 years) than what is needed to avoid 2°C of global warming (Archer et al., 1998; Archer and Maier-Reimer, 1994; Boudreau et al., 2010; Cao et al., 2009; Ilyina and Zeebe, 2012; Lenton et al., 2006; Ridgwell and Zeebe, 2005; Sundquist, 1990). One proposed strategy is to decouple the timescales of carbonate dissolution and ocean circulation by acidifying reactor vessels with CO_2-rich flue gas (Caldeira and Rau, 2000; Rau et al., 2007, 2001; Rau and Caldeira, 1999). This acidified water could then be used to dissolve carbonates, effectively capturing and storing CO_2 in the form of bicarbonate. This idea has been bolstered by the discovery that an enzyme, carbonic anhydrase (CA), increases carbonate dissolution rates by orders of

magnitude (Dreybrodt et al., 1996; Li et al., 2009; Subhas et al., 2017; Xie and Wu, 2014; Zaihua, 2010).

Carbonic anhydrase is found in nearly all animals and photosynthesizing organisms, and it catalyzes the reversible hydration of carbon dioxide to bicarbonate:

$$CO_2 + H_2O \leftrightarrows H^+ + HCO_3^- \leftrightarrows H_2CO_3 \qquad \text{Eq. (4.1)}$$

The catalytic mechanism of CA involves the attack of a zinc-bound OH^- on a CO_2 molecule captured within a hydrophobic pocket. The resulting HCO_3^- ion is displaced into solution by H_2O, where it rapidly equilibrates with H_2CO_3. The zinc-bound OH^- is regenerated by transferring a H^+ from the newly acquired water molecule onto His-64, which then shuttles the proton onto buffer molecules in solution (Lindskog, 1997).

Though the mechanism of CO_2 hydration by CA is known, the mechanism by which the enzyme enhances carbonate dissolution rates is not. The H^+ generated during the CO_2 hydration process is often thought to be responsible for dissolution enhancement (Dreybrodt et al., 1996; Pokrovsky et al., 2005), but H_2CO_3 is also plausible (Subhas et al., 2017), as it is an important nucleophile in dissolution rate laws (Arakaki and Mucci, 1995; Busenberg and Plummer, 1986; Chou et al., 1989; Plummer et al., 1979b). A detailed study is required to understand the dissolution catalysis of CA, and the results will inform the design of any reactor hoping to harness the catalytic effects of the enzyme. From a practical standpoint, this is because CA must be retained within a dissolution reactor to be economically feasible. The most promising ways to retain CA are by physically trapping the enzyme within porous hydrogels (reviewed in Avnir et al., 1994), or by chemically linking it to controlled pore glass (CPG, reviewed in Weetall, 1993). CA may be physically separated from the mineral if dissolution is catalyzed via an increase in the concentration of carbonic acid in solution. However, if CA catalyzes dissolution via direct proton transfer onto the surface (if the mineral is the “buffer molecule” that accepts the proton from His-64), then a reactor design will need to allow for the intimate association of CA with the mineral surface.

In this chapter, we construct prototype fluidized bed and packed bed carbonate dissolution reactors for use as CO_2 capture and storage devices. We implement methods for retaining CA within hydrogels and on the surface of CPG beads, and we evaluate the resulting effects on the activity and effective lifetimes of the enzyme. Finally, we combine our fixed CA products with our reactors and use the results to understand the mechanism by which the enzyme enhances calcite dissolution rates.

4.2 Methods

4.2.1 Reactor Designs

Dissolution catalysis of crushed carbonate rock was evaluated using both fluidized bed and packed bed reactors. Fluidized bed reactors (Fig. 4.1) were fabricated using 50 cm lengths of clear PVC pipe (McMaster-Carr item #49035K48), ¼" NPT fittings, tygon tubing, polycarbonate powder funnels, and stainless-steel mesh (0.034" pore size, McMaster-Carr item# 85385T91). The base of each reactor was made by cutting a funnel in half, placing stainless-steel mesh in between the newly separated pieces, and epoxying the funnel back together and onto the PVC pipe. After assembly, carbonate rock was poured into the base and a peristaltic pump was used to flow either seawater (starting alkalinity 1900 μmol kg^{-1}) or tap water (starting alkalinity of 1200 μmol kg^{-1}) into the reactor. Excess water drained out of the top port such that the steady volume of each reactor was 300 mL during operation. Dissolution progress was monitored using open-system gran titration to measure the alkalinity of the reactor outflow at regular time intervals. CA was purchased in its lyophilized form from Worthington Biochemical Co. (item # LS001263) and either dissolved directly into the inflow water stream or added in an immobilized form as discussed below.

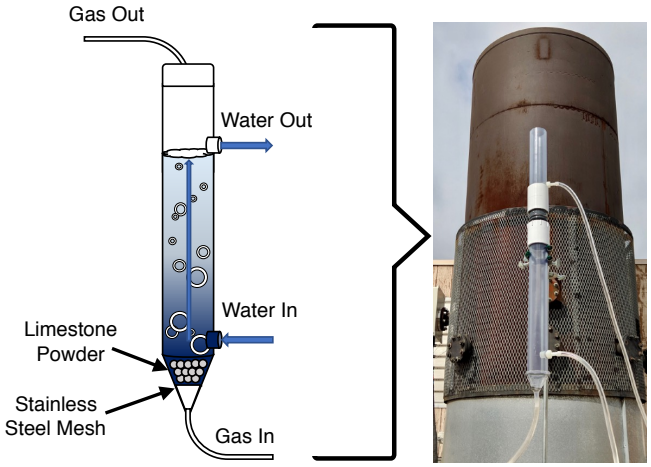

Figure 4.1: Schematic of fluidized bed reactor (left) and full assembled reactor (right)

The reactor carbonate bed was fluidized using either a compressed gas line (10% CO_2, balance N_2) or a diaphragm air pump. The diaphragm pump was used to test dissolution rates when flowing in either ambient air or 3% CO_2 sourced from the Caltech cogeneration powerplant smokestack. To prevent diffusion limitation of the dissolution rate, the minimum gas flow rate required for bed fluidization (u_{mf}, cm s^{-1}) was calculated according to:

$$u_{mf} = \frac{(\Psi d_p)^2}{150\mu}[g(\rho_p - \rho_{fluid})]\frac{\varepsilon^3}{1-\varepsilon} \qquad \text{Eq. (4.2)}$$

Here, Ψ is the sphericity of the particles in the bed (ranging between 0.5 and 1, with 0.6 being typical for a granular solid), d_p is the average diameter of the particles (cm), μ is the viscosity of the inflow gas ($1.86 \cdot 10^{-4}$ g cm^{-1} s^{-1} for air), g is acceleration due to gravity (980 cm s^{-2}), ρ_p is the density of the particles (2.71 g cm^{-3} for calcite), ρ_{fluid} the density of the inflow gas ($1.2 \cdot 10^{-3}$ g cm^{-3} for air), and ε is a measure ranging from 0-1 of the porosity of the particles when fluidized (assumed value of 0.5).

The size fraction of carbonate rock to use in the reactor was chosen with care, as u_{mf} increases with the square of the particle diameter. Large grain rock is most realistic for an industrial application, but given a 3 cm bed diameter (midpoint diameter of the funnel), a 1-

2 mm size fraction required a gas flow rate of ~82 L min^{-1}. Initial experiments used this larger grain size of rock, but the fast flow rate drained a full tank of compressed CO_2 gas within 12 hours, 10 hours of which were required for the alkalinity of the reactor to reach steady state. Later experiments were conducted using a 0.25-0.5 mm rock size fraction because they required a lower gas flow rate (calculated 5.1 L min^{-1}) and could achieve steady state alkalinity more quickly.

Packed bed reactors were made from 30 mL buchner filter funnels with 40-90 μm pore size fritted discs (VWR catalog # 10546-042). Each reactor was filled with 48 g of crushed carbonate rock and topped with a greased rubber stopper that had been threaded with a section of tygon tubing. A larger rock size fraction (1-2 mm) was used because there was a greater chance of observing a catalytic rate enhancement when testing slower dissolution rates. A peristaltic pump was used draw seawater (starting alkalinity 1900 μmol kg^{-1}) from a 4 L reservoir and push it continuously through the packed bed. The seawater was acidified prior to beginning each experiment by bubbling in 10% CO_2 for a minimum of one hour. The reaction progress of the experiment was monitored by measuring the alkalinity of the effluent.

4.2.2 CA Immobilization Strategies

CA was physically trapped within polyethylene glycol diacrylate (PEGDA) hydrogels following the method outlined in Blanchette et al. (2016). Briefly, CA was mixed together with pH 7 phosphate buffer solution, PEGDA macromer, and photoinitiator. The resulting solution was then cured into a solid hydrogel via exposure to UV light. We tested a suite of PEGDA sizes (Laysan Bio Item# ACRL-PEG-ACRL-4MW Kit), PEGDA concentrations, photoinitiators ("2H2M" VWR item #H0991-25G, and "TPO-Li," a proprietary agent from CPS Polymers), and UV intensities ($1 \cdot 10^{-3}$ – 1 W cm^{-2}) to find a combination that optimized CA activity and lifetime (activity measurements detailed in Section 4.2.3) . The UV lamps used were a handheld 365nm lamp ($1 \cdot 10^{-3}$ W cm^{-2}, Fisher Scientific catalog # UVP95000602), a small 405nm lamp (0.6 W cm^{-2}, Peopoly UV curing light), and a 405nm UV flood lamp (1 W cm^{-2}, Loctite IDH: 1359255 for controller, 2139180 for lamp).

Curing times ranged from 5 minutes at the weakest UV intensity to 10 seconds at the strongest. Note that PEGDA macromer comes as a solid powder, so its concentration in solution is defined in terms of weight percentage. For example, 50 mg of PEGDA added to 500 mg of buffer solution is referred to as a 10% PEGDA solution.

Table 4.1: Summary of Hydrogel Materials	
PEGDA MW (g mol^{-1})	575, 5k, 10k, 20k
Photoinitiators	2-hydroxy-2-methylpropiophenone ("2H2M"), TPO-Li
UV lamps	365nm ($1 \cdot 10^{-3}$ W cm^{-2}), 405nm (0.6 W cm^{-2}), 405nm (1 W cm^{-2})

Pure hydrogels were cured into various shapes and evaluated for mechanical robustness and CA activity. Porous silicone sheets (PS sheets) provided by the Baker lab at Lawrence Livermore National Lab were also tested as a material to potentially balance the durability and surface area of the hydrogel. The ~1 mm thick sheets were fabricated according to a proprietary process adapted from previous work (Durban et al., 2018) and were delivered to Caltech in deionized water. The PS sheets were stable for several months. To cure CA-hydrogel within the PS sheet, the sheet was first cut to the desired size (typically 1 cm^2) and then dehydrated by gently patting with a Kimwipe. A 20-50 μL drop of PEGDA-enzyme solution was placed on the sheet and absorbed via capillary action. The PS sheet was then placed under UV light and cured for 10 seconds to 5 minutes, depending upon the UV light intensity.

Through a large amount of trial and error, a research scientist in our group, Dr. Panqing He, adapted previous work (Thakur et al., 2007; Weetall, 1993) to design a method for chemically linking CA to aminated CPG beads. The first step of the process is to exchange the amine groups on the surface of the glass beads with glutaraldehyde (GA) groups. Aminated CPG beads (LGC Biosearch Technologies catalog #BG1-2000-10) were prepared for functionalization by wetting them in a stirred beaker of 70-80°C 18 MΩ cm^{-1} water for 1 hour. Once the beads ceased floating and began to sink, they were heated for an additional 30 minutes and then taken off the hotplate to cool. The beads were subsequently placed in 4-

5 g batches into a lined Buchner funnel and dried under vacuum. In order the replace the CPG amino groups with GA linkers, the beads were rinsed while under vacuum with a 2.5% GA solution made by diluting 50% GA (VWR item #97064-690) with 50 mM pH 7 phosphate buffer solution. 250 mL of 2.5% GA was rinsed over the beads over a 1-hour period.

Once functionalized, the CPG beads were ready to be coupled with CA. A concentrated enzyme solution was created by adding 12 mg of CA to a 0.1 M pH 7 phosphate buffer for every gram of CPG beads to be reacted. The beads and enzyme solution were stirred together in a beaker at room temperature for one hour. 1 mL samples of the enzyme solution were taken at 0, 3, 10, and 60 minutes for later testing of the reaction progress using protein UV absorbance spectroscopy. After reacting for an hour, the beads were filtered from the solution and rinsed under vacuum in a Buchner funnel with 500 mL of 50 mM pH 7 phosphate buffer.

The last step of the process was to block unreacted GA sites on the CPG beads and remove loosely bound CA. The coupled CA-CPG beads were stirred together with a 0.1 M pH 7 glycine solution for 1 hour 45 minutes at room temperature. Loosely bound proteins were then removed from the CPG beads by heating the glycine-CPG solution at 50°C for 30 minutes. Finally, the CA-CPG beads were filtered and stored at 5°C in 50 mM pH 7 phosphate buffer. The amount of CPG-bound CA was estimated from the decrease in UV absorbance at 280 nm of the 1 mL enzyme solution samples. The absorbance typically decreased by ~85% from t = 0 minutes to t = 60 minutes, indicating a maximum loading of ~ 10 mg CA per mg CPG beads.

4.2.3 MIMS Method for CA Activity and Lifetime Measurements

The activities of free CA, CA-CPG beads, and CA hydrogels were evaluated using a Pfeiffer QMG 220 Membrane Inlet Mass Spectrometer (MIMS) following the methods developed by Subhas (2017). In this method, a $H^{13}C^{18}O_3$ isotope spike is injected into pH 8 phosphate buffer solution alongside the desired amount of enzyme, and the activity is determined by the rate of depletion of ^{18}O from aqueous $^{13}CO_2$. The fraction of ^{18}O isotopologues of $^{13}CO_2$ was calculated according to:

$$f^{18} = \frac{2(49)+(47)}{2[(45)+(47)+(49)]} \qquad \text{Eq. (4.3)}$$

Here (45), (47) and (49) are the ion currents measured by the MIMS at those *m*/*z* values. The rate of hydration/dehydration was calculated from the slope of $\ln(f^{18})$ s^{-1} (Mills and Urey, 1940; Silverman and Tu, 1976; Subhas, 2017; Uchikawa and Zeebe, 2012). After an initial equilibration period, $\ln(f^{18})$ s^{-1} decreases linearly in proportion to the activity of CA (Subhas, 2017). A typical activity measurement could be completed in 8-10 minutes.

The original reactor vessel designed by Subhas (2017) was too small to accommodate the hydrogel samples, so a custom 40 mL glass beaker was fabricated and used instead (Figure **4.2**). The new reactor required 10 µL of isotope spike in 35 mL of buffer solution. CA-CPG beads were mechanically robust enough to withstand stirring in the reactor, but the hydrogels would break apart and leak enzyme, thereby complicating the resulting activity calculation. Hydrogels were therefore placed in a specialized housing unit made from the base of a 10 mL Falcon tube. Holes were drilled into the Falcon tube to allow the solution to flow through the housing unit during the MIMS measurement (Figure **4.2**).

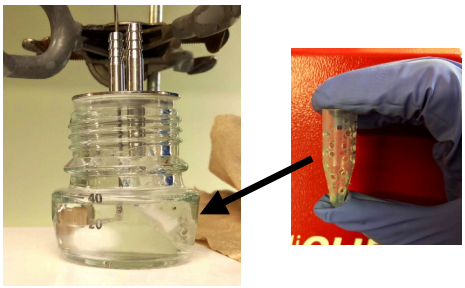

Figure 4.2: Custom 40 mL MIMS sample reactor (left) with hydrogel housing unit (right)

CA samples were systematically tested in the MIMS over time to determine the rate of activity loss. Lifetimes were assessed for samples stored only in buffer solution ("passive" conditions), and for samples placed in seawater being continuously bubbled with 10% CO_2 gas ("active" conditions). Samples were only tested under active conditions if they were shown to maintain activity under passive conditions.

4.3 Results and Discussion

4.3.1 Fluidized Bed Reactors

The results from the fluidized bed reactors are listed in Table 4.2, and plotted for the 0.25-0.5 mm size fraction experiments in Figure **4.3**. Reactors were run in pairs so that one could serve as a control while the test reactor had CA added to its water inflow stream. Bed fluidization was observed in all reactors at a gas flow rate of 5.2 L min^{-1}, in good agreement with the 5.1 L min^{-1} calculated from Eq. (4.2). Note that reactors in the lab were run with seawater bubbling 10% CO_2, while all other reactors were run with tap water. Vertical black dashed lines indicate where the flow rates of the reactors were changed. The vertical red lines in panel (C) indicate times when the reactor was reset due to pump failure and subsequent flooding of the tubing (first line), or due leaks forming in the reactor base (second line).

Table 4.2: Results from fluidized bed reactors

Flow Rate (mL min^{-1})	Rock Size (mm)	Added Alk without CA (µmol kg^{-1})	Added Alk with CA (µmol kg^{-1})	CA Benefit (µmol kg^{-1})	% Change	Extra CO_2 Captured (g yr^{-1})	Cost ($ g^{-1} extra CO_2)
Compressed Gas Tank (10% CO_2)							
5.0	1-2	2820 ± 86	-	-	-	-	-
2.5	1-2	4220 ± 133	5044 ± 50	824 ± 142	19.5 ± 3.1	23.8 ± 4.1	1465
1.0	0.25-0.5	5863 ± 163	7359 ± 141	1496 ± 216	26 ± 4	17.3 ± 2.5	800
CoGen Powerplant Smokestack (3% CO_2)							
8.0	0.25-0.5	3040 ± 59	3387 ± 26	347 ± 65	11.4 ± 2.1	32.1 ± 6.0	3,500
4.0	0.25-0.5	3327 ± 19	3537 ± 27	210 ± 33	6.3 ± 1.0	9.7 ± 1.5	5,800
2.0	0.25-0.5	3672 ± 42	3785 ± 29	113 ± 51	3.1 ± 1.4	2.6 ± 1.2	10,600
Ambient Air							
2.0	0.25-0.5	1093 ± 304	1078 ± 281	None	-	-	-

Extra CO_2 capture rate calculated by converting the "CA Benefit" at a given flow rate assuming a 2:1 Alk:CO_2 conversion

CA Cost calculated assuming price of $1876 g^{-1} (price from Worthington Biochemical Co. August 2019) and calculating the total CA used in 1 year at the designated flow rate and [CA] = 14.15 mg L^{-1}

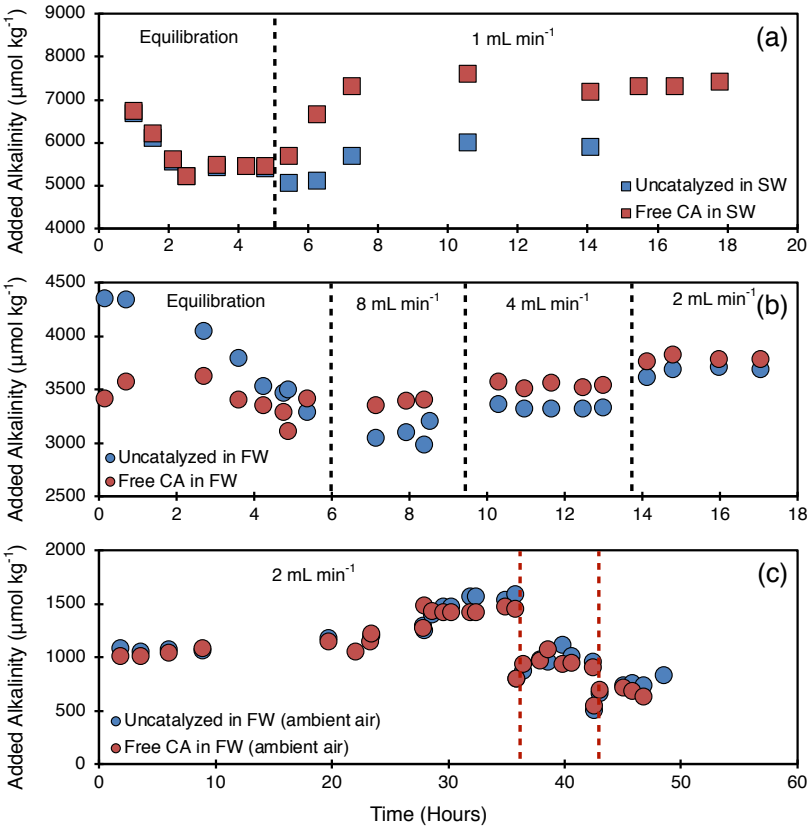

Figure 4.3: Increase in effluent alkalinity for fluidized bed reactors operating on a) 10% CO_2 in seawater (starting alk 1900 µmol kg^{-1}), b) 3% CO_2 from the Caltech powerplant smokestack in freshwater (FW, starting alk 1200 µmol kg^{-1}), c) Ambient air in freshwater. Reactors with 14 mg CA L^{-1} are in red. Dashed vertical lines indicate changes in the water inflow rate. Red vertical lines in c) indicate reactor structural failures (see text for details).

The added alkalinity (defined as alkalinity in excess of the solution starting alkalinity) for each reactor pair was proportional to the % CO_2 of the inflow gas, and inversely proportional to the water inflow rate. These trends make sense, as higher CO_2 concentrations increase the chemical driving force of the solution (decrease Ω), and lower inflow rates increase the time a volume of liquid can react with the carbonate bed. For uncatalyzed reactors dissolving in freshwater at an inflow rate of 2 mL min^{-1}, the added alkalinity increases from 1093 ± 304 to 3672 ± 42 µmol kg^{-1} when switching from ambient air (Figure **4.3**c) to 3% CO_2 (Figure **4.3**b). Although not directly comparable due to the use of seawater as opposed to freshwater,

the added alkalinity reached 5863 ± 163 μmol kg^{-1} when fluidizing reactors with 10% CO_2 in the lab (Figure **4.3**a).

After an initial equilibration period, 14.15 mg mL^{-1} CA was added to the inflow water stream of one reactor in each reactor pair**.** CA increased the effluent alkalinity by as much as 26 ± 4% in the lab (10% CO_2), and 11.4 ± 2.1% for reactors attached to the Caltech cogeneration powerplant smokestack (3% CO_2). CA had no effect when reactors were fluidized using ambient air, emphasizing the need to concentrate CO_2 to decrease Ω in real world implementations of these reactors.

The added alkalinity at a given flow rate was converted to a CO_2 capture rate by assuming a molar equivalence of 2:1 added Alk:CO_2 and using the molar mass of CO_2. For powerplant reactors, the added CO_2 that was captured when using CA followed an empirical power law dependence on the reactor overturning rate (defined as the reactor volume divided by the water inflow rate, units of hours):

$$\text{Added } CO_2 \text{ Capture}_{(gCO_2\ yr^{-1})} = 14(\text{Overturning Rate})^{-1.8} \qquad \text{Eq. (4.4)}$$

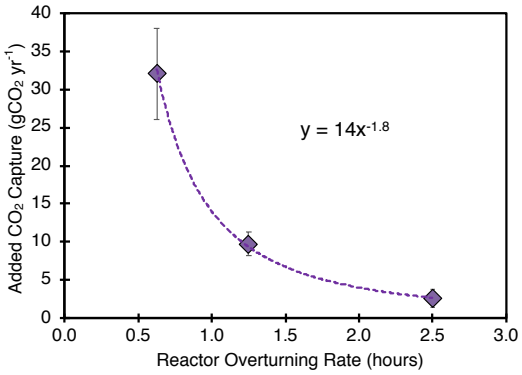

Figure 4.4: Amount of extra CO_2 captured (gCO_2 yr^{-1}) in reactors operating with 14 mg CA L^{-1} in freshwater versus the reactor overturning rate (hours, calculated from reactor volume divided by the water inflow rate). The relation follows an empirical power law dependence.

CA appears to have the largest relative effect when dissolution rates are fast, either due to low solution Ω from fast flow rates, or due to the dissolution of finer grained material. This is initially surprising considering that CA increases dissolution rates by 250x near equilibrium versus just 2x far from equilibrium (Subhas et al., 2017), but it is a reminder that Ω is the first order determinant of dissolution rates. Increased flow rates keep the reactor Ω at lower levels, allowing CA to improve upon a dissolution rate that is already quite high. The importance of Ω also explains why CA had no effect when running reactors with ambient air. The relatively low CO_2 content of ambient air did not change the solution Ω significantly, and without an overall chemical driving force to act alongside, CA could have no effect.

The data from the fluidized bed reactors demonstrate the challenges of scaling up for real world applications. In order to combat climate change effectively, a reactor must capture as much CO_2 as possible at the lowest marginal cost. Adding free CA to the reactors can boost carbon capture rates by 20+%, but CA is expensive, and the marginal cost of the captured CO_2 is on the order of several hundred dollars per gram (Table 4.2). Immobilizing CA such that it remains in the reactor offers a way to decouple the dissolution rate improvements from the prohibitively expensive cost of the enzyme.

4.3.2 Physical Immobilization of Hydrogels

CA was successfully incorporated into a wide range of hydrogels, the results of which are summarized in Table 4.3. The first iterations of hydrogels were cured as thin cylinders within 1 mL syringes using 2H2M photoinitiator (Figure **4**.**5**a), while subsequent trials used TPO-Li photoinitiator and higher UV strengths (Figure **4**.**5**b). The results for each recipe were similar. The MIMS activity assays of the cylinders showed evidence of diffusion limitation into and out of the gel (Figure **4**.**5**c). Compared to free CA which exhibits a linear decrease in $\ln(f^{18})$ over time (Subhas, 2017), the CA-hydrogel cylinders produced a curved slope. Activity measurements were therefore standardized by time to only include data from 200-350 seconds. Cutting the CA cylinder into smaller pieces produced activity measurements that scaled directly with the increase in surface area (Figure **4**.**5**d). Smaller hydrogel pieces also demonstrated less curvature in the MIMS activity assay.

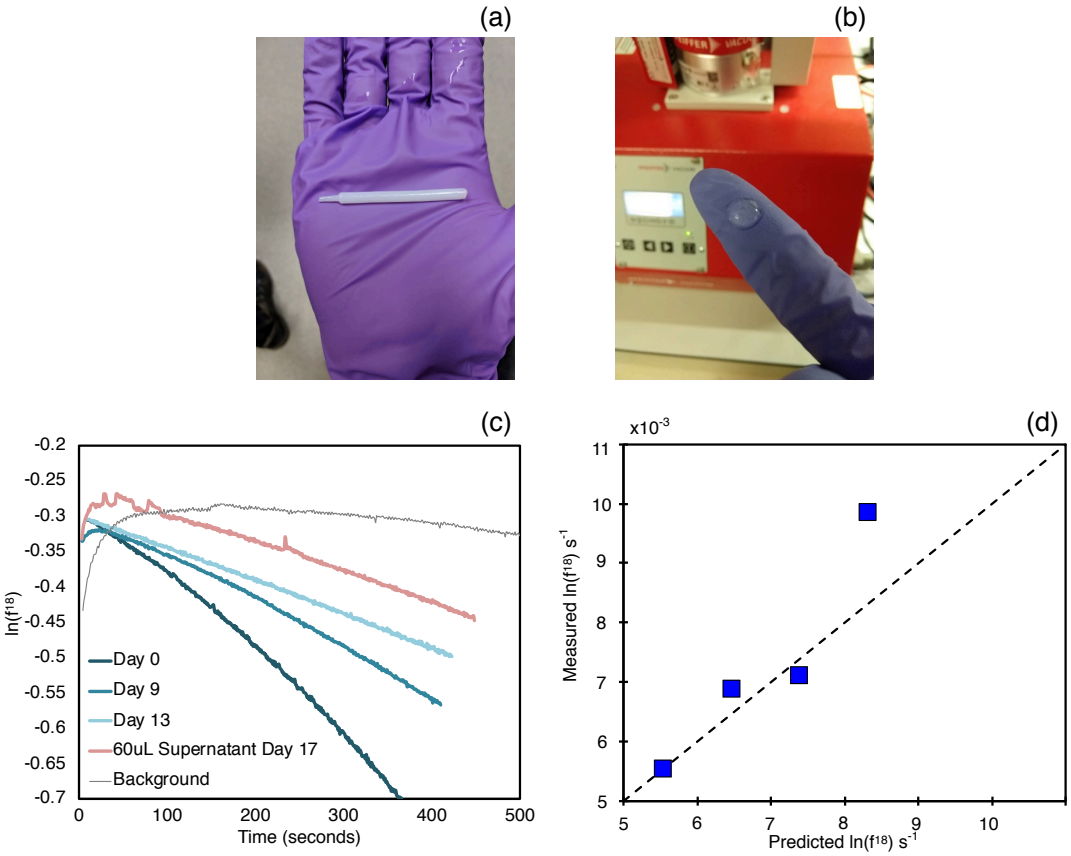

Figure 4.5: Representative CA-hydrogels a) cured in a 1 mL syringe using 2H2M photoinitiator with a $1 \cdot 10^{-3}$ W cm^{-2} 365 nm UV lamp and b) using LAP photoinitiator with a 1 W cm^{-2} 405 nm UV lamp. MIMS activity assays of c) ln(f^{18}) versus time of the same hydrogel tested over multiple days, and d) measured versus predicted activity for a hydrogel subdivided into smaller pieces. The dashed line in d) is the 1:1 measured:predicted activity based upon the increase in surface area from subdividing the hydrogel.

Table 4.3: Summary of Hydrogel Experiments						
PEGDA size (g mol^{-1})	% PEGDA	Lamp Strength (W cm^{-2})	Initiator	Activity · 10^{-3} ln(f18) s^{-1} $mgCA^{-1}$	% of Free CA Activity	Retain Activity (Y/N)?
Pure Hydrogel						
575	10	$1{\cdot}10^{-3}$	2H2M	6.2	2.1	N
		$1{\cdot}10^{-3}$	LAP	3.0	1.0	N
		0.6	**LAP**	**64**	**21**	**N**
	15	$1{\cdot}10^{-3}$	2H2M	4.8	1.6	N
	20	0.6	LAP	4.2	1.4	N
		$1{\cdot}10^{-3}$	2H2M	1.3	0.4	N
	25	$1{\cdot}10^{-3}$	2H2M	1.0	0.3	N
	30	$1{\cdot}10^{-3}$	2H2M	0.8	0.3	N
		0.6	LAP	2.8	0.9	N
	40	$1{\cdot}10^{-3}$	2H2M	0.14	0.05	N
	50	$1{\cdot}10^{-3}$	2H2M	0.10	0.03	N
5K	**12**	**1**	**LAP**	**30**	**10**	**N**
10K	**12**	**1**	**LAP**	**39**	**13**	**N**
20K	12	$1{\cdot}10^{-3}$	LAP	0.6	0.2	N
	24	$1{\cdot}10^{-3}$	LAP	0.8	0.3	N
Curing Within Porous Silicon Sheets						
575	10	$1{\cdot}10^{-3}$	LAP	2.0	0.7	N
		0.6	LAP	9.6	3.2	N
	20	0.6	LAP	1.6	0.5	N
	30	0.6	LAP	5.6	1.9	N
		$1{\cdot}10^{-3}$	LAP	2.1	0.7	N
3.4K	12	1	LAP	12	3.8	N
5K	12	1	LAP	22	7.2	N
10K	12	1	LAP	16	5.2	N
20K	12	$1{\cdot}10^{-3}$	LAP	0.2	0.7	N
	24	$1{\cdot}10^{-3}$	LAP	0.2	0.6	N

The CA-hydrogels showed promising initial activity levels, but this activity was short lived. Assaying 60 µL of storage solution produced activity levels above the background solution, indicating that the hydrogels were leaking CA (Figure **4.5**c). This was surprising, considering that previous work has shown that PEGDA sizes up to 20K g mol^{-1} should be capable of retaining a 30 kDa protein such as CA (Cruise et al., 1998). In an attempt to alleviate enzyme

leakage, we systematically increased the percentage of PEGDA relative to buffer solution (Figure **4.6**). While this increase helped the CA-hydrogels to maintain their activity for up to two weeks, the magnitude of the activity was too low to realistically be of use in a reactor. Indeed, even the best pure CA-hydrogels had an initial activity mg^{-1} that was only 10-20% of the free enzyme. This low activity level could be useable if there were no losses over time, but the activity decreased to < 1% of the original value after 2 weeks under passive storage conditions. Increasing the UV lamp intensity led to improvements in initial activity (max of $2.6 \cdot 10^{-2}$ $\ln(f^{18})$ s^{-1} $mgCA^{-1}$), but the resulting hydrogels still lost 90% activity after 2 hours and were therefore not tested over longer time periods.

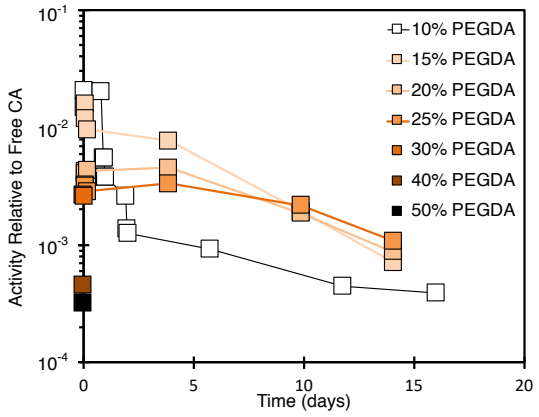

Figure 4.6: MIMS activity $mgCA^{-1}$ over time of a suite of PEGDA-575 hydrogels relative to activity mg^{-1} of free CA (hydrogel activity / free CA activity).

Another impediment to the use of CA-hydrogels in the reactors was their poor mechanical durability. Gels would break apart under moderate stirring conditions, causing faster leakage of CA into the surrounding solution.

Regardless of the aforementioned downsides, pure CA-hydrogels were introduced into a fluidized bed reactor in an effort to test if MIMS activity corresponded with dissolution catalysis. A total of 70.2 mg CA were cured into hydrogels and subdivided into 203 cylindrical pieces, each approximately 3-5 mm tall and 3-5 mm in diameter. The activity of a 15-piece subset was 0.0115 $\ln(f^{18})$ s^{-1}, so the estimated activity of all 203 pieces was 0.155

$\ln(f^{18})$ s^{-1}. This activity level was equivalent to 0.52 mg of free CA, for an effective CA concentration in the reactor of 1.73 mg L^{-1}. Although low, this amount of CA should have theoretically produced a measurable change in alkalinity. 14.15 mg L^{-1} of dissolved CA resulted in an alk increase of ~1500 μmol kg^{-1}, so assuming catalysis scales linearly with [CA], 1.73 mg CA L^{-1} should cause an increase of 183 μmol kg^{-1}, just above the ± 100 μmol kg^{-1} reproducibility of reactor alk titrations. The hydrogels were placed in a Falcon tube with pre-drilled holes (similarly to the housing unit for the MIMS assay) and suspended midway up the reactor using twine. No change in the alkalinity of the reactor effluent was observed over a period of 3 hours. Although not a definitive test due to the low effective activity of the hydrogels, it reaffirmed that large improvements would need to be developed if pure hydrogels were to be realistically implemented as reactor catalysts.

CA-PEGDA solutions were also cured within PS sheets (Table 4.3). Although this greatly improved the mechanical durability of the hydrogels, the best activity mg^{-1} that was achieved was still only 7.2% of free CA. The CA-PS-hydrogels did not show any improvement in enzyme retention.

4.3.3 Coupling CA to CPG Beads

CA-CPG beads demonstrated marked improvements in mechanical durability, activity, and activity retention relative to their CA-hydrogel counterparts. Freely dispersed CA-CPG beads ranged in activity between 11-80% activity mg^{-1} relative to free CA, depending upon the batch (Table 4.4). The density of the coupled CA-CPG beads was marginally greater than water, so the beds would stay suspended in solution for ~15-20 minutes after being dispersed. This density made the beads difficult to incorporate into reactors, as they were quickly lofted out of the reactor and clogged any filter put in their path, even at very low flow rates.

Table 4.4: Summary of CA-CPG Activity				
CA Type	Activity · 10^{-3} $\ln(f^{18})$ s^{-1} $mgCA^{-1}$	% of Free CA Activity	Lifetime (passive)	Lifetime (active)
Free CA	300	100	> 1 year	45 minutes
Dispersed CA-CPG	33.6-240*	11-80	> 6 months	> 30 hours
CA-CPG in mesh bag	12	4	> 6 months	> 30 hours
*Activity of CA-CPG beads depended upon the batch, with the highest activity mg^{-1} being 80% of free CA				

Figure 4.7: CA-CPG beads dispersed in 50 mM pH 7 phosphate buffer (left) and sealed within 70 μm mesh bags (right)

To rectify the problem of CA-CPG bead loss, beads were sealed within 70 μm pore size mesh bags (Figure **4.7**). This prevented the loss of CA-CPG beads due to lofting, but the extra diffusion limitation imposed by the bag decreased the activity of the beads by an order of magnitude, making them equivalent to CA-hydrogel activity. However, sealing the beads enabled repeated lifetime measurements of the same exact material under active conditions of bubbling with 10% CO_2 (Figure **4.8**). CA-CPG beads showed excellent activity retention under active bubbling conditions. Free CA lost all activity within 3 hours, whereas CA-CPG beads maintained 100% of their initial activity for 30 hours of active bubbling. CA-CPG beads also maintained > 50% of their initial activity for over 6 months when stored in passive conditions.

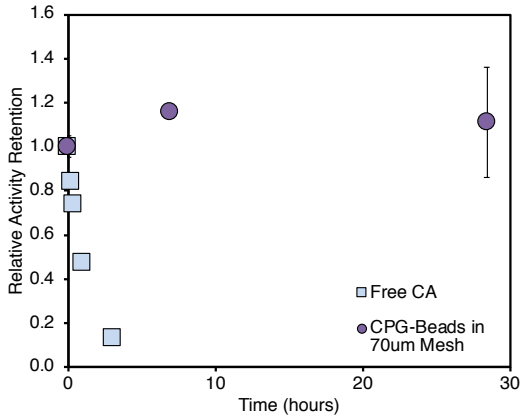

Figure 4.8: Relative activity retention (measured activity / initial activity) of free CA (squares) and CA-CPG beads in 70 μm mesh bags (circles) versus time spent in solution bubbled with 10% CO_2.

Given the excellent activity retention of CA-CPG beads, it then came to test if they could be used for dissolution catalysis. Two packed bed reactors were filled with 48 g of 1-2 mm carbonate rock and run in parallel at a water inflow rate of 3.4 mL min^{-1}. This flow rate gave a residence time of fluid in the reactor of < 10 minutes, which Eq. (4.4) implies should allow for greater relative contributions of CA to the overall alkalinity signal. After an initial equilibration period, 1 g of CA-CPG beads was mixed into the test reactor. The activity of the beads within 70 μm bags had been measured using the MIMS to be 0.12 ($ln(f^{18}) s^{-1}$) per gram. Using the measured activity of free CA of 0.3 mg^{-1}, the added beads had an activity equivalent to 0.12/0.3 = 0.4 mg of free CA. The volume of the reactor was 30 mL, so the equivalent concentration of CA was 13.4 mg L^{-1}. The activity was estimated using measurements from CA-CPG beads in bags, and therefore represents a low end estimate relative to what would be calculated using freely dispersed bead activity.

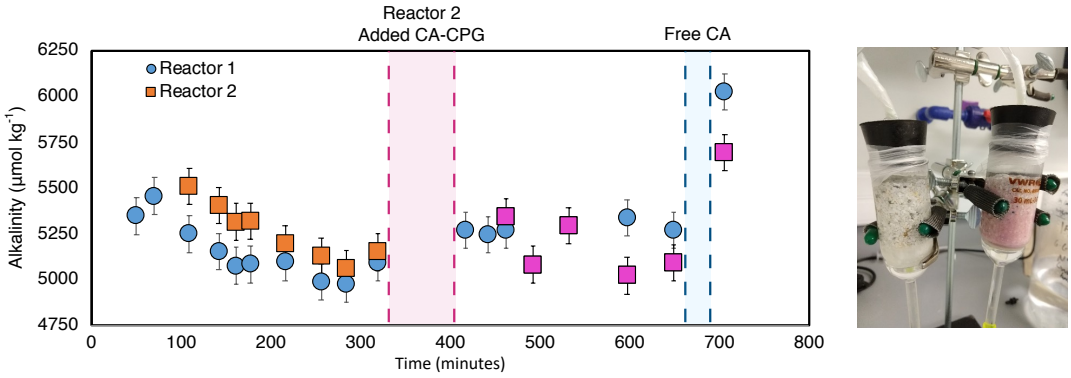

Figure 4.9: Total alkalinity versus time (left) for packed bed dissolution reactors (right). Two reactors were run in parallel at a flow rate of 3.2 mL min^{-1} of seawater. After an initial equilibration period, 1g of CA-CPG beads were mixed into Reactor 2 (pink coloring in the reactor in the right panel). When no change in alkalinity was observed, 15 mg L^{-1} of free CA was added to inflow streams of both reactors.

Beyond some alkalinity fluctuations due to recalibrating the water inflow rate, there was no difference in alkalinity between the two reactors (Figure **4.9**). To ensure that the lack of change was not due to the reactor malfunction, 15 mg L^{-1} of free CA was added to the inflow streams of each reactor. This amount was chosen was it would produce an equivalent MIMS activity as estimated for the CA-CPG beads. The free CA caused the alkalinities of each reactor to increase by ~10%, from ~ 5250 to 5900 µmol kg^{-1}.

The results from the packed bed reactors match those conducted by Dr. He (personal communications) and suggest that the mechanism of CA dissolution catalysis is via direct proton transfer from His-64 to the mineral surface, and not by an increase in the effective concentration of H_2CO_3. This mechanistic insight is consistent with results in freshwater dissolution that showed that H_2CO_3 had no effect on dissolution rates (Pokrovsky et al., 2005). It is also consistent with the mechanistic model of seawater calcite dissolution presented in Chapter 3 of this thesis, where the H_2CO_3 attack term was effectively 0.

4.4 Summary and Conclusions

We designed a fluidized bed reactor capable of sequestering CO_2 from concentrated gas streams both in the lab and directly from a powerplant smokestack. We found that freely dissolved CA catalyzed dissolution rates more effectively in reactors operating with higher % CO_2 gas streams and had no effect when bubbling in ambient air. Free CA is prohibitively expensive for use in large scale reactors, so methods were developed to retain CA within hydrogels and to chemically couple the enzyme to glass beads. Both retention techniques demonstrated activity when assessed by the MIMS, but hydrogels were mechanically fragile and lost nearly all activity after 2 weeks. CA-beads showed marked improvements in durability and maintained their activity for > 6 months, but the beads showed no catalytic effect when incorporated into packed bed dissolution reactors. These results suggest that the mechanism of CA dissolution catalysis is via direct proton transfer to the mineral surface rather than an increase in the effective concentration of H_2CO_3. These results also match both theoretical predictions made earlier in this thesis, and experimental results in freshwater (Pokrovsky et al., 2005). Enhanced dissolution of carbonate rocks remains a promising avenue to combat climate change, and catalytic materials involving direct proton transfer mechanisms should be considered in the future.

Chapter 5

CONCLUSIONS AND FUTURE WORK

The work set forth in this thesis greatly advances the field of seawater calcite dissolution kinetics. In Chapter 1, we found that the complex relationship between dissolution rate and Ω was due to the activation of different surface processes upon crossing "critical" Ω thresholds. We went on in Chapter 2 to show that these same transitions occurred in the natural environment and, when combined with variations in dissolved organic carbon (DOC) concentrations, explained previously contradictory measurements of *in-situ* dissolution rates. We noted that the energetic parameters in our surface model were likely affected by the chemical speciation of the solution, so in Chapter 3 we proceeded to test this hypothesis. We measured dissolution rates in artificial seawater and found that sulfate enhanced dissolution rates near equilibrium, but inhibited them far from equilibrium. The latest speciation models were then used to fit our rate data with a mechanistic equation of ion attack at the calcite surface. This model successfully explained all of our near equilibrium rate data, regardless of solution. Finally, during the testing of carbon capture reactors, we demonstrated that an enzyme shown to catalyze calcite dissolution rates, carbonic anhydrase, most likely does so via direct proton transfer, rather than increasing the effective concentration of carbonic acid. This result matched predictions from the mechanistic equation in Chapter 3.

The advances discussed above also highlight several remaining questions to be explored in future research. For example, although the rate law in Chapter 2 reconciles disparities amongst previous *in-situ* water-column measurements, a flux analysis reveals that the overall magnitude of inorganic dissolution is insignificant in the North Pacific. One of the goals of CDisK-IV was to quantify the contribution of inorganic dissolution to "Alk*," the amount of alkalinity above and beyond the amount expected from purely transport processes (Feely et al., 2002). In a box model combining an aragonite dissolution rate law with measured *in-situ* particle counts and Ωs, Dong et al. (2019) showed that inorganic aragonite dissolution could only explain ~0.2% of the Alk* signal in the N. Pacific. We reach the same conclusion

when modeling the inorganic dissolution rate for calcite, even when imposing unrealistically low sinking rates to the highest productivity, most undersaturated waters of the cruise (Fig 5.1). Inorganic water-column dissolution can explain ~8% of the Alk* signal at a sinking rate of 1 m day^{-1}, but only ~0.1% at the more commonly cited 100 m day^{-1} (Noji et al., 1997; Timothy et al., 2013). It is clear that more work needs to be done quantifying Alk* signals from respiration driven fluxes (Dong et al., 2019; Jansen et al., 2002) and fluxes out of the sediments (Chen, 2002).

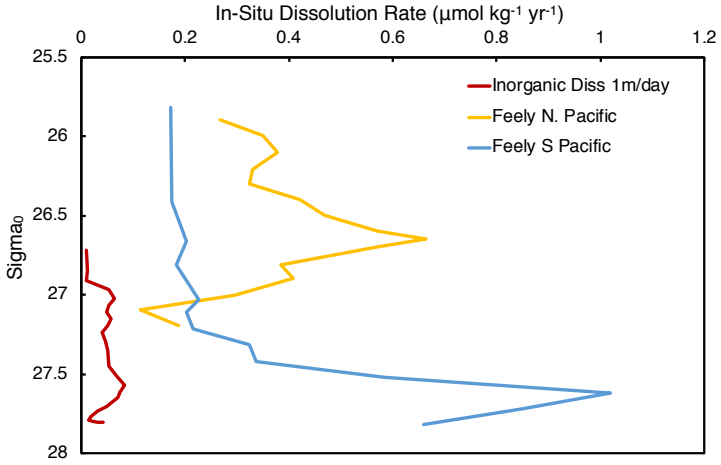

Figure 5.1: Comparison of dissolution rates inferred by Alk* measurements from Feely et al. (2002) with box model results for inorganic calcite dissolution at CDisK-IV Station 5 using the rate law from Chapter 2, a sinking rate of 1 m day^{-1}, and particle flux of 0.69 mmol m^{-2} day^{-1} (upper limit calcite flux from Dong et al. 2019).

On the mechanistic front, more advanced seawater dissolution models will need to be developed and evaluated. The mechanistic model proposed in Chapter 3 is powerful, but can only be applied to a narrow Ω range where dissolution proceeds by defect-assisted etch pit formation. The model cannot account for dissolution rates resulting from homogenous etch pit formation from $0 < \Omega < 0.75$. While it is possible that dissolution kinetics in this regime are driven solely by surface processes (Bibi et al., 2018; Fischer et al., 2014, 2012; Fischer and Lüttge, 2018; Lüttge et al., 2013), there are a variety of alternative models coupling the surface and solution that should be tested. A more rigorous treatment of the calcite crystal

structure (Zhang and Nancollas, 1998, 1990) and/or the electrical double layer (Wolthers et al., 2008) could provide additional explanatory power.

In addition to different surface processes, these new models will need to take into account changes due to solution chemistry. An issue that has been lurking throughout this dissertation is how our results were potentially affected by a change in the sourcing of Dickson seawater. The labeled ^{13}C material used by our group has remained constant for the last 6 years, but the dissolution measurements published by Subhas et al. (2015) and Dong et al. (2018) are an order of magnitude slower than those published by Naviaux et al. (2019). The results are plotted together in Fig. 5.2. Note that the Ωs reported by Subhas et al. (2015) were calculated using a temperature of 25°C, when the actual temperature was closer to 21°C. The temperature has been corrected in Fig. 5.2, such that the data are therefore shifted ~0.04 Ω units farther from equilibrium, increasing the disparity between Subhas et al. (2015), Dong et al. (2018), and Naviaux et al. (2019). All experiments published in Dong et al. and Subhas et al. were conducted in Dickson seawater batches collected prior to July 25, 2014 (B142). According to personal communications with Dr. Dickson, his seawater sourcing transitioned from offshore cruises to seawater pumped up from the Scripps pier over the period of May 2013 to July 2015. Although the change in sourcing does not exactly match the change in rates (Subhas et al. measured slow rates in B135 and B138, both of which were collected from the pier), it is clear from Fig. 5.2 that experiments conducted after the transition was completed yielded faster rates. These fast experiments include an independent test by Dr. Subhas, as well as an inter-comparison test conducted by me, Dr. Subhas, and Dr. Dong where we each used the same seawater and calcite material. The results strongly suggest that a change in the seawater composition was responsible for the increase in rates. We hypothesize that the DOC content could have decreased after the sourcing change, as DOC was shown to slow dissolution rates in Chapter 2. However, DOC was not measured by Dr. Dickson, and there is no seawater remaining from the original offshore cruises that may be retested.

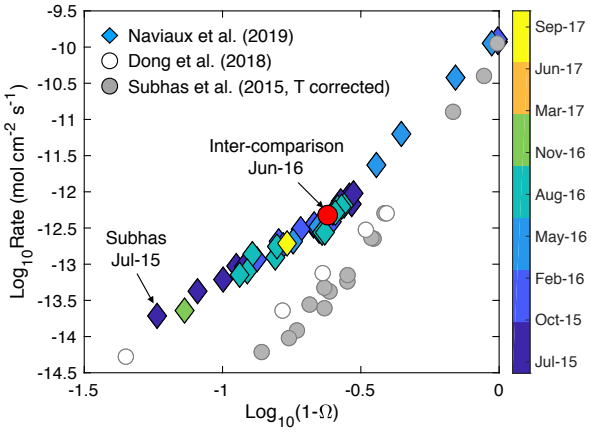

Figure 5.2: Comparison of calcite dissolution rates (mol cm^{-2} s^{-1}) versus $Log_{10}(1-\Omega)$ at 21°C published by our group. The Subhas et al. (2015) Ω values have been corrected from 25 to 21°C. All dissolution rates measured from July 2015-2017 have been faster than those measured prior to July 2015. These fast measurements were replicated independently by Dr. Subhas (July 2015) as well as during an inter-comparison study by each member in our group. They also include multiple different size fractions (20-53 and 70-100 μm) from different powder batches, as well as homegrown calcite (300-500 μm).

There are many other chemical factors known to affect calcite dissolution rates that have yet to be evaluated in seawater. Of particular interest are the impacts of changing the magnesium concentration, as well as the calcium to carbonate ion ratio. These have each been shown profoundly affect calcite growth and dissolution rates in simple solutions (Compton and Brown, 1994; Klasa et al., 2013; Lin and Singer, 2009; Nielsen et al., 2013; Ruiz-Agudo et al., 2010; Sand et al., 2016; Wolthers et al., 2012a). The concentrations of Mg^{2+} and Ca^{2+} have also changed significantly over the last 120 million years (Hain et al., 2015), making it important to incorporate their effects on calcite dissolution rates into our understanding of past climates. Additional experiments in various ionic compositions will also allow for rigorous tests of coupled solution-surface speciation models, especially if combined with atomic force microscopy experiments

The field of calcite dissolution kinetics remains exciting and open to large developments. It has been a pleasure to work on such a complex and interesting problem with such great implications for the global climate system.

BIBLIOGRAPHY

Al Mahrouqi, D., Vinogradov, J., Jackson, M.D., 2017. Zeta potential of artificial and natural calcite in aqueous solution. Adv. Colloid Interface Sci. https://doi.org/10.1016/j.cis.2016.12.006

Alkattan, M., Oelkers, E.H., Dandurand, J.-L., Schott, J., 1998. An experimental study of calcite and limestone dissolution rates as a function of pH from -1 to 3 and temperature from 25 to 80°C. Chem. Geol. 151, 199–214. https://doi.org/10.1016/S0009-2541(98)00080-1

Alkattan, M., Oelkers, E.H., Dandurand, J., Schott, J., 2002. An experimental study of calcite dissolution rates at acidic conditions at 25°C in the presence of $NaPO_3$ and $MgCl_2$. Chem. Geol. 190, 291–302.

Aluwihare, L.I., Repeta, D.J., Chen, R.F., 2002. Chemical composition and cycling of dissolved organic matter in the Mid-Atlantic Bight. Deep. Res. Part II Top. Stud. Oceanogr. 49, 4421–4437. https://doi.org/10.1016/S0967-0645(02)00124-8

Amrhein, C., Jurinak, J.J., Moore, W.M., 1985. Kinetics of Calcite Dissolution as Affected by Carbon Dioxide Partial Pressure. Soil Sci. Soc. Am. J. 49, 1393–1398. https://doi.org/10.2136/sssaj1985.03615995004900060012x

Arakaki, T., Mucci, A., 1995. A continuous and mechanistic representation of calcite reaction-controlled kinetics in dilute solutions at 25°C and 1 atm total pressure. Aquat. Geochemistry 1, 105–130. https://doi.org/10.1007/BF01025233

Archer, D., 1996. A data-driven model of the global calcite lysocline. Global Biogeochem. Cycles 10, 511–526. https://doi.org/10.1029/96GB01521

Archer, D., Eby, M., Brovkin, V., Ridgwell, A., Cao, L., Mikolajewicz, U., Caldeira, K., Matsumoto, K., Munhoven, G., Montenegro, A., Tokos, K., 2009. Atmospheric Lifetime of Fossil Fuel Carbon Dioxide. Annu. Rev. Earth Planet. Sci. 37, 117–134. https://doi.org/10.1146/annurev.earth.031208.100206

Archer, D., Kheshgi, H., Maier-Reimer, E., 1998. Dynamics of fossil fuel CO_2 neutralization by marine $CaCO_3$. Global Biogeochem. Cycles 12, 259–276. https://doi.org/10.1029/98GB00744

Archer, D., Maier-Reimer, E., 1994. Effect of deep-sea sedimentary calcite preservation on atmospheric CO2 concentration. Nature 367, 260–263. https://doi.org/10.1038/367260a0

Archer, D.E., 1991. Equatorial Pacific Calcite Preservation Cycles: Production or Dissolution? Paleoceanography 6, 561–571.

Arvidson, R.S., Collier, M., Davis, K.J., Vinson, M.D., Amonette, J.E., Luttge, A., 2006. Magnesium inhibition of calcite dissolution kinetics. Geochim. Cosmochim. Acta 70, 583–594. https://doi.org/10.1016/j.gca.2005.10.005

Arvidson, R.S., Ertan, I.E., Amonette, J.E., Luttge, A., 2003. Variation in calcite dissolution rates: A fundamental problem? Geochim. Cosmochim. Acta 67, 1623–1634. https://doi.org/10.1016/S0016-7037(02)01177-8

Arvidson, R.S., Luttge, A., 2010. Mineral dissolution kinetics as a function of distance from equilibrium - New experimental results. Chem. Geol. 269, 79–88. https://doi.org/10.1016/j.chemgeo.2009.06.009

Avnir, D., Braun, S., Lev, O., Ottolenghi, M., 1994. Enzymes and Other Proteins Entrapped in Sol-Gel Materials. Chem. Mater. 6, 1605–1614. https://doi.org/10.1021/cm00046a008

Barwise, A.J., Compton, R.G., Unwin, P.R., 1990. The Effect of Carboxylic Acids on the Dissolution of Calcite in Aqueous Solution Part 2. I- and meso-Tartaric Acids. J. Chem. Soc. Faraday Trans. 86, 137–144. https://doi.org/10.1039/ft9908601517

Bender, M.A., Knutson, T.R., Tuleya, R.E., Sirutis, J.J., Vecchi, G.A., Garner, S.T., Held, I.M., 2010. Modeled impact of anthropogenic warming on the frequency of intense Atlantic hurricanes. Science (80-.). 327, 454–458. https://doi.org/10.1126/science.1180568

Benner, R., Pakulski, J.D., McCarthy, M., Hedges, J.I., Hatcher, P.G., 1992. Bulk chemical characteristics of dissolved organic matter in the ocean. Science (80-.). 255, 1561–1564.

Berelson, W.M., Balch, W.M., Najjar, R., Feely, R. a., Sabine, C., Lee, K., 2007. Relating estimates of CaCO3 production, export, and dissolution in the water column to measurements of CaCO3 rain into sediment traps and dissolution on the sea floor:A revised global carbonate budget. Global Biogeochem. Cycles 21, 1–15. https://doi.org/10.1029/2006GB002803

Berelson, W.M., Hammond, D.E., McManus, J., Kilgore, T.E., 1994. Dissolution Kinetics Of Calcium-Carbonate In Equatorial Pacific Sediments. Global Biogeochem. Cycles 8, 219–235. https://doi.org/10.1029/93gb03394

Berger, W.H., 1967. Foraminiferal ooze: Solution at depths. Science (80-.). 156, 383–385. https://doi.org/10.1126/science.156.3773.383

Berner, R.A., Morse, J.W., 1974. Dissolution kinetics of calcium carbonate in sea water IV. Theory of calcite dissolution. Am. J. Sci. 274, 108–134. https://doi.org/10.2475/ajs.274.2.108

Berner, R.A., Westrich, J.T., Graber, R., Smith, J., Martens, C.S., 1978. Inhibition of aragonite precipitation from supersaturated seawater: A laboratory and field study. Am. J. Sci. https://doi.org/10.2475/ajs.278.6.816

Bibi, I., Arvidson, R., Fischer, C., Lüttge, A., 2018. Temporal Evolution of Calcite Surface Dissolution Kinetics. Minerals 8, 256. https://doi.org/10.3390/min8060256

Blanchette, C.D., Knipe, J.M., Stolaroff, J.K., Deotte, J.R., Oakdale, J.S., Maiti, A., Lenhardt, J.M., Sirajuddin, S., Rosenzweig, A.C., Baker, S.E., 2016. Printable enzyme-embedded materials for methane to methanol conversion. Nat. Commun. 7, 1–9. https://doi.org/10.1038/ncomms11900

Boudreau, B.P., 2013. Carbonate dissolution rates at the deep ocean floor. Geophys. Res. Lett. 40, 744–748. https://doi.org/10.1029/2012GL054231

Boudreau, B.P., Middelburg, J.J., Hofmann, A.F., Meysman, F.J.R., 2010. Ongoing transients in carbonate compensation. Global Biogeochem. Cycles 24, 1–13. https://doi.org/10.1029/2009GB003654

Buhmann D., D.W., 1987. Calcite dissolution kinetics in the system H2O-CO2-CaCO3 with participation of foreigns ions. Chem. Geol. 64, p. 89-102 64, 89–102.

Burton, E.A., Walter, L.M., 1990. The role of pH in phosphate inhibition of calcite and aragonite precipitation rates in seawater. Geochim. Cosmochim. Acta 54, 797–808. https://doi.org/10.1016/0016-7037(90)90374-T

Burton, W.K., Cabrera, N., 1949. Crystal growth and surface structure. Part I. Discuss. Faraday Soc. 5, 33. https://doi.org/10.1039/df9490500033

Burton, W.K., Cabrera, N., Frank, F.C., 1951. The Growth of Crystals and the Equilibrium Structure of their Surfaces. Philos. Trans. R. Soc. A Math. Phys. Eng. Sci. 243, 299–358. https://doi.org/10.1098/rsta.1951.0006

Busenberg, E., Plummer, L.N., 1986. A comparative study of the dissolution and crystal growth kinetics of calcite and aragonite. Stud. Diagenesis, U.S. Geol. Surv. Bull. 1578 139–168.

Byrne, R.H., Mecking, S., Feely, R.A., Liu, X., 2010. Direct observations of basin-wide acidification of the North Pacific Ocean. Geophys. Res. Lett. 37, n/a-n/a. https://doi.org/10.1029/2009GL040999

Cabrera, N., Levine, M.M., 1956. XLV. On the dislocation theory of evaporation of crystals. Philos. Mag. 1, 450–458. https://doi.org/10.1080/14786435608238124

Cabrera, N., Levine, M.M., Plaskett, J.S., 1954. Hollow Dislocations and Etch Pits. Phys. Rev. 96, 1153.

Cai, W.-J., Wang, Y., Hodson, R.E., 1998. Acid-base properties of dissolved organic matter in the estuarine waters of Georgia, USA. Geochim. Cosmochim. Acta 62, 473–483.

Caldeira, K., Rau, G.H., 2000. Accelerating carbonate dissolution to sequester carbon dioxide in the ocean: Geochemical implications. Geophys. Res. Lett. 27, 225–228.

Canfield, D.E., Farquhar, J., 2009. Animal evolution, bioturbation, and the sulfate concentraion of the oceans. Proc. Natl. Acad. Sci. 106. https://doi.org/10.1073/pnas.0902037106

Cao, L., Eby, M., Ridgwell, A., Caldeira, K., Archer, D., Ishida, A., Joos, F., Matsumoto, K., Mikolajewicz, U., Mouchet, A., Orr, J.C., Plattner, G.K., Schlitzer, R., Tokos, K., Totterdell, I., Tschumi, T., Yamanaka, Y., Yool, A., 2009. The role of ocean transport in the uptake of anthropogenic CO2. Biogeosciences 6, 375–390. https://doi.org/10.5194/bg-6-375-2009

Carter, B.R., Feely, R.A., Williams, N.L., Dickson, A.G., Fong, M.B., Takeshita, Y., 2018. Updated methods for global locally interpolated estimation of alkalinity, pH, and nitrate. Limnol. Oceanogr. Methods 16, 119–131. https://doi.org/10.1002/lom3.10232

Carter, B.R., Radich, J.A., Doyle, H.L., Dickson, A.G., 2013. An automated system for spectrophotometric seawater pH measurements. Limnol. Oceanogr. Methods 11, 16–27. https://doi.org/10.4319/lom.2013.11.16

Chen, C.T.A., 2002. Shelf-vs. dissolution-generated alkalinity above the chemical lysocline. Deep. Res. Part II Top. Stud. Oceanogr. 49, 5365–5375. https://doi.org/10.1016/S0967-0645(02)00196-0

Chen, J.L., Wilson, C.R., Tapley, B.D., 2006. Satellite gravity measurements confirm accelerated melting of Greenland ice sheet. Science (80-.). 313, 1958–1960.

Chernov, A.A., 1984. Modern Crystallography III: Crystal Growth, Progress in Crystal Growth and Characterization. Springer Science & Business Media. https://doi.org/10.1016/0146-3535(85)90025-5

Chernov, A.A., Rashkovich, L.N., Mkrtchan, A.A., 1986. Solution growth kinetics and mechanism: Prismatic face of ADP. J. Cryst. Growth 74, 101–112. https://doi.org/10.1016/0022-0248(86)90252-6

Chou, L., Garrels, R.M., Wollast, R., 1989. Comparative study of the kinetics and mechanisms of dissolution of carbonate minerals. Chem. Geol. 78, 269–282. https://doi.org/10.1016/0009-2541(89)90063-6

Compton, R.G., Brown, C.A., 1994. The Inhibition of Calcite Dissolution/Precipitation: Mg2+ Cations. J. Colloid Interface Sci. 165, 445–449.

Compton, R.G., Pritchard, K.L., Unwin, P.R., 1989. The effect of Carboxylic Acids on the Dissolution of Calcite in Aqueous Solution Part 1. Maleic and Fumaric Acids. J. Chem. Soc. Faraday Trans. 85. https://doi.org/10.1039/ft9908601517

Compton, R.G., Sanders, G.H.W., 1993. The dissolution of calcite in aqueous acid: The influence of humic species. J. Colloid Interface Sci. https://doi.org/10.1006/jcis.1993.1276

Cruise, G.M., Scharp, D.S., Hubbell, J.A., 1998. Characterization of permeability and network structure of interfacially photopolymerized poly(ethylene glycol) diacrylate hydrogels. Biomaterials 19, 1287–1294. https://doi.org/10.1016/S0142-9612(98)00025-8

Cubillas, P., Köhler, S., Prieto, M., Chaïrat, C., Oelkers, E.H., 2005. Experimental determination of the dissolution rates of calcite, aragonite, and bivalves. Chem. Geol. 216, 59–77. https://doi.org/10.1016/j.chemgeo.2004.11.009

Dale, V.H., Joyce, L.A., McNulty, S., Neilson, R.P., Ayres, M.P., Flannigan, M.D., Hanson, P.J., Irland, L.C., Lugo, A.E., Peterson, C.J., 2001. Climate change and forest disturbances: climate change can affect forests by altering the frequency, intensity, duration, and timing of fire, drought, introduced species, insect and pathogen outbreaks, hurricanes, windstorms, ice storms, or landslides. Bioscience 51, 723–734.

De Giudici, G., 2002. Surface control vs. diffusion control during calcite dissolution: Dependence of step-edge velocity upon solution pH. Am. Mineral. 87, 1279–1285.

De Groot, W.J., Flannigan, M.D., Cantin, A.S., 2013. Climate change impacts on future boreal fire regimes. For. Ecol. Manage. 294, 35–44. https://doi.org/10.1016/j.foreco.2012.09.027

de Kanel, J., Morse, J.W., 1978. The chemistry of orthophosphate uptake from seawater on to calcite and aragonite. Geochim. Cosmochim. Acta 42, 1335–1340. https://doi.org/10.1016/0016-7037(78)90038-8

Dickson, A.G., 2010. Standards for Ocean Measurements. Oceanography 23, 34–47.

Dickson, A.G., 2007. The carbon dioxide system in seawater: equilibrium chemistry and

measurements. Guid. to best Pract. Ocean Acidif. Res. data Report.

Dickson, A.G., 1993. The measurement of sea water pH. Mar. Chem. 44, 131–142. https://doi.org/10.1016/0304-4203(93)90198-W

Dickson, A.G., 1990a. Standard potential of the reaction: AgCl(s) + 1 2H2(g) = Ag(s) + HCl(aq), and and the standard acidity constant of the ion HSO4- in synthetic sea water from 273.15 to 318.15 K. J. Chem. Thermodyn. 22, 113–127. https://doi.org/10.1016/0021-9614(90)90074-Z

Dickson, A.G., 1990b. Thermodynamics of the dissociation of boric acid in synthetic seawater from 273.15 to 318.15 K. Deep Sea Res. Part A, Oceanogr. Res. Pap. 37, 755–766. https://doi.org/10.1016/0198-0149(90)90004-F

Dickson, A.G., Millero, F.J., 1987. A comparison of the equilibrium constants for the dissociation of carbonic acid in seawater media 34, 1733–1743.

Dickson, A.G., Wesolowski, D.J., Palmer, D.A., Mesmer, R.E., 1990. Dissociation constant of bisulfate ion in aqueous sodium chloride solutions to 250°C. J. Phys. Chem. 94, 7978–7985. https://doi.org/10.1021/j100383a042

Ding, H., Rahman, S.R., 2018. Investigation of the Impact of Potential Determining Ions from Surface Complexation Modeling. Energy and Fuels 32, 9314–9321. https://doi.org/10.1021/acs.energyfuels.8b02131

Dobberschütz, S., Nielsen, M.R., Sand, K.K., Civioc, R., Bovet, N., Stipp, S.L.S., Andersson, M.P., 2018. The mechanisms of crystal growth inhibition by organic and inorganic inhibitors. Nat. Commun. 9, 1–6. https://doi.org/10.1038/s41467-018-04022-0

Doney, S.C., Fabry, V.J., Feely, R.A., Kleypas, J.A., 2009. Ocean acidification: the other CO2 problem. Ann. Rev. Mar. Sci. 1, 169–192. https://doi.org/10.1146/annurev.marine.010908.163834

Dong, S., Adkins, J.F., Rollins, N.E., Subhas, A. V., Naviaux, J.D., Celestian, A., Liu, X., Kemnitz, N., Byrne, R.H., Berelson, W.M., 2019. Aragonite Dissolution Kinetics and Calcite/Aragonite Ratios in Sinking and Suspended Particles in the North Pacific. Earth Planet. Sci. Lett. https://doi.org/10.1016/j.epsl.2019.03.016

Dong, S., Subhas, A. V., Rollins, N.E., Naviaux, J.D., Adkins, J.F., Berelson, W.M., 2018. A kinetic pressure effect on calcite dissolution in seawater. Geochim. Cosmochim. Acta 238, 411–423. https://doi.org/10.1016/j.gca.2018.07.015

Dove, P.M., Han, N., Wallace, A.F., De Yoreo, J.J., 2008. Kinetics of amorphous silica dissolution and the paradox of the silica polymorphs. Proc. Natl. Acad. Sci. U. S. A.

105, 9903–9908. https://doi.org/10.1073/pnas.0803798105

Dove, P.M., Han, N., Yoreo, J.J. De, 2005. Mechanisms of classical crystal growth theory explain quartz and silicate dissolution behavior. Proc. Natl. Acad. Sci. 102, 10566.

Dove, P.M., Hochella, M.F., 1993. Calcite precipitation mechanisms and inhibition by orthophosphate: In situ observations by Scanning Force Microscopy. Geochim. Cosmochim. Acta 57, 705–714. https://doi.org/10.1016/0016-7037(93)90381-6

Dreybrodt, W., Lauckner, J., Zaihua, L., Svensson, U., Buhmann, D., 1996. The kinetics of the reaction CO$_2$ + H$_2$O $\rightarrow$ H$^+$+ HCO$^-_3$ as one of the rate limiting steps for the dissolution of calcite in the system H$_2$O-CO$_2$-CaCO$_3$. Geochim. Cosmochim. Acta 60, 3375–3381. https://doi.org/10.1016/0016-7037(96)00181-0

Druffel, E.R.M., Williams, P.M., Bauer, J.E., Ertel, J.R., 1992. Cycling of dissolved and particulate organic matter in the open ocean. J. Geophys. Res. 97, 15639. https://doi.org/10.1029/92JC01511

Dunne, J.P., Hales, B., Toggweiler, J.R., 2012. Global calcite cycling constrained by sediment preservation controls. Global Biogeochem. Cycles 26, 1–14. https://doi.org/10.1029/2010GB003935

Durban, M.M., Lenhardt, J.M., Wu, A.S., Small IV, W., Bryson, T.M., Perez-Perez, L., Nguyen, D.T., Gammon, S., Smay, J.E., Duoss, E.B., Lewicki, J.P., Wilson, T.S., 2018. Custom 3D Printable Silicones with Tunable Stiffness. Macromol. Rapid Commun. 39, 1700563. https://doi.org/10.1002/marc.201700563

Eberlein, K., Leal, M.T., Hammer, K.D., Hickel, W., 1985. Dissolved organic substances during a Phaeocystis pouchetii bloom in the German Bight (North Sea). Mar. Biol. 89, 311–316. https://doi.org/10.1007/BF00393665

Emanuel, K.A., 1987. The dependence of hurricane intensity on climate. Nature 326, 483–485. https://doi.org/10.1038/326483a0

Fakhraee, M., Hancisse, O., Canfield, D.E., Crowe, S.A., Katsev, S., 2019. Proterozoic seawater sulfate scarcity and the evolution of ocean–atmosphere chemistry. Nat. Geosci. 12. https://doi.org/10.1038/s41561-019-0351-5

Feely, R.A., Sabine, C.L., Byrne, R.H., Millero, F.J., Dickson, A.G., Wanninkhof, R., Murata, A., Miller, L.A., Greeley, D., 2012. Decadal changes in the aragonite and calcite saturation state of the Pacific Ocean. Global Biogeochem. Cycles 26, 1–15. https://doi.org/10.1029/2011GB004157

Feely, R.A., Sabine, C.L., Lee, K., Berelson, W., Kleypas, J., Fabry, V.J., Millero, F.J., 2004. Impact of anthropogenic CO2 on the CaCO3 system in the oceans. Science (80-.). 305, 362–366. https://doi.org/10.1126/science.1097329

Feely, R.A., Sabine, C.L., Lee, K., Millero, F.J., Lamb, M.F., Greeley, D., Bullister, J.L., Key, R.M., Peng, T., Kozyr, A., Ono, T., Wong, C.S., 2002. In situ calcium carbonate dissolution in the Pacific Ocean. Global Biogeochem. Cycles 16, 1–12. https://doi.org/10.1029/2002GB001866

Finneran, D.W., Morse, J.W., 2009. Calcite dissolution kinetics in saline waters. Chem. Geol. 268, 137–146. https://doi.org/10.1016/j.chemgeo.2009.08.006

Fischer, C., Arvidson, R.S., Lüttge, A., 2012. How predictable are dissolution rates of crystalline material? Geochim. Cosmochim. Acta 98, 177–185. https://doi.org/10.1016/j.gca.2012.09.011

Fischer, C., Kurganskaya, I., Schäfer, T., Lüttge, A., 2014. Variability of crystal surface reactivity: What do we know? Appl. Geochemistry 43, 132–157. https://doi.org/10.1016/j.apgeochem.2014.02.002

Fischer, C., Lüttge, A., 2018. Pulsating dissolution of crystalline matter. Proc. Natl. Acad. Sci. 115, 201711254. https://doi.org/10.1073/pnas.1711254115

Flannigan, M., Cantin, A.S., De Groot, W.J., Wotton, M., Newbery, A., Gowman, L.M., 2013. Global wildland fire season severity in the 21st century. For. Ecol. Manage. 294, 54–61. https://doi.org/10.1016/j.foreco.2012.10.022

Fong, M.B., Dickson, A.G., 2019. Insights from GO-SHIP hydrography data into the thermodynamic consistency of CO_2 system measurements in seawater. Mar. Chem. 211, 52–63. https://doi.org/10.1016/j.marchem.2019.03.006

Fukuhara, T., Tanaka, Y., Ioka, N., Nishimura, A., 2008. An in situ experiment of calcium carbonate dissolution in the central Pacific Ocean. Int. J. Greenh. Gas Control 2, 78–88. https://doi.org/10.1016/S1750-5836(07)00085-0

Gehlen, M., Bassinot, F.C., Chou, L., McCorkle, D., 2005. Reassessing the dissolution of marine carbonates: II. Reaction kinetics. Deep Sea Res. Part I Oceanogr. Res. Pap. 52, 1461–1476. https://doi.org/10.1016/j.dsr.2005.03.011

Gledhill, D.K., Morse, J.W., 2006. Calcite dissolution kinetics in Na-Ca-Mg-Cl brines. Geochim. Cosmochim. Acta 70, 5802–5813. https://doi.org/10.1016/j.gca.2006.03.024

Gratz, A.J., Hillner, P.E., Hansma, P.K., 1993. Step dynamics and spiral growth on calcite. Geochim. Cosmochim. Acta 57, 491–495. https://doi.org/10.1016/0016-

7037(93)90449-7

Gutjahr, A., Dabringhaus, H., Lacmann, R., 1996. Studies of the growth and dissolution kinetics of the CaCO3 polymorphs calcite and aragonite .1. Growth and dissolution rates in water. J. Cryst. Growth 158, 296–309. https://doi.org/PNR61

Hain, M.P., Sigman, D.M., Higgins, J.A., Haug, G.H., 2016. Response to Comment by Zeebe and Tyrrell on "The Effects of Secular Calcium and Magnesium Concentration Changes on the Thermodynamics of Seawater Acid/Base Chemistry: Implications for the Eocene and Cretaceous Ocean Carbon Chemistry and Buffering." Global Biogeochem. Cycles.

Hain, M.P., Sigman, D.M., Higgins, J.A., Haug, G.H., 2015. The effects of secular calcium and magnesium concentration changes on the thermodynamics of seawater acid/base chemistry: Implications for Eocene and Cretaceous ocean carbon chemistry and buffering. Global Biogeochem. Cycles 29, 517–533. https://doi.org/10.1002/2014GB004986

Hales, B., Emerson, S., 1997. Evidence in support of first-order dissolution kinetics of calcite in seawater. Earth Planet. Sci. Lett. 148, 317–327. https://doi.org/10.1016/S0012-821X(97)00017-4

Hansell, D.A., 2013. Recalcitrant Dissolved Organic Carbon Fractions. Ann. Rev. Mar. Sci. 5, 421–445. https://doi.org/10.1146/annurev-marine-120710-100757

Hansell, D.A., Carlson, C.A., 1998a. Deep-ocean gradients in the concentration of dissolved organic carbon. Nature 395, 263–266. https://doi.org/10.1038/26200

Hansell, D.A., Carlson, C.A., 1998b. Net Communnity Production of Dissolved Organic Carbon. Global Biogeochem. Cycles 12, 443–453.

Harstad, A.O., Stipp, S.L.S., 2007. Calcite dissolution: Effects of trace cations naturally present in Iceland spar calcites. Geochim. Cosmochim. Acta 71, 56–70. https://doi.org/10.1016/j.gca.2006.07.037

Harvie, C.E., Nancy, M., Weare, J.H., 1984. The prediction of mineral solubilities in natural waters: The Na-K-Mg-Ca-H-CI- S04-0H-HC03-C03-COrH20 system to high ionic strengths at 25°C. Geochim. Cosmochim. Acta 48, 723–751.

He, S., Morse, J.W., 1993. The carbonic acid system and calcite solubility in aqueous Na-K-Ca-Mg-Cl-SO4 solutions from 0 to 90°C. Geochim. Cosmochim. Acta 57, 3533–3554. https://doi.org/10.1016/0016-7037(93)90137-L

Heberling, F., Trainor, T.P., Lützenkirchen, J., Eng, P., Denecke, M.A., Bosbach, D., 2011. Structure and reactivity of the calcite-water interface. J. Colloid Interface Sci. 354, 843–

857. https://doi.org/10.1016/j.jcis.2010.10.047

Hoch, A.R., Reddy, M.M., Aiken, G.R., 2000. Calcite crystal growth inhibition by humic substances with emphasis on hydrophobic acids from the Florida Everglades. Geochim. Cosmochim. Acta 64, 61–72. https://doi.org/10.1016/S0016-7037(99)00179-9

Honjo, S., Erez, J., 1978. Dissolution rates of calcium carbonate in the deep ocean: An in situ experiment in the North Atlantic Ocean. Earth Planet. Sci. Lett. 40, 287–300.

Ilyina, T., Zeebe, R.E., 2012. Detection and projection of carbonate dissolution in the water column and deep-sea sediments due to ocean acidification. Geophys. Res. Lett. 39, 1–6. https://doi.org/10.1029/2012GL051272

Inskeep, W.P., Bloom, P.R., 1986. Kinetics of Calcite Precipitation in the Presence of Water-soluble Organic Ligands 1. Soil Sci. Soc. Am. J. 50, 1167–1172.

Ittekkot, V., Brockmann, U., Michaelis, W., Degens, E.T., 1981. Dissolved free and combined carbohydrates during a phytoplankton bloom in the northern North Sea. Mar. Ecol. Prog. Ser. 4, 299–305.

Jahnke, R.A., Craven, D.B., Gaillard, J.-F., 1994. The influence of organic matter diagenesis on CaCO3 dissolution at the deep-sea floor. Geochim. Cosmochim. Acta 58, 2799–2809. https://doi.org/10.1016/0016-7037(94)90115-5

Jansen, H., Zeebe, R.E., Wolf-Gladrow, D.A., 2002. Modeling the dissolution of settling CaCO3 in the ocean. Global Biogeochem. Cycles 16, 11–16. https://doi.org/10.1029/2000GB001279

Jordan, G., Pokrovsky, O.S., Guichet, X., Schmahl, W.W., 2007. Organic and inorganic ligand effects on magnesite dissolution at 100 °C and pH = 5 to 10. Chem. Geol. 242, 484–496. https://doi.org/10.1016/j.chemgeo.2007.05.015

Keir, R.S., 1983. Variation in the carbonate reactivity of deep-sea sediments: determination from flux experiments. Deep Sea Res. Part A. Oceanogr. Res. Pap. 30, 279–296. https://doi.org/10.1016/0198-0149(83)90011-0

Keir, R.S., 1980. The dissolution kinetics of biogenic calcium carbonates in seawater. Geochim. Cosmochim. Acta 44, 241–252. https://doi.org/10.1016/0016-7037(80)90135-0

Kirchman, D.L., Meon, B., Ducklow, H.W., Carlson, C.A., Hansell, D.A., Steward, G.F., 2001. Glucose fluxes and concentrations of dissolved combined neutral sugars (polysaccharides) in the Ross Sea and Polar Front Zone, Antarctica. Deep. Res. Part II Top. Stud. Oceanogr. 48, 4179–4197. https://doi.org/10.1016/S0967-0645(01)00085-6

Kitano, Y., Hood, D.W., 1965. The influence of organic material on the polymorphic crystallization of calcium carbonate. Geochim. Cosmochim. Acta 29, 29–41. https://doi.org/10.1016/0016-7037(65)90075-X

Klasa, J., Ruiz-Agudo, E., Wang, L.J., Putnis, C. V, Valsami-Jones, E., Menneken, M., Putnis, A., 2013. An atomic force microscopy study of the dissolution of calcite in the presence of phosphate ions. Geochim. Cosmochim. Acta 117, 115–128. https://doi.org/10.1016/j.gca.2013.03.025

Knutson, T.R., McBride, J.L., Chan, J., Emanuel, K., Holland, G., Landsea, C., Held, I., Kossin, J.P., Srivastava, A.K., Sugi, M., 2010. Tropical cyclones and climate change. Nat. Geosci. 3, 157.

Koutsoukos, P.G., Kontoyannis, C.G., 1984. Precipitation of Calcium Carbonate in Aqueous Solutions. J. Chem. Soc., Faraday Trans. 1, 1181–1192.

Lasaga, A.C., 1998. Kinetic Theory in the Earth Sciences. Princeton University Press. https://doi.org/10.1515/9781400864874

Lasaga, A.C., Blum, A.E., 1986. Surface chemistry, etch pits and mineral-water reactions. Geochim. Cosmochim. Acta 50, 2363–2379. https://doi.org/10.1016/0016-7037(86)90088-8

Lasaga, A.C., Lüttge, A., 2001. Variation of crystal dissolution rate based on a dissolution stepwave model. Science (80-.). 291, 2400–2404. https://doi.org/10.1126/science.1058173

Lea, A.S., Amonette, J.E., Baer, D.R., Liang, Y., Colton, N.G., 2001. Microscopic effects of carbonate, manganese, and strontium ions on calcite dissolution. Geochim. Cosmochim. Acta 65, 369–379. https://doi.org/10.1016/S0016-7037(00)00531-7

Lee, K., Kim, T.W., Byrne, R.H., Millero, F.J., Feely, R.A., Liu, Y.M., 2010. The universal ratio of boron to chlorinity for the North Pacific and North Atlantic oceans. Geochim. Cosmochim. Acta 74, 1801–1811. https://doi.org/10.1016/j.gca.2009.12.027

Lenton, T.M., Williamson, M.S., Edwards, N.R., Marsh, R., Price, A.R., Ridgwell, A.J., Shepherd, J.G., Cox, S.J., 2006. Millennial timescale carbon cycle and climate change in an efficient Earth system model. Clim. Dyn. 26, 687–711. https://doi.org/10.1007/s00382-006-0109-9

Li, W., Zhou, P.P., Jia, L.P., Yu, L.J., Li, X.L., Zhu, M., 2009. Limestone dissolution induced by fungal mycelia, acidic materials, and carbonic anhydrase from fungi. Mycopathologia 167, 37–46. https://doi.org/10.1007/s11046-008-9143-y

Liang, Y., Baer, D.R., 1997. Anisotropic dissolution at the CaCO3(10$\bar{1}$4)—water interface. Surf. Sci. 373, 275–287. https://doi.org/10.1016/S0039-6028(96)01155-7

Liang, Y., Baer, D.R., McCoy, J.M., Amonette, J.E., LaFemina, J.P., 1996. Dissolution kinetics at the calcite-water interface. Geochim. Cosmochim. Acta 60, 4883–4887. https://doi.org/10.1016/S0016-7037(96)00337-7

Lin, Y.-P., Singer, P.C., Aiken, G.R., 2005. Inhibition of Calcite Precipitation by Natural Organic Material: Kinetics, Mechanism, and Thermodynamics. Environ. Sci. Technol. 39, 1–10. https://doi.org/10.1021/es050470z

Lin, Y.P., Singer, P.C., 2009. Effect of Mg2+ on the kinetics of calcite crystal growth. J. Cryst. Growth 312, 136–140. https://doi.org/10.1016/j.jcrysgro.2009.09.041

Lindskog, S., 1997. Structure and mechanism of Carbonic Anhydrase. Pharmacol. Ther. 74, 1–20. https://doi.org/10.1016/S0163-7258(96)00198-2

Liu, X., Byrne, R.H., Lindemuth, M., Easley, R., Mathis, J.T., 2015. An automated procedure for laboratory and shipboard spectrophotometric measurements of seawater alkalinity: Continuously monitored single-step acid additions. Mar. Chem. 174, 141–146. https://doi.org/10.1016/j.marchem.2015.06.008

Liu, X., Patsavas, M.C., Byrne, R.H., 2011. Purification and characterization of meta-cresol purple for spectrophotometric seawater ph measurements. Environ. Sci. Technol. 45, 4862–4868. https://doi.org/10.1021/es200665d

Lueker, T.J., Dickson, A.G., Keeling, C.D., 2000. Ocean pCO_2 calculated from dissolved inorganic carbon, alkalinity, and equations for K_1 and K_2: Validation based on laboratory measurements of CO_2 in gas and seawater at equilibrium. Mar. Chem. 70, 105–119. https://doi.org/10.1016/S0304-4203(00)00022-0

Luo, G., Kump, L.R., Wang, Y., Tong, J., Arthur, M.A., Yang, H., Huang, J., Yin, H., Xie, S., 2010. Isotopic evidence for an anomalously low oceanic sulfate concentration following end-Permian mass extinction. Earth Planet. Sci. Lett. 300, 101–111. https://doi.org/10.1016/j.epsl.2010.09.041

Lüttge, A., 2006. Crystal dissolution kinetics and Gibbs free energy. J. Electron Spectros. Relat. Phenomena 150, 248–259. https://doi.org/10.1016/j.elspec.2005.06.007

Lüttge, A., Arvidson, R.S., Fischer, C., 2013. A stochastic treatment of crystal dissolution kinetics. Elements 9, 183–188. https://doi.org/10.2113/gselements.9.3.183

MacInnis, I.N., Brantley, S.L., 1992. The role of dislocations and surface morphology in calcite dissolution. Geochim. Cosmochim. Acta 56, 1113–1126.

https://doi.org/10.1016/0016-7037(92)90049-O

Malkin, A.I., Chernov, A.A., Alexeev, I.V., 1989. Growth of Dipyramidal face of dislocation-free ADP crystals; free energy of steps. J. Cryst. Growth 97, 765–769.

McElligott, S., Byrne, R.H., Lee, K., Wanninkhof, R., Millero, F.J., Feely, R.A., 1998. Discrete water column measurements of CO_2 fugacity and pH(T) in seawater: A comparison of direct measurements and thermodynamic calculations. Mar. Chem. 60, 63–73. https://doi.org/10.1016/S0304-4203(97)00080-7

Mehrbach, C., Culberson, C.H., Hawley, J.E., Pytkowicz, R.M., 1973. Measurement of the apparent dissociation constants of carbonic acid in seawater at atmospheric pressure. Limnol. Oceanogr. 18, 897–907. https://doi.org/10.4319/lo.1973.18.6.0897

Millero, F., Huang, F., Zhu, X., Liu, X., Zhang, J., 2001. Adsorption and desorption of phosphate on calcite and aragonite in seawater. Aquat. Geochemistry 7, 33–56.

Millero, F.J., Feistel, R., Wright, D.G., McDougall, T.J., 2008. The composition of Standard Seawater and the definition of the Reference-Composition Salinity Scale. Deep. Res. Part I Oceanogr. Res. Pap. 55, 50–72. https://doi.org/10.1016/j.dsr.2007.10.001

Millero, F.J., Pierrot, D., 1998. A chemical equilibrium model for natural waters. Aquat. Geochemistry 4, 153–199. https://doi.org/10.1023/A:1009656023546

Millero, F.J., Schreiber, D.R., 1982. Use of the ion pairing model to estimate activity coefficients of the ionic components of natural waters. Am. J. Sci. 282, 1508–1540. https://doi.org/10.2475/ajs.282.9.1508

Milliman, J.D., 1975. Dissolution of aragonite, mg-calcite, and calcite in the north atlantic ocean. Geology 3, 461–462. https://doi.org/10.1130/0091-7613(1975)3<461:DOAMAC>2.0.CO;2

Mills, G.A., Urey, H.C., 1940. The Kinetics of Isotopic Exchange between Carbon Dioxide, Bicarbonate Ion, Carbonate Ion and Water. J. Am. Chem. Soc. 62, 1019–1026. https://doi.org/10.1021/ja01862a010

Moran, M.A., Kujawinski, E.B., Stubbins, A., Fatland, R., Aluwihare, L.I., Buchan, A., Crump, B.C., Dorrestein, P.C., Dyhrman, S.T., Hess, N.J., Howe, B., Longnecker, K., Medeiros, P.M., Niggemann, J., Obernosterer, I., Repeta, D.J., Waldbauer, J.R., 2016. Deciphering ocean carbon in a changing world. Proc. Natl. Acad. Sci. 113, 3143–3151. https://doi.org/10.1073/pnas.1514645113

Morel, F.M.M., Rueter, J.G., Anderson, D.M., Guillard, R.R.L., 1979. Aquil - Chemically Defined Phytoplankton Culture-Medium for Trace-Metal Studies. J. Phycol. 15, 135–

141.

Morse, J.W., 1978. Dissolution kinetics of calcium carbonate in sea water; VI, The near-equilibrium dissolution kinetics of calcium carbonate-rich deep sea sediments. Am. J. Sci. https://doi.org/10.2475/ajs.278.3.344

Morse, J.W., 1974. Dissolution kinetics of calcium carbonate in sea water. V. Effects of natural inhibitors and the position of the chemical lysocline. Am. J. Sci. https://doi.org/10.2475/ajs.274.6.638

Morse, J.W., Arvidson, R.S., 2002. The dissolution kinetics of major sedimentary carbonate minerals. Earth-Science Rev. 58, 51–84. https://doi.org/10.1016/S0012-8252(01)00083-6

Morse, J.W., Arvidson, R.S., Lüttge, A., 2007. Calcium Carbonate Formation and Dissolution. Chem. Rev. 107, 342–81. https://doi.org/10.1021/cr050358j

Morse, J.W., Berner, R.A., 1972. Dissolution kinetics of calcium carbonate in seawater: II. A kinetic origin for the lysocline. Am. J. Sci. https://doi.org/10.2475/ajs.272.9.840

Morse, J.W., Wang, Q., Tsio, M.Y., 1997. Influences of temperature and Mg:Ca ratio on CaCO3 precipitates from seawater. Geology 25, 85–87. https://doi.org/10.1130/0091-7613(1997)025<0085

Mucci, A., 1986. Growth kinetics and composition of magnesian calcite overgrowths precipitated from seawater: Quantitative influence of orthophosphate ions. Geochim. Cosmochim. Acta 50, 2255–2265. https://doi.org/10.1016/0016-7037(86)90080-3

Mucci, A., 1983a. The solubility of calcite and aragonite at various salinities, temperatures, and one atmospheric total pressure. Am. J. Sci. 74, 780–799. https://doi.org/10.2475/ajs.283.7.780

Mucci, A., 1983b. The solubility of calcite and aragonite in seawater at various salinities, temperatures, and one atmosphere total pressure. Am. J. Sci. https://doi.org/10.2475/ajs.283.7.780

Mucci, A., Morse, J.W., 1984. The solubility of calcite in seawater of various magnesium concentrations, I=0.697 m at 25°C and one atmosphere total pressure. Geochim. Cosmochim. Acta 48, 815–822.

Mucci, A., Morse, J.W., 1983. The incorporation of Mg^{2+} and Sr^{2+} into calcite overgrowths: influences of growth rate and solution composition. Geochim. Cosmochim. Acta 47, 217–233.

Mullin, J.B., Riley, J.P., 1955. The colorimetric determination of silicate with special reference to sea and natural waters. Anal. Chim. Acta 12, 162–176. https://doi.org/10.1016/S0003-2670(00)87825-3

Naviaux, J.D., Subhas, A. V., Dong, S., Rollins, N.E., Liu, X., Byrne, R.H., Berelson, W.M., Adkins, J.F., 2019a. Calcite dissolution rates in seawater: Lab vs. in-situ measurements and inhibition by organic matter. Mar. Chem. 215, 103684. https://doi.org/10.1016/j.marchem.2019.103684

Naviaux, J.D., Subhas, A. V., Rollins, N.E., Dong, S., Berelson, W.M., Adkins, J.F., 2019b. Temperature Dependence of Calcite Dissolution Kinetics in Seawater. Geochim. Cosmochim. Acta 246, 363–384. https://doi.org/10.1016/J.GCA.2018.11.037

Nielsen, L.C., De Yoreo, J.J., DePaolo, D.J., 2013. General model for calcite growth kinetics in the presence of impurity ions. Geochim. Cosmochim. Acta 115, 100–114. https://doi.org/10.1016/j.gca.2013.04.001

Noji, T.T., Bathmann, U. V., Von Bodungen, B., Voss, M., Antia, A., Krumbholz, M., Klein, B., Peeken, I., Noji, C.I.M., Rey, F., 1997. Clearance of picoplankton-sized particles and formation of rapidly sinking aggregates by the pteropod, Limacina retroversa. J. Plankton Res. 19, 863–875. https://doi.org/10.1093/plankt/19.7.863

Oelkers, E.H., Golubev, S. V., Pokrovsky, O.S., Bénézeth, P., 2011. Do organic ligands affect calcite dissolution rates? Geochim. Cosmochim. Acta 75, 1799–1813. https://doi.org/10.1016/j.gca.2011.01.002

Olsen, A., Key, R.M., Heuven, S. Van, Lauvset, S.K., Velo, A., Lin, X., Schirnick, C., Kozyr, A., Tanhua, T., Hoppema, M., Jutterström, S., Steinfeldt, R., Jeansson, E., Ishii, M., Pérez, F.F., Suzuki, T., 2016. The Global Ocean Data Analysis Project version 2 (GLODAPv2) – an internally consistent data product for the world ocean. Earth Syst. Data Sci. 8, 297–323. https://doi.org/10.5194/essd-8-297-2016

Orr, J.C., Epitalon, J.M., Dickson, A.G., Gattuso, J.P., 2018. Routine uncertainty propagation for the marine carbon dioxide system. Mar. Chem. 207, 84–107. https://doi.org/10.1016/j.marchem.2018.10.006

Parkhurst, D.L., 1995. User's guide to PHREEQC : a computer program for speciation, reaction-path, advective-transport, and inverse geochemical calculations. Lakewood, Colo. : U.S. Dept. of the Interior, U.S. Geological Survey ; Denver, CO : Earth Science Information Center, Open-File Reports Section [distributor], 1995.

Parsons, T.R., 2013. A manual of chemical & biological methods for seawater analysis. Elsevier.

Patsavas, M.C., Byrne, R.H., Wanninkhof, R., Feely, R.A., Cai, W.J., 2015. Internal consistency of marine carbonate system measurements and assessments of aragonite saturation state: Insights from two U.S. coastal cruises. Mar. Chem. 176, 9–20. https://doi.org/10.1016/j.marchem.2015.06.022

Peterson, M.N., 1966. Calcite: Rates of Dissolution in a Vertical Profile in the Central Pacific. Science (80-.). 154, 1542–1544. https://doi.org/10.1126/science.154.3756.1542

Pitzer, K.S., 1973. Thermodynamics of electrolytes. I. Theoretical basis and general equations. J. Phys. Chem. 77, 268–277. https://doi.org/10.1021/j100621a026

Plummer, L.N., Parkhurst, D.L., Wigley, T.M.L., 1979a. Critical Review of the Kinetics of Calcite Dissolution and Precipitation. pp. 537–573. https://doi.org/10.1021/bk-1979-0093.ch025

Plummer, L.N., Parkhurst, D.L., Wigley, T.M.L., 1979b. Critical review of the kinetic of calcite dissolution and precipitation, Chemical Modeling in Aqueous Systems.

Plummer, L.N., Wigley, T.M.L., Parkhurst, D.L., 1978. The kinetics of calcite dissolution in CO2-water systems at 5C to 60C and 0.0 to 1.0 atm CO2. Am. J. Sci. https://doi.org/10.2475/ajs.278.2.179

Pokrovsky, O.S., 1998a. Precipitation of calcium and magnesium carbonates from homogeneous supersaturated solutions. J. Cryst. Growth 186, 233–239. https://doi.org/10.1016/S0022-0248(97)00462-4

Pokrovsky, O.S., 1998b. Surface Speciation of Ca and Mg Carbonate Minerals in Aqueous Solutions: A Combined Potentiometric, Electrokinetic, and DRIFT Surface Spectroscopy Approach. Mineral. Mag. 62A, 1196–1197. https://doi.org/10.1180/minmag.1998.62A.2.291

Pokrovsky, O. S., Golubev, S. V., Jordan, G., 2009. Effect of organic and inorganic ligands on calcite and magnesite dissolution rates at 60 °C and 30 atm pCO2. Chem. Geol. 265, 33–43. https://doi.org/10.1016/j.chemgeo.2008.11.011

Pokrovsky, O.S., Golubev, S. V., Schott, J., 2005. Dissolution kinetics of calcite, dolomite and magnesite at 25°C and 0 to 50 atm pCO_2. Chem. Geol. 217, 239–255. https://doi.org/10.1016/j.chemgeo.2004.12.012

Pokrovsky, Oleg S., Golubev, S. V., Schott, J., Castillo, A., 2009. Calcite, dolomite and magnesite dissolution kinetics in aqueous solutions at acid to circumneutral pH, 25 to 150°C and 1 to 55 atm pCO_2: New constraints on CO_2 sequestration in sedimentary basins. Chem. Geol. 260, 317–329. https://doi.org/10.1016/j.chemgeo.2009.01.013

Pokrovsky, O.S., Schott, J., 2002. Surface Chemistry and Dissolution Kinetics of Divalent Metal Carbonates. Environ. Sci. Technol. 36, 426–432. https://doi.org/10.1021/es010925u

Powell, M.D., Reinhold, T.A., 2007. Tropical Cyclone Destructive Potential by Integrated Kinetic Energy. Bull. Am. Meteorol. Soc. 88, 513–526. https://doi.org/10.1175/BAMS-88-4-513

Raimondi, L., Matthews, J.B.R., Atamanchuk, D., Azetsu-Scott, K., Wallace, D.W.R., 2019. The internal consistency of the marine carbon dioxide system for high latitude shipboard and in situ monitoring. Mar. Chem. 213, 49–70. https://doi.org/10.1016/j.marchem.2019.03.001

Rau, G.H., Caldeira, K., 1999. Enhanced carbonate dissolution: A means of sequestering waste CO2 as ocean bicarbonate. Energy Convers. Manag. 40, 1803–1813. https://doi.org/10.1016/S0196-8904(99)00071-0

Rau, G.H., Caldeira, K., Knauss, K.G., Downs, B., Sarv, H., 2001. Enhanced Carbonate Dissolution as a Means of Capturing and Sequestering Carbon Dioxide. First Natl. Conf. Carbon Sequestration 2, 1–7.

Rau, G.H., Knauss, K.G., Langer, W.H., Caldeira, K., 2007. Reducing energy-related CO2 emissions using accelerated weathering of limestone. Energy 32, 1471–1477. https://doi.org/10.1016/j.energy.2006.10.011

Reddy, M.M., 1977. Crystallization of Calcium Carbonate in the Presence of Trace Concentrations of Phosphorus-Containing Anions. J. Cryst. Growth 41, 287–295. https://doi.org/10.1016/0022-0248(77)90057-4

Repeta, D.J., Quan, T.M., Aluwihare, L.I., Accardi, A., 2002. Chemical characterization of high molecular weight dissolved organic matter in fresh and marine waters. Geochim. Cosmochim. Acta 66, 955–962. https://doi.org/10.1016/S0016-7037(01)00830-4

Reynolds, R.C., 1978. Polyphenol inhibition of calcite precipitation in Lake Powell. Limnol. Oceanogr. 585–597.

Rickard, D.T., Sjöberg, E.L., 1983. Mixed kinetic control of calcite dissolution rates. Am. J. Sci. 283, 815–830. https://doi.org/10.2475/ajs.283.8.815

Ridgwell, A., Zeebe, R.E., 2005. The role of the global carbonate cycle in the regulation and evolution of the Earth system. Earth Planet. Sci. Lett. 234, 299–315. https://doi.org/10.1016/J.EPSL.2005.03.006

Rignot, E., Velicogna, I., Van Den Broeke, M.R., Monaghan, A., Lenaerts, J., 2011.

Acceleration of the contribution of the Greenland and Antarctic ice sheets to sea level rise. Geophys. Res. Lett. 38, 1–5. https://doi.org/10.1029/2011GL046583

Rogelj, J., Den Elzen, M., Höhne, N., Fransen, T., Fekete, H., Winkler, H., Schaeffer, R., Sha, F., Riahi, K., Meinshausen, M., 2016. Paris Agreement climate proposals need a boost to keep warming well below 2 °c. Nature 534, 631–639. https://doi.org/10.1038/nature18307

Ruiz-Agudo, E., Kowacz, M., Putnis, C. V., Putnis, A., 2010. The role of background electrolytes on the kinetics and mechanism of calcite dissolution. Geochim. Cosmochim. Acta 74, 1256–1267. https://doi.org/10.1016/j.gca.2009.11.004

Ruiz-Agudo, E., Putnis, C. V., 2012. Direct observations of mineral fluid reactions using atomic force microscopy: the specific example of calcite. Mineral. Mag. 76, 227–253. https://doi.org/10.1180/minmag.2012.076.1.227

Ruiz-Agudo, E., Putnis, C. V., Jiménez-López, C., Rodriguez-Navarro, C., 2009. An atomic force microscopy study of calcite dissolution in saline solutions: The role of magnesium ions. Geochim. Cosmochim. Acta 73, 3201–3217. https://doi.org/10.1016/j.gca.2009.03.016

Salem, M.R., Mangood, A.H., Hamdona, S.K., 1994. Dissolution of calcite crystals in the presence of some metal ions. J. Mater. Sci. 29, 6463–6467. https://doi.org/10.1007/BF00354005

Sand, K.K., Tobler, D.J., Dobberschütz, S., Larsen, K.K., Makovicky, E., Andersson, M.P., Wolthers, M., Stipp, S.L.S., 2016. Calcite Growth Kinetics: Dependence on Saturation Index, Ca2+:CO32-Activity Ratio, and Surface Atomic Structure. Cryst. Growth Des. 16, 3602–3612. https://doi.org/10.1021/acs.cgd.5b01792

Schott, J., Brantley, S., Crerar, D., Guy, C., Borcsik, M., Willaime, C., 1989. Dissolution kinetics of strained calcite. Geochim. Cosmochim. Acta 53, 373–382. https://doi.org/10.1016/0016-7037(89)90389-X

Schott, J., Pokrovsky, O.S., Oelkers, E.H., 2009. The Link Between Mineral Dissolution/Precipitation Kinetics and Solution Chemistry. Rev. Mineral. Geochemistry 70, 207–258. https://doi.org/10.2138/rmg.2009.70.6

Silverman, D.N., Tu, C.K., 1976. Carbonic Anhydrase Catalyzed Hydration Studied by 13C and 18O Labeling of Carbon Dioxide. J. Am. Chem. Soc. 98, 978–984. https://doi.org/10.1021/ja00420a019

Sjöberg, E.L., 1978. Kinetics and mechanism of calcite dissolution in aqueous solutions at low temperatures, in: Stockholm Contributions in Geology. pp. 1–96.

Sjöberg, E.L., Rickard, D., 1983. The influence of experimental design on the rate of calcite dissolution. Geochim. Cosmochim. Acta 47, 2281–2285. https://doi.org/10.1016/0016-7037(83)90051-0

Sjöberg, E.L., Rickard, D.T., 1985. The effect of added dissolved calcium on calcite dissolution kinetics in aqueous solutions at 25°C. Chem. Geol. 49, 405–413. https://doi.org/10.1016/0009-2541(85)90002-6

Sjöberg, E.L., Rickard, D.T., 1984a. Temperature dependence of calcite dissolution kinetics between 1 and 62°C at pH 2.7 to 8.4 in aqueous solutions. Geochim. Cosmochim. Acta 48, 485–493. https://doi.org/10.1016/0016-7037(84)90276-X

Sjöberg, E.L., Rickard, D.T., 1984b. Calcite dissolution kinetics: Surface speciation and the origin of the variable pH dependence. Chem. Geol. 42, 119–136. https://doi.org/10.1016/0009-2541(84)90009-3

Song, J., Rezaee, S., Zhang, L., Zhang, Z., Puerto, M., Wani, O.B., Vargas, F., Alhassan, S., Biswal, S.L., Hirasaki, G.J., 2019. Characterizing the Influence of Organic Carboxylic Acids and Inorganic Silica Impurities on the Surface Charge of Natural Carbonates Using an Extended Surface Complexation Model. Energy & Fuels acs.energyfuels.8b03896. https://doi.org/10.1021/acs.energyfuels.8b03896

Song, J., Zeng, Y., Wang, L., Duan, X., Puerto, M., Chapman, W.G., Biswal, S.L., Hirasaki, G.J., 2017. Surface complexation modeling of calcite zeta potential measurements in brines with mixed potential determining ions (Ca2+, CO32−, Mg2+, SO42−) for characterizing carbonate wettability. J. Colloid Interface Sci. 506, 169–179. https://doi.org/10.1016/j.jcis.2017.06.096

Stern, N., Stern, N.H., 2007. The economics of climate change: the Stern review. cambridge University press.

Stipp, S.L.S., Hochella, M.F., 1991. Structure and bonding at the calcite surface as observed with X-ray photoelectron spectroscopy (XPS) and (LEED). Geochim. Cosmochim. Acta 55, 1723–1736.

Subhas, A. V., 2017. Chemical Controls on the Dissolution Kinetics of Calcite in Seawater. California Institute of Technology.

Subhas, A. V., Rollins, N.E., Berelson, W.M., Dong, S., Erez, J., Adkins, J.F., 2015. A Novel Determination of Calcite Dissolution Kinetics in Seawater. Geochim. Cosmochim. Acta 170, 51–68. https://doi.org/10.1016/j.gca.2015.08.011

Subhas, A. V., Rollins, N.E., Berelson, W.M., Erez, J., Ziveri, P., Langer, G., Adkins, J.F., 2018. The dissolution behavior of biogenic calcites in seawater and a possible role for

magnesium and organic carbon. Mar. Chem. 205, 100–112. https://doi.org/10.1016/j.marchem.2018.08.001

Subhas, A. V, Adkins, J.F., Rollins, N.E., Naviaux, J., Erez, J., Berelson, W.M., 2017. Catalysis and chemical mechanisms of calcite dissolution in seawater. Proc. Natl. Acad. Sci. 114, 8175–8180. https://doi.org/10.1073/pnas.1703604114

Suess, E., 1973. Interaction of organic compounds with calcium carbonate-II. Organo-carbonate association in Recent sediments. Geochim. Cosmochim. Acta 37, 2435–2447. https://doi.org/10.1016/0016-7037(73)90290-1

Sulpis, O., Lix, C., Mucci, A., Boudreau, B.P., 2017. Calcite dissolution kinetics at the sediment-water interface in natural seawater. Mar. Chem. 195, 70–83. https://doi.org/10.1016/j.marchem.2017.06.005

Sundquist, E.T., 1990. Influence of Deep-Sea Benthic Processes on Atmospheric CO2. Philos. Trans. R. Soc. A Math. Phys. Eng. Sci. 331, 155–165. https://doi.org/10.1098/rsta.1990.0062

Svensson, U., Dreybrodt, W., 1992. Dissolution kinetics of natural calcite minerals in CO2-water systems approaching calcite equilibrium. Chem. Geol. 100, 129–145. https://doi.org/10.1016/0009-2541(92)90106-F

Takahashi, T., 1975. Carbonate chemistry of sea water and the calcite compensation depth in the oceans, in: Sliter, W. V., Bé, A.W.H., Berger, W.H. (Eds.), Dissolution of Deep-Sea Carbonates. Cushman Foundation for Foraminiferal Research, pp. 11–26. https://doi.org/10.1029/2002PA000756.Rickaby

Teng, H.H., 2004. Controls by saturation state on etch pit formation during calcite dissolution. Geochim. Cosmochim. Acta 68, 253–262. https://doi.org/10.1016/S0016-7037(03)00423-X

Thakur, M.S., Vegesna, R.S.B., Karanth, N.G., Kumar, M.A., 2007. Process for preparation of thermostable enzyme.

Thomas, M.M., Clouse, J.A., Longo, J.M., 1993. Adsorption of organic compounds on carbonate minerals 3. Influence on dissolution rates. Chem. Geol. 109, 227–237.

Timothy, D.A., Wong, C.S., Barwell-Clarke, J.E., Page, J.S., White, L.A., Macdonald, R.W., 2013. Climatology of sediment flux and composition in the subarctic northeast pacific ocean with biogeochemical implications. Prog. Oceanogr. 116, 95–129. https://doi.org/10.1016/j.pocean.2013.06.017

Tol, R.S.J., 2002. Estimates of the damage costs of climate change. Part 1: Benchmark

estimates. Environ. Resour. Econ. 21, 47–73.

Troy, P.J., Li, Y., Mackenzie, F.T., 1997. Changes in Surface Morphology of Calcite Exposed to the Oceanic Water Column. Aquat. Geochemistry 2, 1–20.

Uchikawa, J., Zeebe, R.E., 2012. The effect of carbonic anhydrase on the kinetics and equilibrium of the oxygen isotope exchange in the CO 2-H 2O system: Implications for δ 18O vital effects in biogenic carbonates. Geochim. Cosmochim. Acta 95, 15–34. https://doi.org/10.1016/j.gca.2012.07.022

Uppström, L.R., 1974. The boron/chlorinity ratio of deep-sea water from the Pacific Ocean. Deep. Res. Oceanogr. Abstr. 21, 161–162. https://doi.org/10.1016/0011-7471(74)90074-6

Van Cappellen, P., Charlet, L., Stumm, W., Wersin, P., 1993. A surface complexation model of the carbonate mineral-aqueous solution interface. Geochim. Cosmochim. Acta 57, 3505–3518. https://doi.org/10.1016/0016-7037(93)90135-J

van Heuven, S., Pierrot, D., Rae, J.W.B., Lewis, E., Wallace, D.W.R., 2011. CO2SYS v 1.1: MATLAB Program Developed for CO2 System Calculations. ORNL/CDIAC-105b. https://doi.org/10.3334/CDIAC/otg.CO2SYS_MATLAB_v1.1

Velicogna, I., 2009. Increasing rates of ice mass loss from the Greenland and Antarctic ice sheets revealed by GRACE. Geophys. Res. Lett. 36, 2–5. https://doi.org/10.1029/2009GL040222

Vinson, M.D., Luttge, A., 2005. Multiple length-scale kinetics: An integrated study of calcite dissolution rates and strontium inhibition. Am. J. Sci. 305, 119–146. https://doi.org/10.2475/ajs.305.2.119

Walter, L.M., Burton, E.A., 1986. The effect of orthophosphate on carbonate mineral dissolution rates in seawater. Chem. Geol. 56, 313–323. https://doi.org/10.1016/0009-2541(86)90011-2

Walter, L.M., Morse, J.W., 1985. The dissolution kinetics of shallow marine carbonates in seawater: A laboratory study. Geochim. Cosmochim. Acta 49, 1503–1513. https://doi.org/10.1016/0016-7037(85)90255-8

Wang, X., Conway, W., Burns, R., McCann, N., Maeder, M., 2010. Comprehensive study of the hydration and dehydration reactions of carbon dioxide in aqueous solution. J. Phys. Chem. A 114, 1734–1740. https://doi.org/10.1021/jp909019u

Weetall, H.H., 1993. Preparation of immobilized proteins covalently coupled through silane coupling agents to inorganic supports. Appl. Biochem. Biotechnol. 41, 157–188.

https://doi.org/10.1007/BF02916421

Williams, N.L., Juranek, L.W., Feely, R.A., Johnson, K.S., Sarmiento, J.L., Talley, L.D., Dickson, A.G., Gray, A.R., Wanninkhof, R., Russell, J.L., Riser, S.C., Takeshita, Y., 2017. Calculating surface ocean pCO2 from biogeochemical Argo floats equipped with pH: An uncertainty analysis. Global Biogeochem. Cycles 31, 591–604. https://doi.org/10.1002/2016GB005541

Wolthers, M., Charlet, L., Van Cappellen, P., 2008. The surface chemistry of divalent metal carbonate minerals: A critical assessment of surface charge and potential data using the charge distribution multi-site ion complexation model. Am. J. Sci. 308, 905–941. https://doi.org/10.2475/08.2008.02

Wolthers, M., Nehrke, G., Gustafsson, J.P., Van Cappellen, P., 2012a. Calcite growth kinetics: Modeling the effect of solution stoichiometry. Geochim. Cosmochim. Acta 77, 121–134. https://doi.org/10.1016/j.gca.2011.11.003

Wolthers, M., Nehrke, G., Gustafsson, J.P., Van Cappellen, P., 2012b. Calcite growth kinetics: Modeling the effect of solution stoichiometry. Geochim. Cosmochim. Acta 77, 121–134. https://doi.org/10.1016/j.gca.2011.11.003

Wotton, B.M., Flannigan, M.D., 1993. Length of the fire season in a changing climate. For. Chron. 69, 187–192. https://doi.org/10.5558/tfc69187-2

Xie, T., Wu, Y., 2014. The role of microalgae and their carbonic anhydrase on the biological dissolution of limestone. Environ. Earth Sci. 71, 5231–5239. https://doi.org/10.1007/s12665-013-2925-7

Xu, J., Fan, C., Teng, H.H., 2012. Calcite dissolution kinetics in view of Gibbs free energy, dislocation density, and pCO_2. Chem. Geol. 322–323, 11–18. https://doi.org/10.1016/j.chemgeo.2012.04.019

Xu, M., Hu, X., Knauss, K.G., Higgins, S.R., 2010. Dissolution kinetics of calcite at 50–70°C: An atomic force microscopic study under near-equilibrium conditions. Geochim. Cosmochim. Acta 74, 4285–4297. https://doi.org/10.1016/j.gca.2010.04.066

Yang, B., Byrne, R.H., Lindemuth, M., 2015. Contributions of organic alkalinity to total alkalinity in coastal waters: A spectrophotometric approach. Mar. Chem. 176, 199–207. https://doi.org/10.1016/j.marchem.2015.09.008

Yi, H., 1996. Climate change 1995: Economic and social dimensions of climate change: Contribution of Working Group III to the second assessment report of the Intergovernmental Panel on Climate Change. Cambridge University Press.

Yu, J., Elderfield, H., 2007. Benthic foraminiferal B/Ca ratios reflect deep water carbonate saturation state. Earth Planet. Sci. Lett. 258, 73–86. https://doi.org/10.1016/j.epsl.2007.03.025

Zaihua, L., 2010. Role of Carbonic Anhydrase as an Activator in Carbonate Rock Dissolution and Its Implication for Atmospheric CO2 Sink. Acta Geol. Sin. - English Ed. 75, 275–278. https://doi.org/10.1111/j.1755-6724.2001.tb00531.x

Zeebe, R.E., 2012. History of Seawater Carbonate Chemistry, Atmospheric CO2 , and Ocean Acidification. Annu. Rev. Earth Planet. Sci. 40, 141–165. https://doi.org/10.1146/annurev-earth-042711-105521

Zhang, J., Nancollas, G., 1998. Kink Density and Rate of Step Movement during Growth and Dissolution of an AB Crystal in a Nonstoichiometric Solution. J. Colloid Interface Sci. 200, 131–145. https://doi.org/10.1006/jcis.1997.5357

Zhang, J., Nancollas, G.H., 1992. Kinetics and Mechanisms of Octacalcium Phosphate Dissolution at 37C. J. Phys. Chem 96, 5478–5483. https://doi.org/10.1098/rstb.2010.0176

Zhang, J., Nancollas, G.H., 1990. Kink densities along a crystal surface step at low temperatures and under nonequilibrium conditions. J. Cryst. Growth 106, 181–190. https://doi.org/10.1016/0022-0248(90)90062-P

Zhong, S., Mucci, A., 1989. Calcite and aragonite precipitation from seawater solutions of various salinities: Precipitation rates and overgrowth compositions. Chem. Geol. 78, 283–299. https://doi.org/10.1016/0009-2541(89)90064-8

Zuddas, P., Mucci, A., 1998. Kinetics of calcite precipitation from seawater: II. The influence of the ionic strength. Geochim. Cosmochim. Acta 62, 757–766.

Zullig, J.J., Morse, J.W., 1988. Interaction of organic acids with carbonate mineral surfaces in seawater and related solutions: I. Fatty acid adsorption. Geochim. Cosmochim. Acta 52, 1667–1678. https://doi.org/10.1016/0016-7037(88)90235-9

A p p e n d i x A

DERIVATION OF SURFACE MODEL EQUATIONS

Dove et al. (2005) found that the same equations originally developed to describe crystal growth (Burton et al., 1951; Chernov, 1984; Malkin et al., 1989) could also be used to describe dissolution. Although developed for a single component crystal, we step through the model below as it may still provide useful insight into the behavior of $CaCO_3$. According to the surface model, dissolution occurs via the consecutive removal of crystal layers, where each dissolving layer has a defined thickness, h (step height, nm), and retreats along the face of the crystal with a velocity, v (cm/s). There can be several, simultaneous dissolution fronts, and the average spacing between them, λ (nm), influences the overall rate. Closer spacings (smaller λ) allow for more dissolution fronts and a faster rate, whereas farther spacings (larger λ) can only support slower rates. Conceptualized this way, the normalized dissolution rate (length/time) is given by

$$R = \frac{hv}{\lambda} \tag{A.1}$$

The generalized form of Eq. (A.1) holds true for dissolution mechanisms that are not limited by the rate of transport to/from the mineral surface.

The retreat velocity, v, is linearly dependent on the step kinetic coefficient for the solid, the thermodynamic driving force, and the volume element being dissolved. It is classically formulated as (Chernov, 1984; Malkin et al., 1989)

$$v = \omega\beta C_e(1 - \Omega) \tag{A.2}$$

where β is the step kinetic coefficient (cm/s), ω is the molecular volume (cm^3), and C_e is the equilibrium concentration of dissolved species in solution (molecules/cm^3).

The step spacing is the only term in Eq. (A.1) that changes depending on the dissolution mechanism, and it is therefore what sets the functional form of the rate equation. At low driving forces near $\Omega \approx 1$, dissolution occurs primarily via the retreat of pre-existing steps at edges and/or screw dislocations. The step spacing is then derived assuming spiral retreat around a dislocation exceeding a "critical radius," r_c, that is set by the local bonding environment of the crystal and the solution driving force. It is given by (Chernov, 1984; Chernov et al., 1986)

$$\lambda = \frac{8r_c + P}{m} \text{ with } r_c = -\frac{\omega\alpha}{k_b T|\sigma|};\ |\sigma| = \ln(\Omega) \tag{A.3}$$

where m is the number of elementary steps (order 1), P is the perimeter of the core of the dislocation (proportional to $2\pi mh$), k_b is Boltzmann's constant, T is the temperature (Kelvin), $|\sigma|=\ln(\Omega)$ is a measure of the solution driving force, and α is the free energy of step formation per unit step height (mJ/m^2). A larger α implies a slower dissolution rate, as the formation/retreat of a step produces a greater increase in the local surface energy of the crystal. The step edge free energy varies depending upon the local bonding environment of the material, where the bonding environment is affected by solid-solid interactions (whether dissolution is at a kink, step, dislocation, flat surface, etc.) and solid-solution interactions (changes in the chemical speciation of the surface). α is therefore distinct from the average surface energy of a perfect crystal (Burton et al., 1951; Burton and Cabrera, 1949; Cabrera et al., 1954; Cabrera and Levine, 1956; Chernov, 1984).

As the solution undersaturation increases, 2D etch pits begin to form first at crystal defects, and then homogenously across the mineral surface. Although step-retreat continues, it is limited to a single direction (the direction of the step), so its contribution to the overall rate is small once the production and radial spread of etch pits is activated. 2D dissolution therefore changes the dominant shape of the dissolving front from a spiral (Eq. A.3) to a spreading area, and in doing so changes the relevant step spacing to use in Eq. (A.1).

The spacing of etch pits of average area, λ^2, is related to the speed of propagation (v from Eq. A.2) and the steady-state rate of pit opening, J ($cm^{-2}s^{-1}$). The lifetime of a pit is given by (Chernov, 1984).

$$\frac{\lambda}{v} = \frac{1}{J}\frac{1}{\lambda^2} \tag{A.4}$$

Substituting (A.4) into (A.1) gives a new equation that describes the rate of 2D dissolution, either at defects or homogenously across the surface.

$$R_{2D} = h(v^2 J)^{\frac{1}{3}} \tag{A.5}$$

Eq. (A.5) may be further expanded to account for the solution's effect on the steady-state rate of pit opening, J. The rate of pit opening depends on two things: the frequency of new site formation (sites/time) and the probability of surpassing some critical free energy barrier, ΔG_{Crit}^{2D}. The overall energy barrier is, in turn, a function of the *local* step edge free energy α, and the driving force of the solution, σ. It is given by (Malkin et al., 1989)

$$\Delta G_{Crit}^{2D} = -\frac{\pi\alpha^2\omega h}{k_b T|\sigma|} \tag{A.6}$$

We can see from Eq. (A.6) that the required ΔG_{Crit}^{2D} to stabilize and open a pit decreases for constant α as the solution becomes more undersaturated (greater |σ|). The frequency of new site formation is related to the density of active nucleation sites (n_s, sites/cm^2), the lattice spacing (a, nm), and the spreading rate constant for the material (β).

The probability of opening a pit is set by ΔG_{Crit}^{2D} via an Arrhenius-style relation, where the pre-exponential factor contains the steady-state frequency of new site formation, $n_s a\beta$.

$$J = J_0 \exp\left(-\frac{\Delta G_{Crit}^{2D}}{k_b T}\right) \text{ with } J_0 = |\sigma|^{\frac{1}{2}} n_s a h C_e \beta \tag{A.7}$$

The step height, h, and the lattice spacing, a, are physical properties of the mineral that do not change with temperature or solution undersaturation. C_e exhibits a temperature dependence, but this effect is well documented in seawater (Dickson and Millero, 1987; Mehrbach et al., 1973) and simple to account for in the model. Therefore, the crystal parameters in J_0 that set the overall, steady-state nucleation rate are the density of active pit nucleation sites, n_s, and the step kinetic coefficient, β.

β is expected to exhibit temperature dependence according to (Chernov, 1984; Malkin et al., 1989; Xu et al., 2010; Zhang and Nancollas, 1992):

$$\beta = \beta_0 \exp\left(-\frac{\epsilon_{step}}{k_b T}\right) \tag{A.8}$$

Here, the interpretation of ϵ_{step} changes depending upon which of two potential dissolution pathways is occurring. In the first pathway, the dissolving species directly detaches from a kink/step and enters the solution. In the second pathway, the species does not directly detach, but instead diffuses away from a kink/step to become an adatom that can subsequently desorb from the surface. ϵ_{step} in the first case is the energy of direct detachment from a kink/step, and ϵ_{step} in the second case is the energy of surface diffusion. Surface diffusion is hindered on calcite by water (Liang and Baer, 1997) and dipoles on the calcite surface (Gratz et al., 1993), so ϵ_{step} in our system is the energy of direct detachment from kinks/steps.

n_s exhibits a temperature dependence according to (Chernov, 1984; Chernov et al., 1986; Dove et al., 2005):

$$n_s = n_{s0} \exp\left(-\frac{\epsilon_{init}}{k_b T}\right) \tag{A.9}$$

Here, ϵ_{init} is the kinetic energy barrier for removing a species from the surface to initiate a new etch pit. ϵ_{init} is distinct from Eq. (A.6) because, while etch pits can initiate on the surface, they will not be stable and propagate across the mineral face unless ΔG_{Crit}^{2D} has also

been surpassed. The pre-exponential factors in Eq. (A.8) and (A.9) contain entropy terms (Burton et al., 1951).

Substituting Eq. (A.7), (A.6) and (A.2) into (A.5) and rearranging yields an equation describing dissolution by either homogenous or defect-assisted 2D dissolution:

$$\ln\left(\frac{R_{2D}}{(1-\Omega)^{\frac{2}{3}}|\sigma|^{\frac{1}{6}}}\right) = \ln\left(h\beta C_e(\omega^2 h n_s a)^{\frac{1}{3}}\right) - \frac{\pi\alpha^2\omega h}{3(k_b T)^2}\left|\frac{1}{\sigma}\right| \tag{A.10}$$

We arrive at a similar equation for dissolution by step retreat by substituting Eq.'s (A.3) and (A.2) into (A.1) and rearranging:

$$\begin{aligned}\ln\left(\frac{R_{step}}{(1-\Omega)^{\frac{2}{3}}|\sigma|^{\frac{1}{6}}}\right) &= \ln\left(\frac{\omega\beta C_e m h}{P}\right) + \ln\left((1-\Omega)^{\frac{1}{3}}\left|\frac{1}{\sigma}\right|^{\frac{1}{6}}\right) \\ &\quad - \ln\left(1 + 8\left(\frac{\omega\alpha}{P k_b T}\right)\left|\frac{1}{\sigma}\right|\right)\end{aligned} \tag{A.11}$$